Universidade do Minho
Escola de Engenharia

Helena Cristina Lopes Rocha

Graphene Nanoribbons for Multilayer Films
based on Natural Polymers

Helena Cristina Lopes Rocha   Graphene Nanoribbons for Multilayer Films based on Natural Polymers

UMinho | 2014

Novembro de 2014

Universidade do Minho
Escola de Engenharia

Helena Cristina Lopes Rocha

Graphene Nanoribbons for Multilayer Films
based on Natural Polymers

Dissertação de Mestrado
Ciclo de Estudos Integrados Conducentes ao
Grau de Mestre em Engenharia de Materiais

Trabalho efetuado sob a orientação de
Professora Doutora Maria da Conceição de Jesus Rego
Paiva
Professora Doutora Natália Maria Araújo Alves

Novembro de 2014

DECLARAÇÃO

Nome: Helena Cristina Lopes Rocha

Endereço eletrónico: a58700@alunos.uminho.pt   Telefone: 915279021

Número do Bilhete de Identidade: 13913792

Título dissertação: Graphene Nanoribbons for Multilayer Films based on Natural Polymers

Orientadores: Professora Doutora Maria da Conceição de Jesus Rego Paiva

              Professora Doutora Natália Maria Araújo Alves

Ano de conclusão: 2014

Designação do Mestrado: Mestrado Integrado em Engenharia de Materiais

Universidade do Minho, 14/ 11/ 2014

Assinatura:

_____

Helena Cristina Lopes Rocha

Acknowledgments

I would like to express my sincerest appreciation to everyone who supported me and helped me in these years of learning and, in particular, in the conclusion of this dissertation.

I would like to sincerely thank my supervisors, Professor Conceição Paiva and Professor Natália Alves, for their guidance, teaching and support.

I must express my gratitude to my lab partner, Eunice Cunha, for the helpful discussions and friendship.

To everyone and in particular to Rui Costa, Sofia Caridade and Sónia Rego, at 3B's Research Group, I would like to thank for their help and useful advices.

I would like to express my acknowledgment to everyone that somehow contributed to my work and pleasant stay in Denmark. I would like to express my sincere gratitude to Professor Liv Hornekær for accepting me in her group and for all her guidance. To all Surface Dynamics group, I would like to thank their friendship. I would like to specially express my deepest appreciation to Andrew Cassidy for his valuable advices.

To all my friends of the Integrated Master's in Materials Engineering I would like to thank for their friendship and for accompanying me in these five years.

My sincerest gratitude goes to my parents and sister for all support, confidence and unconditional love in all my life.

To Pedro, my true north, I will forever thank and recognize his patience, friendship, support, encouragement and love at all moments.

Graphene Nanoribbons for Multilayer Films based on Natural Polymers

Abstract

Biomedical applications and more precisely, implantable devices or scaffolds for regenerative medicine, typically require the use of biodegradable and/or biocompatible materials with adequate mechanical properties and, depending on the specific application, specific electric properties. In this work, such properties were attempted by combining natural polymers, to provide biodegradability and biocompatibility, and graphene, to provide adequate mechanical and electric properties.

Four different types of graphene were produced through different chemical methods. Both raw multiwall carbon nanotubes (MWNTs) and raw exfoliated graphite (EG) were chemically functionalized by two methods, oxidation using a modified Hummers' method, and functionalization through a 1,3-dipolar cycloaddition reaction. Both functionalization procedures were followed by unzipping/exfoliation in solution, through sonication. The result was functionalized graphene nanoribbons (f-GNRs) and graphene flakes (f-GFs) and oxidized graphene nanoribbons (o-GNRs) and graphene flakes (o-GFs), by subjecting functionalized MWNTs and EG and oxidized MWNTs and EG, respectively, to sonication.

The graphene solutions produced were characterized by Ultraviolet-Visible Spectroscopy, Zeta Potential (ZP), and Scanning Transmission Electron Microscopy (STEM). Graphenes were characterized by Infrared Spectroscopy and Thermogravimetric Analysis (TGA). Additionally, f-GNRs were characterized by Scanning Tunneling Microscopy (STM), and to ease characterization they were previously characterized by Atomic Force Microscopy (AFM) and Optical Microscopy (OM).

Thereafter, multilayer films combining those different types of produced graphene and two biodegradable and biocompatible natural polymers, namely chitosan (CHT) and alginate (ALG), were prepared through the layer-by-layer (LbL) technique, and real time monitored by a quartz crystal microbalance (QCM) for accurate mass sensing. The thickness, viscosity and shear modulus of the produced films were estimated by applying a Voigt based model.

The multilayer films developed in the present work might serve different biomedical applications, such as biosensors, coatings for implants, and electroactive tissues.

Nanofitas de Grafeno para aplicação em Filmes Multicamada baseados em Polímeros Naturais

Resumo

Aplicações biomédicas, mais precisamente, dispositivos implantáveis e *scaffolds* para a medicina regenerativa, tipicamente, exigem materiais biodegradáveis e/ou biocompatíveis, com adequadas propriedades mecânicas e, dependendo da aplicação, propriedades eléctricas. Neste trabalho, polímeros naturais, pela sua biodegradibilidade e biocompatibilidade, foram combinados com grafeno, pelas suas adequadas propriedades mecânicas e elétricas, por forma a responder a tais requisitos.

Quatro tipos de grafeno foram produzidos por diferentes métodos químicos. Nanotubos de paredes múltiplas (MWNTs) e grafite exfoliada (EG) foram funcionalizados quimicamente por dois métodos, oxidação segundo um método de Hummers modificado e funcionalização através da reacção de cicloadição dipolar 1,3. Deste processo resultaram nanofitas de grafeno oxidadas (o-GNRs) e flocos de grafeno oxidados (o-GFs) e, nanofitas de grafeno funcionalizadas (f-GNRs) e flocos de grafeno funcionalizados (f-GFs), pela exposição de MWNTs e EG oxidados e MWNTs e EG funcionalizados, respetivamente, a ultrassons, proporcionando a sua exfoliação.

As soluções de grafeno produzidas foram caraterizadas por espectroscopia ultravioleta-visível, potencial zeta (ZP) e microscópia eletrónica de varredura por transmissão (STEM). Os grafenos foram caraterizados por espectroscopia de infravermelho e análises termogravimétricas (TGA). Adicionalmente, as f-GNRs foram caraterizadas por Microscopia Ótica (OM) e microscopia de força atómica (AFM) por forma a facilitar a observação das f-GNRs por microscopia de efeito de túnel (STM).

Posteriormente, filmes multicamada combinando os diferentes tipos de grafeno produzidos com dois polímeros naturais biodegradáveis e biocompatíveis, nomeadamente quitosano (CHT) e alginato (ALG), foram produzidos através da técnica de deposição camada a camada (LbL), e monitorizados em tempo real através de uma microbalança de cristal de quartzo (QCM). A espessura, viscosidade e módulo de cisalhamento dos filmes multicamada produzidos foram estimados pela aplicação de um modelo de Voigt.

Os filmes multicamada desenvolvidos no presente trabalho podem ser aplicados em diversas aplicações biomédicas, como biosensores, revestimentos de implantes e tecidos electroativos.

Contents

List of Figures

List of Tables

Chapter 1

Introduction

This chapter is an introduction to this dissertation, including the motivation for this work, describing the importance of the materials used, graphene and natural polymers, for biomedical industry. Finally, the objectives envisaged are highlighted.

1.1. Motivation

Implants and biodevices such as biosensors, bone fixation devices or scaffolds for regenerating cardiac tissue, may cause severe immunological reactions in the host body, and consequently reduce the performance of the implant/device. Natural polymers are promising materials to overcome such issues, due to their inherent biodegradability and biocompatibility, however they lack mechanical and electrical properties [1]. A composite material may overcome these issues, by combining synergies of natural polymers with a reinforcement material like graphene, with overwhelming mechanical, electrical and thermal properties, as well as presumable non-toxic behavior [2], [3].

In 2004, Geim and Novoselov accomplished to isolate graphene, a single layer of graphite, through mechanical exfoliation of graphite, using scotch-tape. This experiment proving the stability of graphene, and the properties that were experimentally derived from it, awarded them the Nobel Prize in Physics, in 2010. Graphene was well known, from the theoretical point of view, among the scientists for several years. However, the research of this incredible material was exploited when it was possible for the first time to isolate it, which was thought to be thermodynamically unstable [4]. The increase on the number of documents published on this topic is evident in figure 1 and this increase is noteworthy since 2010.
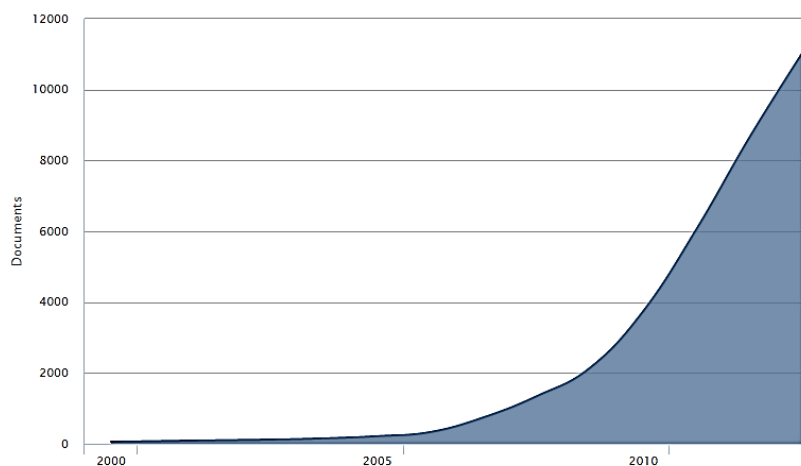
Figure 1: Published documents about graphene since 2000 until the end of 2013. Analysis obtained through Scopus™ of Elsevier

Graphene owes this intense research to its incredible properties: great tensile strength and elastic modulus, ballistic electric conductivity, high thermal conductivity, flexibility and transparency. [4]–[7]

Graphene may serve numerous applications, which are dependent on the graphene production technique, since different graphene properties may be obtained. [6]

1.2. Objectives

The main goal of this work is to produce multilayer films by assembling alternate layers of graphene and natural polymers, through the layer-by-layer (LbL) technique, to take advantage of the interesting graphene properties simultaneously with the biodegradability and biocompatibility of natural polymers, useful for biomedical applications. The necessary conditions to produce the multilayer films, such as solution concentration or pH must be investigated. It is also intended to estimate several properties of the produced multilayer films, such as thickness, viscosity and shear modulus, by applying a Voigt based model.

To accomplish the main objective of this work, different types of graphene, in both forms of graphene nanoribbons (GNRs) and graphene flakes (GFs), were produced by chemical methods and further ultrasounds application. This dissertation aims to characterize the graphene produced using different techniques, namely Ultraviolet-Visible Spectroscopy, Infrared Spectroscopy, TGA, ZP and STEM, in order to compare the methods used for graphene production and inherent graphene properties. f-GNRs are further characterized by STM, where the best deposition technique and parameters for this purpose are analyzed by AFM and OM.

Chapter 2

State of the Art

Chapter 2 presents the state of the art of the materials involved in this work. Graphene structure, properties, applications, STM studies, production techniques and its application in multilayer films, produced by the layer-by-layer technique are further discussed. The state of the art regarding to the potential biomedical application of the multilayer films produced in this work is also described.

2.1. Carbon nanotubes

Carbon nanotubes (CNTs) are one-dimensional structures and may be divided into two types: single-walled carbon nanotubes (SWNTs), a rolled-up graphene sheet, and multiwall carbon nanotubes (MWNTs), multiple concentric rolled-up graphene sheets [8]. A representative schematic structure of these carbon allotropes is presented in figure 2.

SWNT   **MWNT**
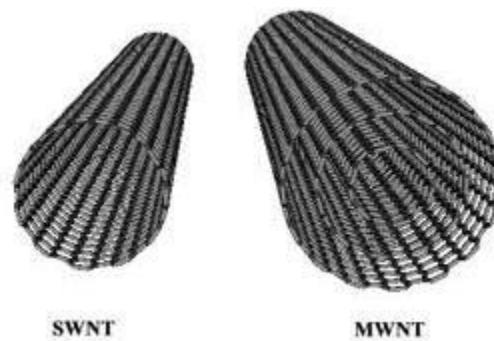
Figure 2: SWNT and MWNT structure [9]

CNTs are expected to be excellent reinforcing materials owing to their mechanical and electrical properties, density and aspect ratio, even at low percolation threshold [8], [10]. A value of 22 GPa tensile strength for a SWNT, values between 11 and 63 GPa tensile strength for MWNT and 1TPa Young's modulus were measured [8], [10]. The density of SWNTs is in the range of 1.33 to 1.40 g/cm³ [10] and approximately 1.74 g/cm³ for MWNTs [11]. A diameter of 1 to 2 nm for SWNTs, and typically 5 - 50 nm for MWNTs (can be smaller or larger, depending on the number of concentric tubes) and the large lengths of the CNTs – in the micrometer or, sometimes, millimeter range – confer them a huge aspect ratio. [10]

A SWNT may behave like a metal or semiconductor, while a MWNT behave like a metal [10], leading to ballistic electronic transport [8]. Theoretically, the thermal conductivity of CNTs is 6000 W/(m.K), however, it was measured to be as high as 3000 W/(m.K). [8]

CNTs potential applications concern reinforcements, for example, in high performance power transmission cables/wires (as CNTs may overcome power loss in energy transmission due to their high electrical conductivity), in lubricants as a lubricant additive to improve tribology properties, and in marine current turbines to improve both mechanical properties and energy transmission efficiency. [10]

However, the production of CNTs reinforced composites faces yet some difficulties [8],[10]. The most used technique to produce CNTs, chemical vapor deposition (CVD), so far is not able to

produce defect-free CNTs and it uses catalysts which remain in the CNTs afterwards, leading to variable CNTs properties [10]. The CNTs are produced in bundle form, being a problem to disperse it in the composite matrix, resulting in high cost production [10]. This problem has been studied by application of ultrasounds and functionalization of the CNTs to improve polymer matrix/CNTs interfaces [8],[10]. A consensus regarding CNTs toxicity has also not been achieved [10].

2.2. Graphite

Graphite may be found in two crystal phases, hexagonal and rhombohedral, being the hexagonal (figure 3) the most common in nature [12]. Stacked graphene sheets stabilized by van der Waals forces with an interlayer spacing of 3.35 Å, form graphite, forming a three-dimensional material [13], [14].
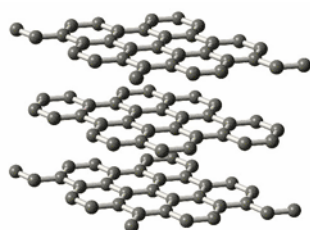
Figure 3: Graphite structure [15]

Being an abundant material on earth, graphite is quite cheap [16]. Graphite has good in-plane thermal conductivity, 522 W/(m.K) [17], good electrical conductivity, with a semi-metal behavior [13], [16], high melting point (3800 K) [12], fairly low surface area (10 m^2/g, depending on its physical form, exfoliation extent, etc.) [18], chemical inertness, oxidation stability [19], low coefficient of friction and is inflammable and non-toxic [12]. The van der Waals forces between graphene layers result in reduced mechanical properties [17].

Graphite is commonly used in electric arc furnaces, nuclear reactors, fire retardant additives, lithium batteries [20], crucibles for molten metals and lubricants [12].

This work used exfoliated graphite (EG), a treated graphite product, synthetized by intercalation compounds, possible to prepare due to the weak van der Waals forces [21] between graphene planes, followed by exfoliation, or thermal expansion, generally done by fast thermal heating up to 900 °C [22].

EG can resist to high-temperature and corrosive environments, has low coefficient of thermal expansion [23], low density and high porosity [22].

2.3. Graphene

2.3.1. Structure

Graphene is a two-dimensional material consisting on a sheet of sp2 hybridized carbon atoms bonded in a hexagonal lattice [5], as schematically presented in figure 4.
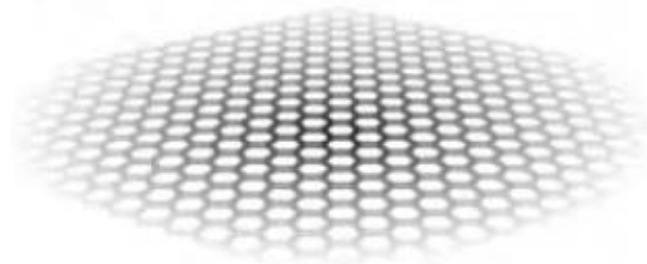
Figure 4: Scheme of graphene hexagonal structure. Adapted from [5]

The sp2 hybridization results from the combination of one s (2s) orbital and two p (2p$_x$ and 2p$_y$) orbitals, resulting in a trigonal planar structure, where each carbon is covalently bonded, in the plan, through σ-bonds to three different carbon atoms and overlapped π-orbitals, forming the delocalized π band, with the occupied valence band, and the delocalized π* band, the unoccupied conduction band [24]–[26]. The C-C bond distance under this bonding condition is 1.42 Å [25].

In the graphene band structure, the valence band meets the conduction band at the Fermi Energy (E_f), which can be described by two non-equivalent Dirac cones. These cones are located at the charge neutrality points, represented by K and K' [24]. The other Dirac points are obtained by the translation of a reciprocal lattice vector.

The band structure of single layer graphene is presented in figure 5.
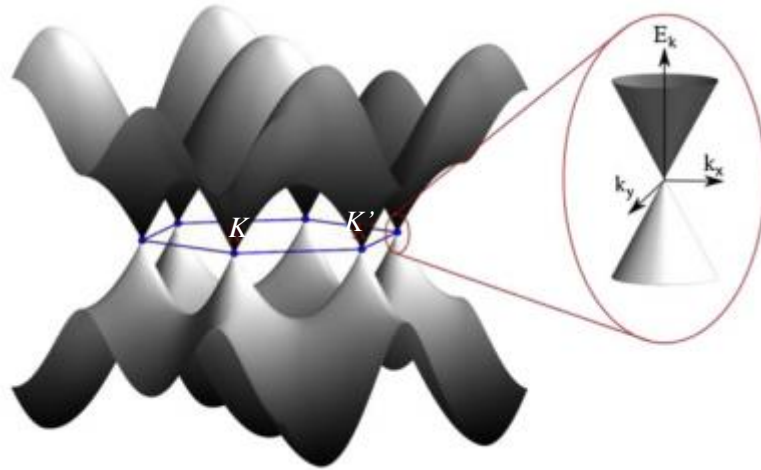
Figure 5: Graphene band structure with the valence band (lower band) meeting the conduction band (upper band) at the Fermi energy with a conical shape [24]

As the conduction and valence bands of graphene meet at the Dirac point, where de density of states (DOS) is zero, graphene is a zero-gap semiconductor with no band-gap between the valence and conduction bands, with vanishing DOS at the Dirac point. [24]

The ideal V-shape of graphene at the Dirac point might be shifted from the E_F due to disorders such as strain, ripples or local doping. [24]

The trigonal covalently bonded structure of graphene is responsible for the flexibility and mechanical properties of graphene, while the delocalized π-orbitals are responsible for the electronic properties of graphene. [25], [26]

2.3.2. STM studies

Scanning Tunneling Microscopy (STM) is an unique tool for surface characterization at atomic scale, as well as, for electrical characterization [27]. STM can image defects at the graphene surface, and using Scanning Tunneling Spectroscopy (STS) the electronic properties of graphene may be measured, by probing the local density of states (DOS) [28], [29]. Additionally, these atomically resolved images of defects and functional groups are also helpful for understanding and explaining the mechanical properties of graphene [30].

Since this work is concerned about GFs and GNRs, this section includes a simple literature survey on STM/STS studies of GNRs and GFs, with focus on substrates and deposition techniques reported, for a more efficient sample preparation to study the graphene produced in this work through STM.

Highly Oriented Pyrolitic Graphite (HOPG) and silicon dioxide (SiO₂) coated Si wafer are the most used substrates on graphene research. SiO₂ lacks electrical conductivity, therefore it is not an appropriate substrate for STM studies. HOPG, on the other hand, is electrically conductive and its atomic structure matches with graphene, making it a non-invasive substrate [31], being possible to measure graphene properties in a more accurate way and closer to the properties expected for free standing graphene. [27]

Some other substrates, such as Au(111) [32], [33] or mica [34] have been also reported as graphene substrates for STM studies.

Regarding graphene solutions, deposition techniques like solvent-casting [30] or spin-coating [33] have been reported, but the most commonly used is droplet deposition [29], [35].

Reported studies on GNRs using STM/STS evidence the importance of these techniques for the electrical and atomic characterization of these carbon allotrope materials. [33], [36]

GNRs were produced through unzipping of MWNTs, by oxidation at defect sites and edges, followed by their dispersion in an organic solvent and sonication, as reported by L. Jiao et al. [37]. Those GNRs were deposited onto Au(111) substrate by spin-coating and revealed to have curved edges, which the authors claimed to be folded graphene edges. At the same time, the authors were able to observe that those GNRs presented random chirality and that MWNTs tend to unzip following their axial direction. STS measurements revealed a 130 meV energy band-gap for a 19.5 ± 0.4 nm wide GNR. [33]

GNRs and graphene quantum dots (GQDs) were produced by mechanical exfoliation of HOPG and deposited on Si substrate, as reported by K. A. Ritter and J. W. Lyding [36]. Atomically resolved STM images revealed the edge atomic structure of these GNRs, which combined with STS measurements allowed the authors to conclude that higher fraction of armchair-edge leads to greater energy band-gap than for GNRs with similar width with zigzag edges. For the same width, 2-3 nm wide, a zigzag terminated edge GNR presented a band-gap of 140 meV while an armchair terminated edge presented a band-gap of 380 meV [36].

2.3.3. Properties and Applications

For years, diamond was believed to be the material with highest thermal conductivity, but in 2008, an experimental work reported that graphene, produced through mechanical exfoliation of graphite,

showed values of thermal conductivity ranging from 4840 ± 440 to 5300 ± 480 W/(mK). Another work reported in 2010, revealed a thermal conductivity of 2500 W/(mK) for a graphene sheet produced by Chemical Vapor Deposition (CVD). [5]

The tensile strength of graphene is approximately 130 GPa, about 200 times the value of steel, and the Young's modulus is about 1TPa. However, these values depend on the type and number of defects, decreasing considerably with the increase in defects [5], [6].

A graphene surface is chemically inert, but is prone to physical adsorption by π- π interactions. Also, chemical groups such as carboxyl (COOH), phenol (COH), hydrogenated (CH) and amine (NH$_2$), for example, may be chemically anchored at the graphene edge, decreasing its chemical inertness. [5]

The high carrier's mobility make graphene an interesting substitute material for silicon (Si) in the transistor Si-based technology, which is close to find its fundamental limits [6], [38]. However, one of the major complications of this application is the absence of a band-gap in graphene, which has found some solutions yet limited, such as the use of GNRs and chemically modified graphene [6]. Some electronic mobility values of graphene have been reported: 15 000 cm^2/(V.s) [39], 200 000 cm^2/(V.s) [7], 250 000 cm^2/(V.s) [6], which may mean a ballistic transport [7], [39]. Graphene is a semimetal with zero band-gap, while GNRs may be semiconductors with a band-gap energy that decreases with the increase of the GNRs width, making possible their use in transistor applications [5], [40].

A graphene monolayer presents approximately 97.3% of optical transparency, and combined with its flexibility and electric conductivity [7], [41], graphene may find applications such as flexible touch screens [41], transparent solar cells and photovoltaic applications in general [7], [42].

Due to the large specific area, 2630 m^2/g, high thermal conductivity, excellent mechanical strength, and changes in conductance when certain molecules are adsorbed at the graphene surface, they may be detected by charge transfer between graphene and these molecules. This behavior of graphene makes it valuable to be used as a sensor [3], [7].

The graphene properties are adequate for the improvement of the efficiency of electric batteries [38], and conductive polymers composites [6], [38]. Other applications are hydrogen storage [38], conductive ink, and supercapacitors [6].

Overall two major drawbacks of graphene should be referred. The first one is that the single sheets of graphene may re-stack owing to the re-forming of π - π interactions [43] and the second one is the poor dispersion of graphene in aqueous media. Only GO is soluble in water due to its oxidation level, however its electronic properties are not interesting [44]–[47].

2.3.4. Production Techniques

So far, several methods to produce graphene were reported such as CVD, thermal decomposition on silicon carbide (SiC) substrate, micromechanical exfoliation and chemical exfoliation of graphite [7], [48]. CNTs have also been used to produce GNRs, through intercalation followed by exfoliation and chemical, physico-chemical, catalytic and electrical methods [5]. The formation of GNRs under a Scanning Tunneling Microscope (STM) was also reported [49].

These are different routes to produce graphene but they might be classified into two groups: bottom-up and top-down routes. The first describes the production of graphene using carbon atoms, resorting to chemical routes, while the last one is based on the use of bulk graphite or even CNTs to obtain graphene. [50]

CVD-grown graphene is suitable for applications such as transparent conductive layers and electronics [6] and is the most used large-scale technique to produce graphene for those applications [48]. Graphene produced by this technique is too expensive for bulk applications. Some drawbacks of this technique are related to the difficulty to produce perfect single-layer graphene [48] and the graphene domains (grains) have small dimensions and defective grain boundaries [51]. Summarily, this process involves the decomposition of a carbon source into carbon atoms, by a catalyst [48] and further deposition of a single or multilayer graphene over Ni or Cu substrates [51], which are then etched away from graphene for it to be transferred onto a suitable substrate for a given application [6], [51].

Intensified research on graphene production started when Geim and Novoselov et al., in 2004, reported the production of single-layer graphene by micromechanical exfoliation of graphite using scotch-tape [5]. The yield process of this technique is very low [48], thus it is used only for research purpose, but the obtained graphene may present large dimensions and good charge carrier mobility at room temperature [6].

Mostly, the chemical exfoliation of graphite to produce GO, is carried out using the Hummers' method [52], based on $KMnO_4$ and H_2SO_4 oxidation of graphite [7], followed by exfoliation by sonication [7], [51]. The decrease of electrical conductivity is inherent to the oxidation of graphene, due to the covalent bonding of oxygen to the carbon atoms in the graphene lattice, and formation of oxygen-functional groups, e.g. epoxide, carbonyl or carboxylic groups [52]. However, these polar oxygen-functional groups confer hydrophilicity to GO, enabling it to be dispersed in several solvents and especially in water [7]. GO is suitable for applications such as biosensors and optical materials [52]. This procedure was reported for CNTs, as well [2], [32].

MWNTs can be opened by intercalation of lithium and ammonia, and exfoliated once intercalation increases the interlayer spacing inducing stresses, which will help to break the CNT wall. The exfoliation occurs due to a thermal and acid treatment with hydrochloric acid (HCl). [5], [55]

The catalytic cutting method has a very low yield but is a simple method. Cobalt or Nickel catalytic metal nanoparticles may cut graphene sheets from CNTs along armchair or zigzag lines. After nanoparticles deposition, the resulted coated CNTs are placed onto Si wafers at 1123 K with H_2-Ar flow. The carbon bonds of CNTs are dissociated by the metal particles and hydrogen from the flow reacts with carbon to produce methane. [5]

An electric current of a microscope may open CNTs but with a low yield of unzipping. [5]

In a physico-chemical method, MWNTs are placed onto a Si substrate and coated with a Poly(methyl methacrylate) (PMMA) film. Subsequently, the film containing PMMA and MWNTs is removed from the Si substrate, rolled over to be subject to Ar plasma and finally the PMMA film is detached from the produced GNRs. This process has a relatively low yield, but the produced GNRs present quite uniform shape and narrow width distribution between 10 and 20 nm. [5], [54]

In 2010, the unzipping of functionalized MWNTs, f-MWNTs, induced by STM was reported (figure 6). It was observed that the functionalization, together with the STM conditions, accomplished the unzipping of the CNT and enabled obtaining clean and non-oxidized GNRs. [49]

14
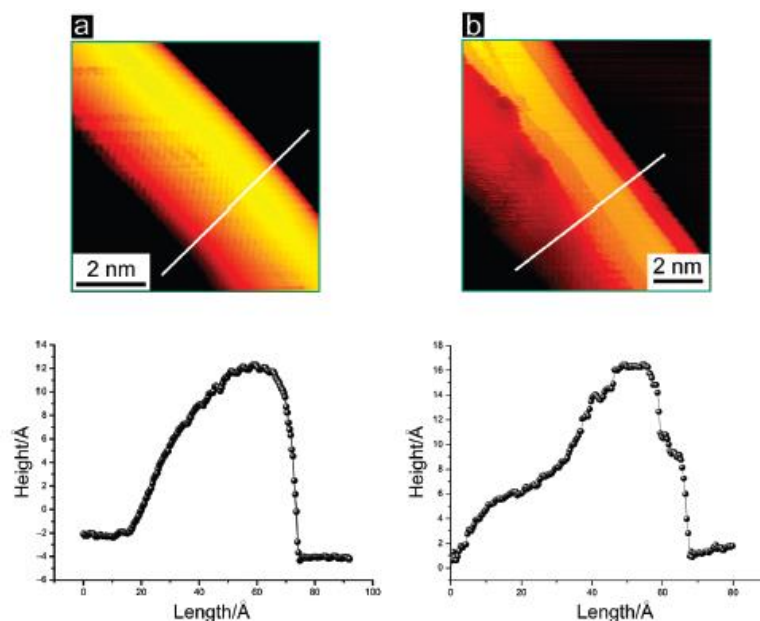
Figure 6: STM image and profile along the white line of a **(a)** non-functionalized region of a CNT, and **(b)** functionalized region of a CNT; (scanning conditions: (a) It = -2.2 nA, Vt = -7 mV; (b) It = -2.2 nA, Vt = -29 mV) [49]

The covalent bond between the functionalization group and the carbon atom from the outer layer of the functionalized CNT causes the increase of the bond length and, consequently, the decrease of the bond strength and, somehow when the STM tip interacts with the two tetrahedral sp3-hybridized carbon atoms obtained by the cycloaddition reaction, the unzipping is observed. The exact mechanism that leads to this is not yet completely understood. [49]

The functionalization of the CNT consisted in a 1,3-dipolar cycloaddition reaction, achieved by mixing α-amino acid, paraformaldehyde and CNTs, under solvent-free conditions, at 483 K for seven hours, resulting in two different functional groups bonded onto the CNT surface, protected amine and pyrrolidine, group 1 and 2 in figure 7, respectively. Pyrrolidine is formed above 453 - 473 K by thermal cleavage of the protecting group of the protected amine. [49]
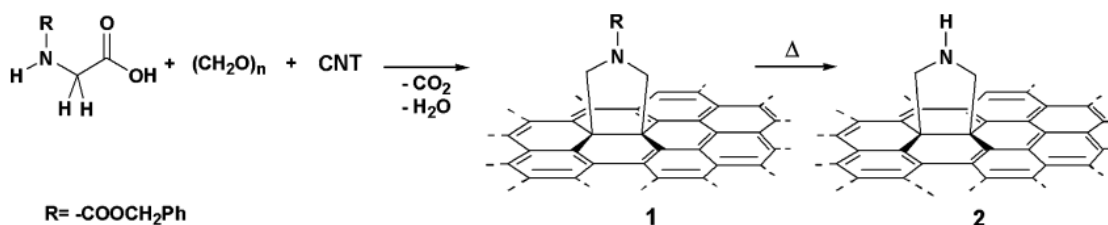
Figure 7: Schematic representation of the 1,3-dipolar cycloaddition functionalization. Functional group 1 is the protected amine and functional group 2 is pyrrolidine [49]

A similar effect as described above may be observed in a solution of functionalized CNTs by means of a high energy ultrasonic bath. In this dissertation, a similar functionalization was applied to MWNTs and EG to produce GNRs and GFs, respectively.

In the present work, the synthesis of GFs and GNRs through chemical exfoliation, either through EG and MWNTs, will be the main focus. More precisely, the chemical approaches used for the formation of GFs and GNRs from EG and MWNTs will be through covalent functionalization by the 1,3-dipolar cycloaddition reaction and through the chemical oxidation by potassium permanganate ($KMnO_4$) and sulfuric acid (H_2SO_4), following a modified Hummers' method [52] for EG and a method proposed by Kosynkin and coworkers [53] for MWNTs. The method proposed by Kosynkin and coworkers uses the same reagents as the modified Hummers' method ($KMnO_4$ and H_2SO_4), but in different amounts, thus Kosynkin's method is often regarded as a modified Hummers' method. The chemical methods will be used as a comparison, being the modified Hummers' method the most used technique to produce graphene oxide from graphite or CNTs.

2.4.   Natural Polymers

In general, polymeric biomaterials may be divided into two classes, natural and synthetic polymers. Natural polymers are naturally made polymers found in the environment, such as chitosan, hyaluronic acid, cellulose, alginate or silk [1]. Usually, natural polymers are biocompatible and biodegradable but they may present immunogenicity, purity variability, poor mechanical properties and difficult degradability tailoring, while synthetic polymers present workable chemical, structural, and mechanical properties, negligible among batches, yet they may lack biocompatibility and might be toxic and cause inflammatory biological reactions. [1]

Biocompatibility may be seen as the toleration of a biological ex vivo or in vivo environment face to a foreign material, or in other words, it can be stated as the change in the biological environment caused by the foreign material. Toxicity, bioprocessibility and functionality may suggest the extent of biocompatibility [1].

Biodegradability regards to the biomaterial capability of being degraded in the biological system by means of bio-based reactions, such as enzymes. Biodegradation may include two distinct but complementary processes, degradation and erosion. For instance, biodegradable properties are desirable for controlled drug delivery systems, and scaffolds for regenerating distinct human tissues. [1]

Chitosan (CHT), a natural polymer, is produced through de-acetylation of chitin, by converting the acetyl groups of chitin into free amine groups, by hydrolysis, obtaining different degrees of de-acetylation (DA) [56]. This biopolymer is an abundant, low cost linear polysaccharide, with amine and hydroxyl functional groups [56]. Its structure is presented in figure 8.
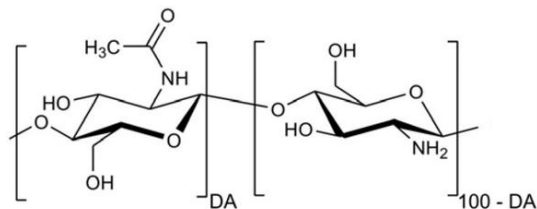
Figure 8: Partially acetylated chitosan. Adapted from [57]

Chitin is the second most abundant polysaccharide in the world and it is extracted from fungi, bacteria and exoskeleton of crustaceans such as crayfish, crab, shrimp and insects [56], [58]. The degree of conversion of acetyl groups, is given by the degree of de-acetylation (DD), which affects molecular weight, crystallinity, solubility, mechanical strength and biological properties [58].

The inherent properties of CHT, biocompatibility, biodegradability, anti-bacterial activity, non-toxicity, cellular compatibility and adhesive properties, and its adaptability to many shapes, such as films, microparticles, fibers and porous scaffolds, make it an extensively used biopolymer in biomedical and pharmaceutical applications, such as, wound healing accelerator, drug delivery systems, surgical suture, dental implants, artificial skin, bone and cartilage regeneration, corneal contact lenses, material encapsulation, artificial blood vessels, and for weight loss and blood cholesterol control. [58], [59]

CHT is neither soluble in organic solvents nor water at neutral or basic conditions but it may be dissolved in acidic conditions (pKa, approximately 6.3), using, for example acetic and formic acids, owing to the protonation of free amino groups, [56], [58], making CHT a suitable polycation at pH below its pKa, [59], [60] to be used in multilayer films. A positive zeta potential of +13.1 ± 0.3 mV was measured for CHT at a pH 5.5 [61].

However, CHT has poor mechanical properties [56], [58], solubility only in acidic conditions and low surface area, which may hinder the adsorption process [56] in the LbL assembly of multilayer films. Hence, many approaches have been described in the literature to overcome these drawbacks of CHT, either by chemical modification, easy approach due to the reactivity of the amine and hydroxyl functional groups, or by covalent and ionic cross-linking of chitosan [56]. For example, by adding methacrylic anhydride to acid acetic dissolved chitosan, the chitosan amine groups react

with the methacrylic anhydride to yield a water soluble chitosan, Methacrylamide chitosan (Met. CHT). [62]

Alginate (ALG) is another abundant low cost natural polymer, derived from brown algae. It is a linear block copolymer polysaccharide containing α-*L*-guluronate (G block) and β-*D*-mannuronate (M block) monomers (figure 9). [63], [64]
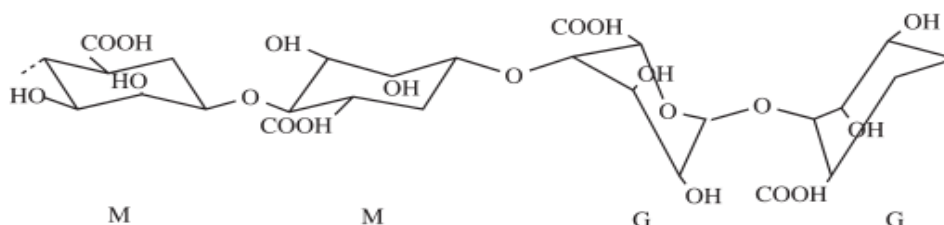
Figure 9: Alginate structure [1]

ALG has biocompatibility, non-immunogenicity [64], hydrophilicity, since it can be readily soluble in water [64], [65], but it has disadvantages, the poor biodegradability, as it cannot be naturally broken by enzymes, and the difficulty of cells to adhere to ALG [64].

ALG has known many applications, either in the biomedical industry, such as in drug systems or in cartilage tissue engineering, and also in the food industry [64], [65].

In solution, ALG is a polyanion at a pH above its pKa (between 3 and 4 [66]), due to the negatively charged carboxylic groups present in both G and M monomers [67], [68]. These interesting properties, make ALG a suitable polyanion to be used in this work to produce multilayer films by electrostatic interaction, resorting to the LbL technique. A negative zeta potential of -17.5 ± 1.5 mV was measured for ALG at a pH 5.5 [61].

2.5.   Graphene based Multilayer films

The Layer-by-Layer (LbL) technique is a versatile approach to produce multilayer films at nanometric scale, by simply alternating the deposition of a par of polyelectrolytes (PE), a polycation (PC) and a polyanion (PA) with opposite charges [69]. Therefore, the assembling of the bilayers is mainly achieved by electrostatic interactions. A representation of this technique can be seen in figure 10.
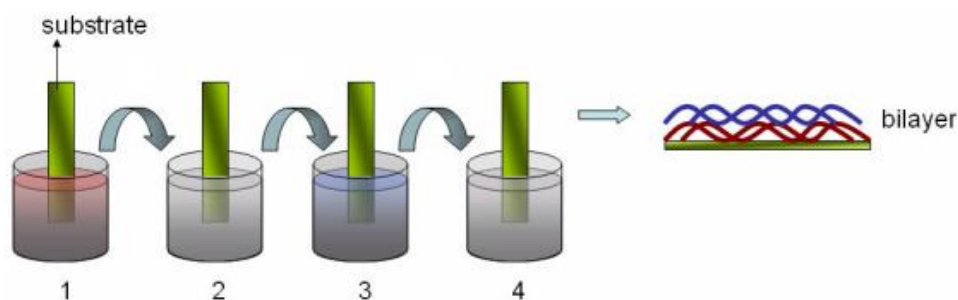
Figure 10: Representation of the LbL technique: sequentially, a positively/negatively charged substrate is introduced in a polyanion/polycation solution **(1)**, immersed in a washing solution **(2)**, introduced in a polycation/polyanion solution **(3)**, and again is immersed in a washing solution **(4)**, to form a bilayer. This procedure can be repeated as many times as desired to get a n number of layers. Adapted from [70]

Several multilayer films, produced through layer-by-layer deposition, based on graphene have been reported in the literature but literature on multilayer films based on graphene and natural polymers is still very scarce. The main proposed application has been biosensing [71]–[76] but dye-sensitized solar cells (DSCs) [77], low-friction and anti-wear coatings in MEMS or NEMS [78], electrochromic devices [79], and transistors [80], [81] have also been suggested. Some examples are briefly described below.

An LbL assembly of positively charged mixture of alcian blue pyridine (AB) with graphene and a negatively charged mixture of copper phthalocyanine-3,4',4'',4'''-tetrasulfonic acid tetrasodium salt (TSCuPc) with graphene permitted to produce a biosensor for glucose detection, since the multilayer film electrocatalytic activity significantly increased towards O_2 reduction. [71]

An LbL procedure used positively charged Prussian Blue (PB) nanoparticles protected by poly (diallyldimethylammonium chloride) (PDDA) and negatively charged polyacrylic acid (PAA) functionalized graphene. The obtained multilayer film was reported to be suitable for biosensing applications, as it presented elctrocatalytic activity towards H_2O_2 reduction. Graphene oxide was produced through the Hummers' method and it was reduced in an oil bath at 80 °C for 4 h. [72]

An assembly consisting in 2 bilayers of poly (diallyldiamine chloride) (PDDA) and poly (styrene sulfonate) (PSS), followed by 5 bilayers PDDA and graphene was made by LbL method, which then, suffered a SF_6 dry etching. The composite demonstrated to be capable of detecting prostate specific antigen with a very low detection limit. [73]

Alternate layers of Polyethyleneimine (PEI)-functionalized graphene and Prussian blue (PB) were used to build up a multilayer film suitable for electrosensing applications, with great electrochromic properties and good elctrocatalytic activity towards H_2O_2. This work used reduced graphene oxide (rGO). [74]

19

A biosensor consisting on a chitosan/graphene multilayer film coated glassy carbon electrode, was reported for detection of dopamine and uric acid. It presented great electrocatalytic activity towards oxidation of dopamine and uric acid. [75]

A multilayer film made of GO and another natural polymer, regenerated cellulose (RC), was reported to fulfil biosensing and tissue engineering applications. It was produced through LbL deposition due to hydrogen-bonding interaction between the GO oxygen containing functional groups and the hydroxyl groups in RC chains. GO was obtained through graphite using a modified Hummers' method. [76]

A counter electrode for dye-sensitized solar cells (DSCs) was produced with resort to the LbL technique using negatively charged GO and positively charged poly (diallyldimethylammonium chloride). GO was produced through graphite following a modified Hummers' method. [77]

Alternate layers of positively charged PEI and negatively charged poly (sodium 4-styrenesulfonate) - graphene sheets blend, were assembled by LbL deposition. The good tribological properties of these films suggest their potential for low-friction and anti-wear coating in MEMS or NEMS. Graphene oxide was produced by the Hummers' method and it was reduced in solution together with poly (sodium 4-styrenesulfonate) by hydrazine. [78]

Negatively charged GO and positively charged polyaniline (PANI) layers were deposited by means of electrostatic interaction, followed by the GO reduction. These composite films revealed a great potential as electrode materials for electrochromic devices. [79]

Zhu and Tour reported the production of GNRs thin films on silicon oxide and silicon surfaces, by electrostatic layer-by-layer absorption, between positively charged GNRs and negatively charged GNRs, and they were found to be good bottom gated GNR thin-film transistors. This appears to be an interesting technique, since it is done under ambient conditions [80]. Another more recent study on transistors, Organic Field-Effect Transistor, was reported by Ou et al. Alternative layers of GO and (3-aminopropyl) trimethoxysilane (APTMS) were covalently assembled in a layer-by-layer approach. APTMS is a covalent cross-linking agent, which lead to covalently grafted GO. This approach allowed to obtain highly stable films, with high stability and reproducibility. [81]

2.6. Biomedical Applications

Thanks to polymers, either natural or synthetic, mainly due to their biodegradability and biocompatibility, a wide range of biomedical applications have witnessed impressive improvements in the recent decades, such as in tissue engineering, drug delivery systems, biosensors, prosthetics and wound healing. [1], [82]

Some considerations of biosensors, tissue engineering of electrically responsive tissues and coatings for implants and devices, three of the potential applications of the multilayer films produced in this work, are discussed below.

2.6.1. Biosensors

A big effort has been made in biosensing research, seeking for low-cost, fast diagnostic devices, as well as for continuous metabolic monitoring, either for prevention or indication of body disorders and diseases. [83]

The utilization of miniaturized implantable biosensors may overcome painful procedures that not completely cover the overall trends of a disease, as in diabetes control, where a blood droplet obtained from a finger pricking is placed in a test strip. Other implantable biosensors are applied in nerve stimulation, relief of acute pain, detection of electric signals in brain, monitoring bioanalytes in brain, and drug delivery systems for controlled delivery at pain and stress sites. [83]

In a simple description, a biosensor integrates a selective interface, close to a transducer, responsible for transmitting information regarding to analyte/electrode surface interactions [2]. According to the transducing mechanism, biosensors can be labeled as resonant, optical-detection, thermal-detection, ion-sensitive FET, and electrochemical biosensors [2], being the last the most reported because of their design and construction simplicity [83], and sensing ability without damage of the host system [2].

Selectivity and sensitivity are important parameters of a sensor. Selectivity is defined as the capacity of a sensor to reply to a specified analyte within the several metabolites within the body, while sensitivity is defined as the extent of its response. The products of the electrochemical reaction may induce poisoning of the selective interface and consequently deterioration of the sensor sensitivity. The electrochemical cleaning of the selective interface is made by high potentials, resulting in loss of the biosensor selectivity, as well. [83]

The implantable biosensors success, miniaturization and reliability depends on foreign body response, sensor drifts and temporal resolution. Within a few hours or days, following sensor implantation, tissue inflammation due to the presence of the implantable sensor in the body, and foreign body response, resulted by fibrous confinement of the implanted sensor, a body's natural response to protect the tissue in contact with the foreign body might occur. This biofouling phenomenon may lead to a defective response of the sensor. The use of biocompatible and non-toxic materials are an adopted approach to address this problem. [83]

Nanomaterials, such as metallic and metallic alloy nanoparticles, nanowires, CNTs, carbon nanofibers and graphene, have been used to overcome such issues, mentioned above [2]. However, for example, while metallic nanoparticles present inconstant signal amplification and CNTs impurities induce toxicological hazards [2], graphene prevents these problems and present great physicochemical properties suitable for biosensing applications, high surface area, fast electron transport, high thermal conductivity, great mechanical flexibility and biocompatibility [2], [3].

Most of the graphene based biosensors use rGO, as the high concentration of functional groups and defects is capable of fast electron transfer between analyte and electrode surface. [2], [3]

Reduced GO based biosensors have been reported to detect dopamine (DA), glucose, dihydronicotinamide adenine dinucleotide (NADH), hydrogen peroxide (H_2O_2), amino acids, and ascorbic acid (AA) [3], [84], as already discussed in section 2.5.

2.6.2. Electrically Responsive Tissues and Devices

Tissue engineering intends to regenerate or repair lost or injured tissues, using biomaterial scaffolds, cells, and growth factors. The scaffold should fulfill certain requirements, such as mimic the properties and structure of the organ, and serve as a support of cell survival and growth. [85]

Many cell types such as cardiomyocytes, neurons, and osteoblasts respond to electrical signals and thus, tissue engineering of electrically excitable tissues such as skeletal muscle, nerve, cardiac tissue, and bone, might be viable. For that, conductive materials, like conductive polymers (CPs) are needed [85]. CPs have experienced innumerous applications, such as biosensors, neural implants, drug delivery devices and tissue engineering scaffolds [86]. Some of them are PANI, polypyrrole (PPy), poly(3,4-ethylenedioxythiophene) (PEDOT), and polythiophene (PTh) derivatives. [86], [87]

Neuronal Probes consist in an array of electrodes that are implanted into the brain to stimulate and record signals of the immediate neurons. These electrodes need an interface capable of transmitting electrical signals between the tissue and the electrode to control external devices like robotic arms [85]. Neural probes are currently used in many clinical settings for diagnosis of brain diseases such as Parkinson's disease, dystonia, epilepsy, and major depression. [88]

Several issues regarding biocompatibility and long-term use of CPs have been reported. It was reported a decrease performance along the time in a neuronal electrode, characterized by the decrease of neuronal signal recording and charge deliverance, attributed to severe inflammation reactions, as glial scar formation and electrode encapsulation. Biocompatibility is pointed to be the key issue, as it could prevent adverse foreign body response. [86], [87]

Controlled thickness and topography of CPs thin conducting films may enable the use of these films as coatings of neural electrodes, to decrease electrodes impedance and enhance their integration in the host body. These conducting films may contain biological molecules, growth factors, and anti-inflammatory drugs, to overcome inflammatory reactions and protein adsorption. The entrapment and delivery of agents/drugs have been using several approaches, using carries like micelles, nanotubes, and nanocapsules, entrapment and adsorption techniques, covalent attachment and doping techniques. However, the induced chemical modifications may cause worse mechanical, chemical and conductive properties, which may be a substantial limitation in the CPs use. Biocompatibility and long-term functionality were reported to be improved through modification of the surface topography, by increasing the surface area and roughness. [86], [87]

Conductive polymers are not inherently biodegradable but it can be enhanced by mainly three routes. Composite films made by mixing the conductive polymers, like PPy or PTh, with biodegradable polymers, like PLA and PLLA, have been successfully accomplished, but it cannot remove the non-degradable polymer after the biodegradable degradation, yet the conductivity and degradation rate may be controlled by the ratio of the two polymers. The conductive polymer can also be modified by adding ionizable or hydrolysable side groups to the backbone of PPy and the last, electrochemically synthesized small chains of PPy can suffer gradual erosion and renal clearance due to their small size. [86]

It is thought that many of the studies reporting reduced biocompatibility might be a cause of incomplete cleaning of by-products of the polymer synthesis. PPy should be fully biocompatible if enough steps of rinsing and extraction are accomplished, to remove impurities, reactants,

monomers and shorter oligomers. PANI is generally cytocompatible, it supports neural cell growth, offer satisfactory proliferation and adhesion and does not cause severe inflammation. However, other studies described unsatisfactory cell adhesion and growth, tissue incompatibility and fibrous tissue formation. Also as PPy, it is thought that PANI cytotoxicity comes from residual dopants and low molecular weight by-products. [86]

PEDOT has generally presented good biocompatibility but PEDOT coatings revealed to be prone to *in situ* delamination after log-term implantation, which was overcome by using CNTs as dopant at PEDOT polymerization, to improve structural strength and biocompatibility. CNTs were also used together with PPy in a multilayer film, showing enhanced chemical, mechanical and electrical properties. Both coatings were suitable for coatings of neural electrodes. [86], [87]

Another interesting application of conductive materials, either CPs or conductive particles, as carbon or gold based particles, is tissue engineering of electrically responsive tissues, such as cardiac tissue, using biomaterial scaffolds as a main vehicle, which in the majority of the applications are electrically resistant, and thus the applications of such materials may provide significant improvements on scaffolds performance, by modulating cellular behavior, through transmission of electrical signals, provided from an external source. [85]

However, the use of carbon and gold based particles may induce some concerns, as they are non-biodegradable and their long-term effect *in vivo* is unknown. As they are not soluble, homogeneous distribution in composites materials is also hard to obtain. It is accepted that CPs offer a viable alternative, since they are organic-soluble and so they can be blended with other polymers to produce, for example porous scaffolds, through electrospinning, resulting in a good transmission of the electrical signals through the entire composite. [85]

PANI is a conductive polymer with interesting properties, biocompatibility, conductivity, processability, and antibacterial effect, to be used either as a composite scaffold or as a coating material of resistive scaffolds. Through a combination of self-assembly and surface polymerization, a PANI film was produced with long-term cytocompatibility. This technique provides an enormous potential of this coating to be used as coating of scaffolds. [85]

The use of a graphene based coating in electroactive scaffolds was also reported. The film was produced through the layer-by-layer technique, using graphene-heparin polyanion and poly-L-lysine (PLL) polycation, to cover 2D and 3D scaffolds made of poly-ε-caprolactone (PCL) nanofibrous, produced by electrospinning. Graphene was in the form of rGO. PLL is a natural polypeptide with

great cell adhesion properties and heparin is an extremely negatively charged polysaccharide, with anti-inflammatory and antiadhesive properties. The resultant graphene coated scaffolds revealed to provide neuron cell adhesion and neurite growth. [89]

The incredible structural properties of graphene, already discussed in this chapter, together with its almost neglected cytotoxicity, when compared with CNTs, make it a promising material for tissue engineering and prosthetics [89]. The LbL is also an important strategy in this and in the work mentioned above, since it can be used to produce coatings over an irregular and detailed surface.

2.6.3. Coatings for Implants

For years, researchers studied inert materials for implants to avoid cell - implant interactions, since it was believed that the body could tolerate the implant, as inflammation was not observed due to fibrous encapsulation. Later it was comprehended that by modulating cell responses, it could enhance the biomaterial integration and the implant performance. [90]

Two different types of modulated responses for more biocompatibility are described in the literature: passive responses, where non-fouling coatings are applied and active responses, where anti-inflammatory agents are incorporated into the coatings to be delivered at the cell/implant interface. [90], [91]

It is commonly accepted that by decreasing bio-fouling, leukocyte activation and tissue fibrosis can be eluded, preventing severe inflammation. This passive strategy is a simple technique but some disadvantages were noticed, lack of stability by displacement of other proteins like albumin. Polyethylene glycol (PEG), poly(2-hydroxyethyl methacrylate), poly(N-isopropyl acrylamide), poly(acrylamide), poly(ethylene oxide) (PEO) and ALG are known polymers to resisting protein adsorption. Even though these polymers present low *in vitro* protein adsorption and leukocyte adhesion, *in vivo* experiments have presented incoherent results on acute and chronic inflammatory reactions, which might be due to reduced non-fouling properties, coating degradation, independent inflammatory mechanism on protein adsorption. Thus, anti-inflammatory strategies were further developed. [90], [91]

Orally administrated drugs may be in a defective concentration in the site of need and their long-term use may lead to relevant side effects. The incorporation of drugs in implant coatings is an accepted active approach to bridge inflammatory responses. Many approach have been presented to agents/drugs delivery, passive diffusion from coatings, polyelectrolyte layers, bioerodible or

biodegradable coatings, passive mechanisms from swelling coatings, and hydrolysable or enzyme-degradable linkages to the agent/drug. [91]

Several materials have been used in implant coatings, to improve either corrosion resistance [92], [93], inflammation resistance [90], [91], or antimicrobial resistance [94].

For most applications, for instance, in temporary implants applications like pins, wires, screws, plates, and stents, biodegradable and biocompatible coating materials are preferred over the non-degradable coating materials, since it would be possible to avoid a second surgical operations to remove the implant, once the tissue is regenerated or healed [92], [94].

The possibility to tailor the biodegradability, biocompatibility and other properties of synthetic polymers, through synthesis parameters or through composites, by mixing the polymer coating material with other chemicals or biodegradable polymers (poly-l-lactic acid (PLLA) and poly(lactide-co-glycolide) (PLGA)), make them the most polymer coating materials used in cardiovascular and orthopedic implants. [93]

The use of natural polymers as coating material for implants was already reported in the literature, chitosan and collagen in stents, revealing good biocompatibility, and in orthopedic tissue engineering, glycine-phenylalanine-hydroxyproline-glycine-glutamate-arginine (GFOGER) in orthopedic tissue healing or bone repair, and bacterial cellulose (BC) in vascular grafts or replacement, wound healing and scaffolds for tissue engineering. However, chitosan and collagen presented an immunological response, but BC revealed to be very promising as a coating material for implants due to its high mechanical strength, high water content, good biocompatibility and non-toxic properties. [93]

Chapter 3

Materials and Experimental techniques

This chapter, Materials and Experimental techniques, lists those reagents and materials used to conclude this work, and the methods used to produce all different kinds of graphene and multilayer films. Lastly, techniques for graphene and multilayer films characterization are further described.

3.1. Materials

This work used MWNTs NC7000 from Nanocyl™ and EG Micrograf® HC11 from Nacional de Grafite Ltda.

The functionalization applied to the EG used Paraformaldehyde (reagent grade) from Sigma-Aldrich, amino acid *N*-benzyloxycarbonylglycine, 98.5% from Acrós Organics and diethyl ether stabilized with ~6ppm BHT from Panreac. The washing was made using absolute ethanol from Fisher Scientific UK, commercial hexane (benzine) from JMS and acetone from Pronalab.

For the oxidation of EG and MWNTs the reagents used were sulfuric acid 95-97% (analytical reagent) from Riedel-de Haën, potassium permanganate analytical reagent grade from Fisher Scientific UK, distilled water, hydrogen peroxide (reagent grade) from Fisher Chemical, absolute ethanol from Fisher Scientific UK, and hydrochloric acid S.G. 1.18 from Fisher Scientific. Additionally, it was used diethyl ether stabilized with ~6ppm BHT from Panreac on the oxidation procedure of MWNTs.

The study of the best deposition technique for graphene analysis through STM used the substrates Au coated Si, Au coated mica and HOPG (Grade SPI-1 from SPI supplies).

Au coated Si substrates were cleaned with piranha solution, using sulfuric acid from Sigma-Aldrich and hydrogen peroxide 33% from VWR. The piranha solution was washed using isopropanol, 2-Propanol z. A. from CHEMSOLUTE®.

For sample temperature control on UHV-STM, a Chromel/ Alumel thermocouple from ADVENT Research Materials Ltd was used.

For the production of the multilayer films it was used Sodium Alginate FEMA 2015 from SAFC, absolute ethanol from Fisher Scientific UK, distilled water, medium molecular weight chitosan from Sigma-Aldrich, which was also used in the production of Met. CHT in the 3B's Research Group, Elastin-like polymer ELP IK24 synthetized in a partnership between 3B's Research Group and BIOFORGE (Valladolid, Spain), hydrochloric acid 37% from VWR, sodium hydroxide pellets from EMSURE® and acetic acid 100% from VWR.

3.2. Graphene Production

In the present work graphene was produced by applying two different chemical methods to MWNTs and to EG.

The first method consists on chemical functionalization of the raw material, MWNTs and EG, and further unzipping and exfoliation of the functionalized MWNTs (f- MWNTs) and functionalized EG (f-EG), respectively, in ethanolic solution, induced by sonication. This method was used for the functionalization of the CNT that originated the graphene formation, observed under STM imaging [49].

The covalent functionalization was a 1,3-dipolar cycloaddition reaction carried out at 230 $^\circ$C for 5 hours. 3 g of amino acid, 20 ml of diethyl ether, 2.1 g paraformaldehyde, 50 ml of diethyl ether and 3 g of EG were put in a 2-neck round bottom flask, accordingly to the order of the mentioned materials. Between each addition, the materials were mixed by magnetic stirring. When everything was mixed, the temperature was raised to 40 $^\circ$C to boil away the solvent, diethyl ether. When the solvent evaporation was completed, assured by a temperature increase above 40 $^\circ$C (measured with the thermometer inserted in the 2-neck round bottom flask) the temperature was increased to 230 $^\circ$C and the reflux apparatus was set-up for 5 hours.

After cooling, the f-EG was collected, put into a beaker and it was washed. A sequence of solvents was used: ethanol, hexane, acetone and ethanol, three times each solvent, 150 ml at each time. Each washing step was accomplished by a 2 to 3 minutes of magnetic stirring and vacuum filtration.

In this work, the functionalization was applied only to EG, once there were already f-MWNTs available from a previous work of the same work group.

The conditions to produce f-GNRs from f-MWNTs were already set-up in a previous work and 50 samples containing approximately 120 mg of f-MWNTs in 40 ml of ethanol (concentration of 3 mg/ml) were produced by exposure to 10 minutes of sonication (ultrasonic bath Ultrasonics from Crest).

In the case of f-GFs produced through f-EG, 4 different initial concentration of f-EG were tested – 1, 2, 3 and 4 mg/ml – by using approximately 40, 80, 120 and 160 mg of f-EG in 40 ml of ethanol. Only 2 different times of sonication (same equipment as above) were tested, 10 and 15 minutes, once longer sonication time may cause GFs breakage [95].

After exposure to ultrasounds the solutions were filtered by gravity filtration and collected to 50 ml volumetric flasks.

This method is illustrated in figure 11.

Figure 11: f-GNRs or f-GFs production illustration: **(a)** functionalization reaction of MWNTs or EG to obtain f-MWNTs or f-EG, respectively, **(b)** mixture of f-MWNTs or f-EG with ethanol, **(c)** sonication of f-MWNTs or f-EG solutions, **(d)** resultant solution after sonication containing f-GNRs or f-GFs, **(e)** gravity filtration of the solutions in (d)

Oxidized GFs (o-GFs) were produced by a modified Hummers' method by extensive oxidation of EG by H_2SO_4 and $KMnO_4$. 2 g of EG were poured into a round bottom flask and 100 ml H_2SO_4 was added and magnetic stirred for 15 minutes in an ice-bath. 6g of $KMnO_4$ were added slowly during 1 hour. The mixture was removed from the ice-bath and let to stir at room temperature for 1 hour.

The oxidation was followed by a purification procedure. 300 ml distilled water (DW) and 5 ml H_2O_2 were added to the mixture in an ice-bath (the mixture color changed from black to brownish when DW was added and to yellowish when H_2O_2 was added). The mixture was centrifuged and the solid was collected. It was followed by addition of 150 ml DW, stirred for 30 minutes and centrifuged to collect the solid. Then, 150 ml HCl (20% vol.) was added, stirred for 30 minutes and centrifuged. Afterwards 150 ml ethanol was added, stirred for 30 minutes and centrifuged. The addition of DW and centrifugation were repeated over and over again until a pH between 6 and 7 was observed. Every centrifugation steps was carried at 10 000 rpm for 3 minutes in a centrifuge Universal 320 from Hettich.

31

The resultant o-EG were dried for 78 hours at 100 °C and then milled using an Agate mortar and pestle. The resultant powder was evaluated by TGA.

The o-EG powders (1.9458 g) were dispersed in 400 ml DW and exposed to ultrasound for 2 hours. The mixture was centrifuged for 10 minutes at 8000 rpm but UV-Vis spectroscopy analysis revealed no evidence of o-GFs. The remaining o-EG set apart by the centrifugation step was dispersed once more in 400 ml DW and exposed to plus 2 hours sonication.

Some steps of the EG oxidation procedure, where is possible to see the variation of the solution color, are illustrated in figure 12.
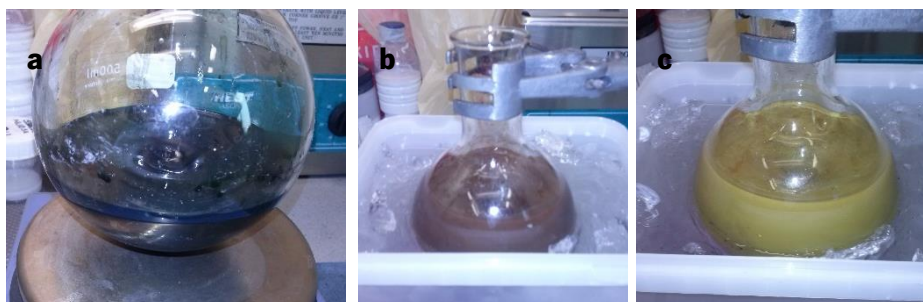
Figure 12: EG oxidation: **(a)** magnetic stirring of a mixture of EG, H_2SO_3 and $KMnO_4$ at room temperature, after stirring in an ice bath while adding $KMnO_4$, **(b)** magnetic stirring of a mixture of EG, H_2SO_3, $KMnO_4$ and DW in an ice bath, **(c)** magnetic stirring of a mixture of EG, H_2SO_3, $KMnO_4$, DW and H_2O_2 in an ice bath

MWNTs were oxidized by another approach, a more aggressive oxidation process, similarly to the method described by Kosynkin and coworkers [53].

1g of MWNTs were added in 250 ml H_2SO_4 and stirred for 12h. 6g of $KMnO_4$ was added and magnetic stirred for 1h. The mixture was heated to temperatures ranging from 55 to 70 °C for 1h. The state of the reaction was checked by 2 tubes test, test 1 containing 1 ml DW and test 2 containing 1 ml DW and 3 drops of H_2O_2. 5 drops of the MWNTs mixture were poured into each tube test and sonicated for 3 minutes. In case of reaction complete, it was expected to see a reddish color in test 1 and yellowish/brownish color in test 2. It was not observable and so, the mixture was kept between 55 and 70 °C for 1 more hour. These tests were repeated 3 times and then, the mixture was left to reflux overnight, reaching a maximum temperature of 100 °C, completing a total time of heating of 18 hours.

After cooling to room temperature, a purification procedure was accomplished. 400 ml DW and 25 ml H_2O_2 were added to the mixture in an ice-bath and filtered. Then, again, 400 ml DW were added, magnetic stirred for 30 minutes and exposed to sonication for 20 minutes. 150 ml of HCl (20% vol.) were added and centrifuged. It was followed by addition of 400 ml ethanol, magnetic stirred

for 30 minutes and exposed to ultrasounds for 20 minutes. Diethyl ether was added 3 times, first 400 ml and then 150 ml was added twice. It was centrifuged at each time diethyl ether was added. The o-MWNTs were left to dry for 43 hours at 80 °C.

The result of this procedure was 0.2206g o-MWNTs and 0.1778 g o-MWNTs were dispersed in 100 ml DW and exposed to sonication for 30 minutes. o-GNRs were then collected by centrifugation.

UV-Vis spectroscopy was used to prove the presence of graphene in those solutions obtained.

A picture of each type of graphene solution is presented in figure 13.
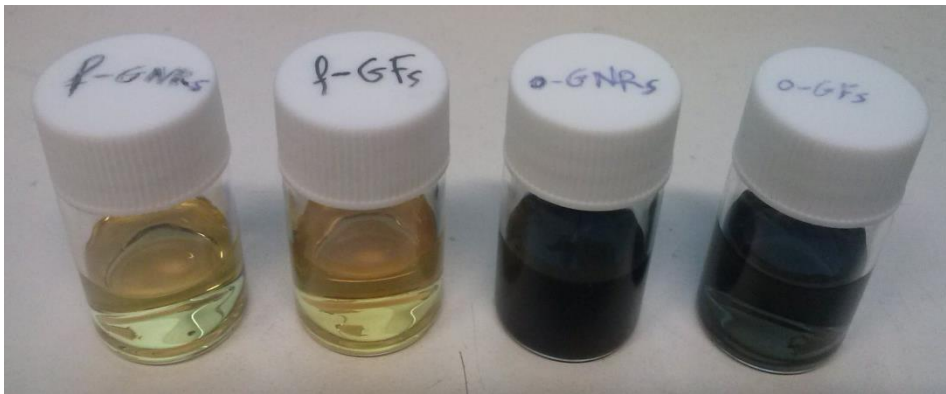
Figure 13: Graphene solution samples, f-GNRs, f-GFs, o-GNRs and o-GFs, from left to right

The o-GNRs and o-GFs are presented as obtained, while f-GNRs and f-GFs are presented after solution concentration by solvent evaporation.

3.3. Characterization of graphene

3.3.1. Ultraviolet-Visible Spectroscopy

UV-Vis spectrometer is able to detect electron transitions that may occur due to exposure to radiation with wavelength between 200 and 800 nm. [96]

In a double-beam UV-Vis spectrometer, a UV-Vis light beam is divided into 2 parallel UV-Vis light beams to pass across two cells placed in parallel (reference cell, with solvent, and sample cell with the solution to be studied). A detector measures the intensity of the transmitted light through both cells, aiming to quantify the absorbance A, given by equation (1). [96]

$$A = log_{10} \frac{I_0}{I}$$ (1)

Where I_o is the intensity of the light transmitted through the reference cell and I is the intensity of light transmitted through the cell containing the sample. [96]

UV-Vis spectroscopy is frequently used to quantify solutions concentration [96], according to the Beer-Lambert law, presented in equation (2) [96], [97].

$$A = \mathcal{E}lc \qquad (2)$$

Where $\mathcal{E}$ is the absorptivity coefficient, characteristic of each type of chemical group absorbing in the UV-Vis range, and may be reported in molar or weight units, depending on the units of the solution concentration, c, and l is the path length of the cells. The Beer-Lambert law is generally accepted as valid for absorbance values lower than 1. [96], [97]

UV-Vis spectroscopy analyses were performed in a UV – 2401 PC from Shimadzu, aiming to quantify the solutions concentrations and follow the graphene production, proving its presence in those solutions.

The solution concentration cannot be determined if $\mathcal{E}$ is not known. Arranging equation (2) into equation (3), $\mathcal{E}$ can be determined by the slope of the line A/l vs. c.

$$\frac{A}{l} = \mathcal{E}c \qquad (3)$$

The line A/l vs. c can be plotted by performing UV-Vis spectroscopy analysis for a single sample diluted several times, by adding exact volumes of solvent. The solute weight must be measured to calculate c at each dilution. In the present work, the graphene solution used to calculate $\mathcal{E}$ was evaporated into aluminum crucibles on a hot plate and the aluminum crucibles mass was measured before and after evaporation of graphene solutions in a PERKIN-ELMER AD-4 Autobalance with a resolution of 0.1 µg.

3.3.2. Infrared Spectroscopy

Infrared (IR) radiation, corresponding to wavelengths ranging from 2500 to 15 000 nm in the electromagnetic spectrum, usually expressed in wavenumbers ranging from 4000-400 cm^{-1} in *IR* spectroscopy, is responsible for transitions between vibrational energy levels of molecules, by stretching or bending of bonds [96]. Those transitions are characteristic of each molecule, once they depend on the relative masses of the atoms, bond strength, atoms geometry and dipole moment in the molecule and, so they may be detected [98].

In a modern IR spectrometer, an IR radiation source is used to irradiate the sample in a single pulse of radiation, covering all the wavenumbers of IR radiation at once. Once a single beam is used in modern IR spectrometers, the analysis must start by collecting a background spectrum (to remove, for example, the contribution of carbon dioxide and atmospheric water), which is then subtracted to the sample spectrum. A detector can measure the energy absorbed by the molecules at each frequency. [96]

A Spectrum 100 FTIR Spectrometer from PerkinElmer was used to study the covalently bonded species on f-GNRs and f-GFs. Two NaCl cells were dried in an oven at 80 °C, for 72 hours before and 70 hours after deposition of the f-GFs and f-GNRs solutions, containing 1 mg graphene each.

The covalently bonded species on o-GNRs and o-GFs were studied in a 4100 Fourier Transform Infrared Spectrometer from Jasco. o-GNRs and o-GFs solutions were deposited in glass substrate and the water was evaporated in a hot plate. A film of each kind of graphene was formed, which were scraped off with a spatula and a powder was obtained. The powders were placed on an ATR crystal for analysis.

3.3.3. Thermogravimetric Analysis

Thermogravimetric Analysis (TGA) is an important technique to study the decomposition behavior of materials at different temperatures, weather the material is subject to heating at controlled rate in a specific atmosphere or to isothermal conditions for a certain time. [99]

TGA studies were carried out in a Q500 from TA Instruments to quantify adsorbed and covalently bonded species on functionalized and oxidized MWNTs and EG (f-MWNTs, o-MWNTs, f-EG, o-EG) and functionalized and oxidized GNRs and GFs (f-GNRs, o-GNRs, f-GFs, o-GFs). Every TGA analyses were carried out in a temperature range between 100 and 800 °C, with 1 minute isothermal period at 100 °C and 10 °C/min heating rate, under a nitrogen atmosphere.

3.3.4. Scanning Transmission Electron Microscopy

A Scanning Transmission Electron Microscope (STEM) operates according to the same principles of a Scanning Electron Microscope (SEM). An electron beam is focused by a series of condenser lenses and an objective lens and then, scanned over the sample to form an image by collecting those electrons transmitted through the specimen. Several kinds of signals may be collected by different types of detectors to form different images containing different information. [100]

This technique requires quite thin specimens to enable electrons transmission but the sample preparation procedure for nanometric materials is much easier by simply depositing the nanomaterial on a thin holey carbon film on a copper grid [100]. In the present work, the different 4 kinds of graphene were analyzed by STEM by dipping carbon coated TEM grids into the 4 different graphene solutions.

The STEM analysis aim to look for insights of the graphene distribution, shape and size, in order to facilitate the STM analysis.

Nova NanoSEM 200 from FEI in transmitted electrons mode was used for STEM observations. An EDS detector was also available to elemental analysis of f-GNRs, f-GFs and o-GFs samples.

3.3.5. Optical Microscopy

Optical Microscopy (OM) has played an important role on graphene research since it was possible to observe a single layer graphene on a SiO_2 coated Si wafer using an optical microscope, by Novoselov and coworkers in 2004. [5], [101]

An optical microscope uses, in its simplest form, 2 different kinds of lenses to form an image. The condenser lens is responsible for focusing the light, which source is called illuminator, in a small area of the sample, while the objective lens collects the diffracted light resultant from the light interaction with the specimen and forms the magnified image.

The use of the optical microscope in this work intended to evaluate the graphene deposition techniques and validate them either for AFM or STM analysis.

An optical microscope Eclipse Ci-L from Nikon was used, equipped with a Differential Interference Contrast (DIC) prism using polarized light in bright-field mode.

3.3.6. Atomic Force Microscopy

Atomic Force Microscopy (AFM) is one of the SPM techniques along with STM, and its development aimed to overcome the impossibility to analyze insulator materials by STM. [102]

AFM can be divided into two different operational modes, static and dynamic AFM. The dynamic AFM mode is characterized by the oscillation of the cantilever at its resonance frequency when scanning the sample, while in the static AFM mode the cantilever is quasi-static when scanning the

sample. Dynamic AFM may achieve better signal-to-noise ratio and better resolution, when compared to static AFM. [103]

Generally, in an AFM set up, a cantilever holding a tip at one of its ends is scanned over the surface. A laser beam is focused on the cantilever, right above the tip. The surface-tip interactions are measured and detected by the reflected laser beam, which is driven by a mirror to a photo-diode. [103]

Those sample-tip interactions, vertical bending, lateral bending, torsion and extension are modeled considering a rectangular shaped cantilever equivalent to a 3D beam with clamped-free boundary conditions and thus, an image of the scanned surface is built. Both tapping mode (TM) and non-contact AFM (NC-AFM), are governed by vertical bending of the cantilever, which motion is provided by vertical harmonic induced on its holder [103].

The easyScan 2 FlexAFM from nanoSurf was used in this work, using dynamic TM-AFM for the study of the deposition techniques of graphene solution. Data manipulation was carried out using the software Gwyddion [104] being possible to study samples roughness and built 3D views.

3.3.7. Scanning Tunneling Microscopy

A Scanning Tunneling Microscope (STM) is a very powerful equipment to analyze surfaces of conductive samples at atomic scale. Basically, it works because electrons from the sample may tunnel through a very tinny vacuum barrier between the sample and a sharp tip (or vice-versa), thus both sample and tip must be conductive. [105]

For this tunneling transport to happen, electrons have to be removed from one solid, usually the sample, go into the second solid, usually the tip, passing all the way through the vacuum barrier. Energy with same value as the work function, which is the difference between the Fermi energy of the solid and the energy at the vacuum level, is needed to pull out the electron of the atom to the vacuum barrier with zero kinetic energy. When the two solids are separated by a distance ranging between 1 and 5 nm, the decay length of electronic states in vacuum, electrons may enter into the second solid. These electrons from one of the metals will pass across the vacuum barrier to the other metal and this tunnel current will stop as soon as the Fermi levels of both metals are aligned. However, if a bias is applied to one of the metals, the Fermi level is no longer aligned and a tunnel current between the metals is developed. [105]

The STM can be set up to two different modes, constant current mode or constant height mode, being the first the most used one. [105]

The constant current mode is provided by a feedback mechanism which compares the set and measured tunneling current at each pixel and acts on the z-piezo by applying a voltage in order to keep a constant sample-tip distance. This mode is suitable for high corrugation samples and for high scanning areas. [105]

STS, Scanning Tunneling Spectroscopy can be used in parallel to STM, for probing the DOS, useful for band-gap determination. For that, the STM tip is stopped under a spot of choice and the feedback loop is switched off. The tunneling conductance, dI/dV, is recorded as a voltage range is applied to the sample. [105]

STM images were recorded using an Aarhus air-STM and an Aarhus UHV-STM, using Pt/Ir tips, and a Createc Low Temperature-STM (LT-STM), using a gold tip. All images were acquired in constant current mode. The Createc LT-STM was also used for STS experiments.

This STM study intended to look for insights of the functional groups distribution, as well as, the atomic and electric characterization of f-GNRs.

3.3.7.1. *Study of graphene deposition technique and substrate for STM analysis*

As described in section 4.5, after STEM analysis, f-GNRs were chosen for STM analysis, as they are flat.

Different deposition techniques were tried on Au coated Si substrates to find the best one for graphene deposition for STM analysis. Every sample prepared was analyzed by OM and the best samples were further analyzed by AFM. A summary of the samples prepared, deposition method, deposition parameters and substrates, is presented in table 1.

AFM allowed to choose the most suitable sample for STM studies, regarding to corrugation, distribution and graphene patches size. The graphene patches density should be the highest possible to increase the probability and easiness to find graphene patches in STM.

Piranha solution, a mixture of 2ml H_2SO_4:1ml H_2O_2, was used to remove organic residues from Au coated Si substrates. The piranha solution was removed afterwards by isopropanol and the substrates were dried by an inert gas flow.

Varying the number of deposition cycles between 1 and 4, four samples were prepared by spin coating (SC): SC.1X.3500, SC.2X.3500, SC.3X.3500 and SC.4X.3500, same order as mentioned. At each deposition cycle, 2 droplets of a 2.2 mg/ml concentrated f-GNRs solution were dropped onto the substrate and a rotation speed of 3500 rpm and 30 seconds spinning time was used. All samples were analyzed by OM but only SC.4X.3500 was analyzed through AFM.

Later, 2 more samples were prepared by spin coating: SC.7X.2000 and SC.7X.3500. Both samples were prepared by 7 deposition cycles, with 2 droplets of the same f-GNRs solution, 30 seconds spinning time at each cycle, varying the rotation speed, 2000 and 3500 rpm, respectively. SC.7X.3500 was analyzed by OM and further coated until complete 12 deposition cycles (SC.12X.3500).

1 ml of 2.2 mg/ml concentrated f-GNRs solution was evaporated to further concentration to a final concentration of 11 mg/ml. This concentrated f-GNRs solution was used to prepare 2 spin coated samples, 2 droplets for each sample, one using 2000 rpm (SC.1X.2000.11) and the other one using 3500 rpm (SC.1X.3500.11). Both samples were subject to a single spin coating cycle of 30 seconds. They were analyzed by OM and AFM.

A Spin Coater from HRL Headway Research, Inc. was used.

Two samples were prepared by droplet deposition (DD) on a hot plate (HP), using the 2.2 mg/ml concentrated f-GNRs solution: DD.HP.0.2 and DD.HP.0.4. To achieve that, 0.2 and 0.4 ml of f-GNRs solution was deposited using a volumetric pipette. Both samples were analyzed only through OM, once the heat provided by the hot plate could compromise the graphene quality by damage of the functional groups. It was possible to observe that the samples appeared to be burnt.

To avoid damage of the functional groups, another sample was prepared by droplet deposition using a volumetric pipette, at room temperature, with 0.4 ml volume of the 2.2 mg/ml concentrated f-GNRs solution, DD.RT.0.4. Since the ethanol evaporation was carried out slowly at room temperature, for each droplet deposited the graphene could be dragged during evaporation and deposited towards the edge. In the end, the sample looked quite inhomogeneous and rough.

Two more samples were prepared by droplet deposition at room temperature using a syringe (S) instead, as smaller droplets could be deposited: DD.0.2.S and DD.10drp.S. DD.0.2.S was prepared by droplet deposition of 0.2 ml and DD.10drp.S by droplet deposition of 10 droplets (drp) of the 2.2 mg/ml concentrated f-GNRs solution. Those samples were analyzed by OM and AFM.

One sample was prepared by simply dipping the substrate into the 2.2 mg/ml concentrated f-GNRs solution (DIP) and left to dry at room temperature. It was analyzed by OM and AFM.

SC.1X.3500.11 seemed to be the most suitable sample to be analyzed by STM and then tried out in an air-STM.

A 7x7 mm Au coated mica (SC.1X.3500.11.mica) and freshly cleaved HOPG (SC.1X.3500.11.HOPG) substrates were also coated as SC.1X.3500.11 sample on Au coated Si. These samples and the reference clean substrates were analyzed in the same air-STM. SC.1X.3500.11.HOPG was also scanned on UHV-STM.

2 more samples of f-GNRs on HOPG were prepared. One sample was prepared by droplet deposition of a single droplet of the 2.2 mg/ml concentrated f-GNRs solution and evaporation in an oven heated at 100 °C (DD.1drp.2.2), and another one by droplet deposition of 2 droplets of a freshly produced 1 mg/ml concentrated f-GNRs solution (DD.2drp.1) and evaporation in a hot plate. DD.2drp.1 was analyzed by OM after deposition of the first droplet and since graphene was barely seen, the second droplet was deposited. Both were analyzed by air-STM and, later on, DD.2drp.1 was annealed at 200 °C for 20 minutes for UHV-STM scanning.

Sometimes it was difficult to distinguish between HOPG steps and f-GNRs due to their atomic structure similarities, Au(111) crystal substrate was expected to overcome this problem.

An Au(111) substrate was cleaned by sputtering for 30 minutes, annealed at 500 °C for 5 minutes and 10 minutes sleeping after annealing, in 16 full repeated cycles. The cleaning state of the Au(111) substrate was checked by scanning on UHV-STM.

One droplet of the 1 mg/ml concentrated f-GNRs solution was used to coat the Au(111) substrate by droplet deposition in a hot plate (DD.1drp.1.Au). It was deposited only 1 droplet due to the smaller size of the Au(111) crystal when compared to the 7x7 mm HOPG substrate. The sample was first analyzed by air-STM and later by UHV-STM. Prior to UHV-STM scanning, the sample was annealed at 200 °C for 5 minutes.

For STS analysis in the LT-STM, 1 droplet of the 1 mg/ml concentrated f-GNRs solution was deposited in a HOPG substrate, in a hot plate. Again, it was used only 1 droplet because of the reduced size of the HOPG substrate. The sample was annealed at 200 °C for 5 minutes and cooled down to 77 K, by liquid nitrogen for sample scanning.

Table 1: Summary of samples prepared for deposition technique study

			Spin coating (SC)		
Sample	**Number of cycles**	**rpm**	**Solution concentration**	**Solution volume**	**Substrate**
SC.1X.3500	1				
SC.2X.3500	2	3500			
SC.3X.3500	3				
SC.4X.3500	4		2.2 mg/ml		Au coated Si
SC.7X.2000	7	2000		2 droplets (drp)	
SC.7X.3500	7	3500			
SC.12X.3500	12				
SC.1X.2000.11		2000			
SC.1X.3500.11	1		11 mg/ml		
SC.1X.3500.11.mica		3500			Au coated mica
SC.1X.3500.11.HOPG					HOPG
			Droplet Deposition (DD)		
Sample	**Deposition tool**	**Solvent evaporation**	**Solution concentration**	**Solution volume**	
DD.HP.0.2		Hot plate (HP)		0.2 ml	
DD.HP.0.4	Volumetric pipette			0.4 ml	
DD.RT.0.4			2.2 mg/ml		
DD.0.2.S	Syringe (S)	Room Temperature (RT)		0.2 ml	
DD.10drp.S				10 drp	
DD.1drp.2.2		Oven, 100 °C		1 drp	
DD.2drp.1	Pasteur pipette	HP	1 mg/ml	2 drp	
DD.1drp.1.Au				1 drp	
			Dipping		
Sample	**Solution concentration**		**Solvent evaporation**		
DIP	2.2 mg/ml		RT		

3.3.7.2.   UHV-STM samples preparation

The 7x7 mm square shaped substrates were placed on a STM sample holder made of tantalum. A Chromel/ Alumel thermocouple was attached and fixed by welding of a clean tantalum foil, aiming to control the temperature of the sample while annealing at the UHV-STM chamber (figure 14). A commercial welding machine from Sunstone was used for that purpose.
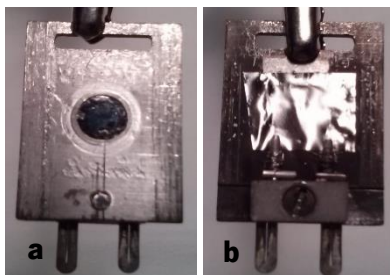
Figure 14: HOPG sample for UHV-STM: **(a)** front side; **(b)** back side

Samples were first introduced into the load lock chamber of the UHV-STM chamber and pumped out. They were then transferred to the UHV-STM chamber at 10^8 mbar pressure and annealed at 200 °C for 5 minutes.

This type of samples could also be used for air-STM scanning but there is no need for attachment of the thermocouple.

3.3.8. Zeta Potential

Electrical charge on colloidal particles surface attract oppositely charged ions to their surfaces. Commonly, two regions of charge are defined, the electrical double layer. The first one is an immobile layer of ions which adhere to the colloidal particle surface and the second one is a mobile layer of ions with opposite charge to those ions of the immobile layer. The radius of a sphere including the first layer is called the radius of shear and the electric potential at this point is called zeta potential. [106]

The zeta potential of all graphene samples were measured to quantify its electric potential, in order to choose a suitable natural polymer as a polyelectrolyte, with opposite electric potential to those values measured for each graphene sample, thus enabling the multilayer films materials selection.

Those measurements were accomplished into a Nano-Zs equipment from Malvern Instruments, and the results are presented as an average of 3 measurements for each solution.

3.4. Multilayer Films Production

The LbL technique presents several advantages, once the properties and composition of the produced films may be easily tailored. In fact, a huge variety of polymers may be dispersed in solution and it may also develop different morphologies and other properties according to the used

blend. The multilayer film thickness can be controlled by the number of deposited bilayers and it is possible to use low solution concentrations, which can turn it in an inexpensive technology [69], [107]. The LbL deposition is an attractive approach for this work since polyelectrolytes can be deposited in irregular surfaces, as prostheses.

An important process parameter is the pH; a higher pH value increases the charge density of the solution, which improves the film stability. The film wettability and, consequently, the biocompatibility, may be tailored by using different external layer materials. [69]

The ionic strength has also an important effect on the LbL assemblies. It can be enhanced by adding salt, commonly NaCl, resulting in thicker and more stable multilayer films. [69]

The LbL technique results in amorphous-like films, as the polyelectrolytes adsorption tends to irregularly interpenetrate between layers, and very stable films, as possible defects formed in a specific layer do not spread through the next layers and as the numerous charge interactions are neutralized. [107]

The multilayer films were produced and real time monitored in a Quartz Crystal Microbalance (QCM). The QCM presents an accurate mass sensing to monitor the LbL film formation in real-time. This microbalance is equipped with a piezoelectric quartz crystal covered in both upper and lower extremities by metal electrodes. When an alternating electric field across the quartz crystal is applied, it oscillates with a characteristic frequency, f. If a mass is adsorbed to the quartz crystal surface, it oscillates with a lower f, being possible to determine the amount of adsorbed mass. A simplistic approach to calculate the adsorbed mass uses the Sauerbray equation, valid for elastic experiments when the adsorbed mass does not exceed 2% of the crystal mass, given by equation (4). [108]

$$\Delta f = -2.\,\Delta m.\,f^2/A\big(\mu \rho_q\big)^{0.5} \tag{4}$$

being Δf the measured resonant frequency decrease (Hz), f the intrinsic crystal frequency, Δm the elastic mass change (g), A the electrode area, ρ_q the density of quartz (2.65 g/cm^3), and μ the shear modulus of quartz (2.95 x 10^{11} dyn/cm^2). [108]

However, the majority of the QCM studies does not follow an elastic, but inelastic behavior, where energy dissipation has to be considered for correct and reliable calculations of the adsorbed mass. The QCM-D can also measure energy dissipation properties, an important feature when assembling viscoelastic materials, as the case of polymers. [108]

Accordingly to the Zeta Potential of the graphene based solutions produced, suitable natural polymers PE were chosen, with opposite ZP of that measured in the graphene based solutions.

Several combinations of polyelectrolytes based on natural polymers and graphene were tried to produce multilayer films.

An attempt to produce a multilayer film of alternate layers of f-GFs dissolved in ethanolic solution (which revealed to be a PC in the ZP measurement) and Sodium Alginate, ALG, (natural polymer PA) was made. Both solutions had a concentration of 0.5 mg/ml. ALG was dissolved in DW for 20 hours by magnetic stirring and its pH was adjusted to 5.5 prior to use. Between the adsorption of each PE a washing step was included, right after the deposition of ALG, DW was feed to the QCM for 2.5 minutes followed by 2.5 minutes of ethanol, while after the deposition of f-GFs ethanolic solution, ethanol for 2.5 minutes followed by DW for 2.5 minutes were feed to the QCM. f-GFs and ALG were feed for 30 minutes each.

As the experiment described above used 2 solvents and the QCM-D only allows to use one solvent baseline, a second setup was run parallel to this experiment in a second QCM-D chamber. Simultaneously, while f-GFs ethanolic solution and ethanol as washing solvent was feed in the first QCM-D chamber, ethanol was feed in the second QCM-D chamber and, while ALG (in aqueous solution) and DW as washing solvent was feed in the first QCM-D chamber, DW was feed to the second QCM-D chamber.

A second attempt using f-GFs and ALG was made but the first two bilayers were produced with CHT and ALG, to serve as a support for f-GFs deposition. Each PE was feed for 10 minutes, intercalated by 5 minutes of washing with DW. CHT was dissolved in DW and 1% (v/v) acetic acid in a concentration of 0.5 mg/ml, for 20 hours. f-GFs and ALG were then deposited for 20 minutes each, intercalated by the same washing procedure as described for the experiment above.

The same build-up was also tried in an offline approach, i.e. PE deposition and washing were accomplished on the quartz crystal sensors out of the QCM-D and then loaded in the QCM-D chambers afterwards. 100 µl of PE solution or washing solvent were deposited on the quartz crystal sensor using a volumetric pipette and left there for 10 (natural polymers) and 20 minutes (f-GFs) or 5 minutes, respectively. Solutions were then carefully removed, using the volumetric pipette, and the quartz crystal sensors were loaded into the chambers, only after each washing step, since that is the moment that indicates the sensor frequency for the final mass bonded to the crystal, for each PE. Washing of f-GFs was done either by 5 minutes of ethanol or 5 minutes of DW and later

on, evaporation of the ethanol of the f-GFs solution was tried with a dryer, after removing a small amount of solution, instead of removing as much as possible of the extra solution with a volumetric pipette.

An ethanolic solution of f-GNRs in a concentration of 0.5 mg/ml was evaporated and DW was added to fulfil 50% ethanol and 50% DW, labeled as f-GNRs-50. This solution was alternatively feed to the QCM with an ELP (elastin-like polymer) solution dissolved in 50% ethanol and 50% DW, in a concentration of 0.5 mg/ml and pH 5.5. ELP solution was deposited for 10 minutes with a 50 μl/min flow, while f-GNRs ethanolic-aqueous solution was deposited for 20 minutes with a 25 μl/min flow, intercalated by 5 minutes washing using a 50% ethanol and 50% DW solvents mixture. ELP solution and washing solvent were corrected to a pH 5.5. The same build-up was tried with an f-GFs ethanolic-aqueous solution, containing 50% ethanol and 50% DW.

An f-GNRs solution in a concentration of 0.25 mg/ml was prepared in 25% ethanol and 75% DW. ALG was added to this solution to fulfill a 0.5 mg/ml concentrated f-GNRs-ALG solution in 25% ethanol and 75% DW, labeled as f-GNRs-ALG. CHT was dissolved in a concentration of 0.5 mg/ml in 25% ethanol and 75% DW, as well, and 1% (v/v) acetic acid. The washing solvent was 25% ethanol and 75% DW. The polycation CHT and washing solvent were corrected to the same pH as f-GNRs-ALG solution, pH 5.5. Four bilayers of CHT and f-GNRs-ALG and a top layer of CHT were assembled, accomplished by deposition of the polyelectrolytes for 10 minutes, intercalated by 5 minutes washing. Two multilayer films were produced following this procedure and labeled as (CHT/f-GNRs-ALG)4.5.

A similar procedure was applied to a f-GFs solution, to obtain a solution of f-GFs and ALG with a final concentration of 0.5 mg/ml in 25% ethanol and 75% DW, named f-GFs-ALG. This solution revealed a pH 7.4 and it was corrected to pH 5.5, a pH value commonly used in CHT containing multilayer films [66], [109]. CHT and washing solutions were prepared following exactly the same procedure as described above, but corrected to a pH 5.5. Two multilayer films were produced containing 4 bilayers of CHT and f-GFs-ALG and a top layer of CHT, named (CHT/f-GFs-ALG)4.5.

Multilayer films of alternate layers of CHT and ALG were produced as control films for (CHT/f-GNRs-ALG)4.5 and (CHT/f-GFs-ALG)4.5 multilayer films. CHT and ALG solutions were produced in a concentration of 0.5 mg/ml in a mixture of 25% ethanol and 75% DW and 1% (v/v) acetic acid was added to the CHT solution. Both polyelectrolytes and washing solution (mixture of 25% ethanol

and 75% DW) were corrected to a pH 5.5. Two control films were assembled by four bilayers of CHT and ALG and a top layer of CHT, denominated (CHT/ALG)4.5.

Aqueous solutions of o-GNRs and o-GFs were combined with polycations natural polymers, Met. CHT and CHT. Met. CHT was dissolved in DW by magnetic stirring for several hours and corrected to a pH 7.0. CHT was dissolved in DW and 1% (v/v) acetic acid by magnetic stirring for several hours and corrected to a pH 5.5. Each polyelectrolyte was deposited for 10 minutes, followed by washing with DW for 5 minutes. The follow multilayer films were accomplished: (Met. CHT/o-GNRs)3, (Met. CHT/o-GFs)2, (CHT/o-GNRs)4, (CHT/o-GNRs)5 and (CHT/o-GFs)3. The numbers indicate the number of bilayers. o-GNRs and o-GFs aqueous solutions were prepared in 2 different concentration, 0.25 and 0.5 mg/ml, to produce the multilayer films (CHT/o-GNRs)5, (CHT/o-GFs)3 and (Met. CHT/o-GNRs)3, (Met. CHT/o-GFs)2, (CHT/o-GNRs)4, respectively.

Those multilayer films used fresh natural polymer solutions and pH values were corrected using 0.5 M HCl and 0.5 M NaOH or 2 M NaOH (for CHT solutions).

All online QCM-D experiments were performed at 25 °C with a 50 µl/min flow in a QCM-D E4 from Q-Sense Instruments. All successfully assembled multilayer films are summarized in table 2.

Table 2: Summary of the build-up parameters of the successfully assembled multilayer films

Multilayer film	PC (pH)	PA (pH)	Bilayers	C (mg/ml)
(CHT/f-GNRs-ALG)4.5		f-GNRs-ALG (5.5)		
(CHT/f-GFs-ALG)4.5	CHT (5.5)	f-GFs-ALG (5.5)	4.5	
(CHT/ALG)4.5		ALG (5.5)		0.5
(Met. CHT/o-GNRs)3	Met. CHT (7.0)	o-GNRs	3	
(Met. CHT/o-GFs)2		o-GFs	2	
(CHT/o-GNRs)4			4	
(CHT/o-GNRs)5	CHT (5.5)	o-GNRs	5	0.5 (PC), 0.25 (PA)
(CHT/o-GFs)3		o-GFs	3	

3.5. Modelling of the QCM-D data of the multilayer films

The QCM-D response of the prepared multilayer films was modelled using a software from Q-sense, QTools, which allows to estimate the viscosity, shear modulus and thickness variations as a function of the layer number.

The resonant frequency, Δf, and dissipation, ΔD, variations recorded in the QCM-D can be modeled in the QTools software using a Voigt based model, equivalent to a spring and a dashpot in parallel under no slip conditions, suitable for viscoelastic films. These variations are presented in equations (5) and (6). [66], [109]

$$\Delta f \approx -\frac{1}{2\pi\rho_0 h_0}\left\{\frac{\eta_S}{\delta_S} + h_L\rho_L\omega - 2h_L\left(\frac{\eta_S}{\delta_S}\right)^2\frac{\eta_L\omega^2}{\mu_L^2+\omega^2\eta_L^2}\right\} \tag{5}$$

$$\Delta D \approx -\frac{1}{\pi f\rho_0 h_0}\left\{\frac{\eta_S}{\delta_S} + 2h_L\left(\frac{\eta_S}{\delta_S}\right)^2\frac{\eta_L\omega}{\mu_L^2+\omega^2\eta_L^2}\right\} \tag{6}$$

being ω the angular frequency of the oscillation, ρ_0 and h_0 the density and thickness of the crystal, respectively, η_s the solution viscosity, δ_s the viscous penetration depth of the shear wave in the solution, given by $2(\eta_s/\rho_s\omega)^{1/2}$, ρ_s the solution density, and h_L, η_L, μ_L and ρ_L the thickness, viscosity, elastic shear modulus and density of the adsorbed layer, respectively. [66], [109]

By providing ρ_s, η_s and ρ_L to the QTools software, it compares Δf and ΔD values obtained in the in-situ QCM-D experiment and modelled values and gives the sum of the squares of the scaled errors between the experimental and modelled values (Total ChiSqr). ρ_s, η_s and ρ_L may be changed to get the lower Total ChiSqr possible. These algorithm uses, at least, 3 overtones of frequency and dissipation. [109]

Chapter 4

Results and Discussion

This chapter proves the success of graphene and multilayer films production and presents the results obtained by the characterization techniques described in Chapter 3, followed by a discussion and conclusions taken out of those results.

4.1. Graphene Characterization

4.1.1. Ultraviolet-Visible Spectroscopy

The absorptivity coefficient of f-GFs, o-GNRs and o-GFs were calculated from the UV-Vis absorption spectra, as explained in section 3.4.1, in order to quantify the concentration of those graphene solutions produced. The absorptivity coefficient of f-GNRs was calculated in a previous work. UV-Vis spectra and A/l vs. C curves are plotted below for f-GFs, o-GNRs and o-GFs samples, in figures 15 to 17. The UV-Vis spectra of the solvents, DW and Ethanol is also plotted.
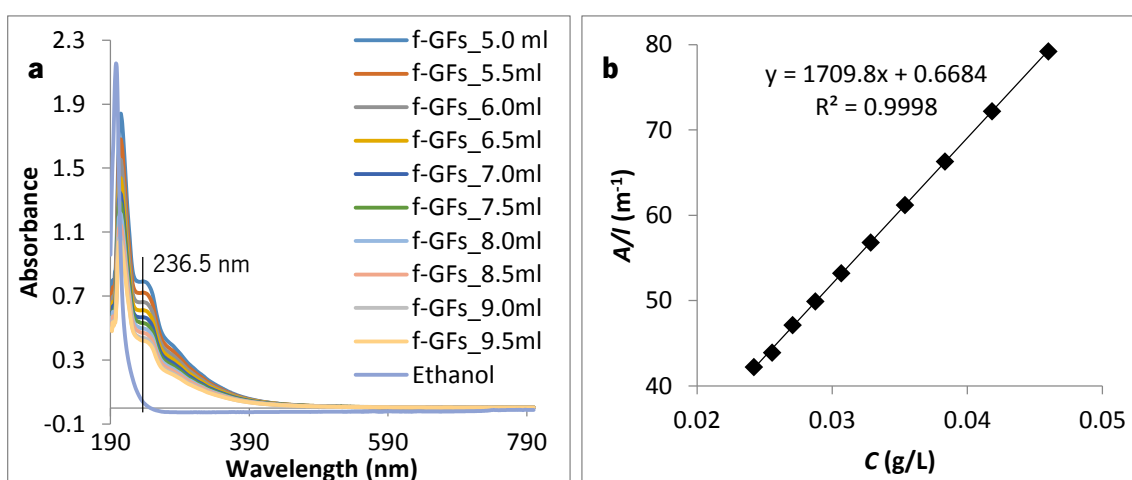
Figure 15: (a) UV-Vis spectrum of f-GFs at different solution concentrations; **(b)** A/l vs. C graph for absorptivity coefficient calculation of f-GFs through the graph slope
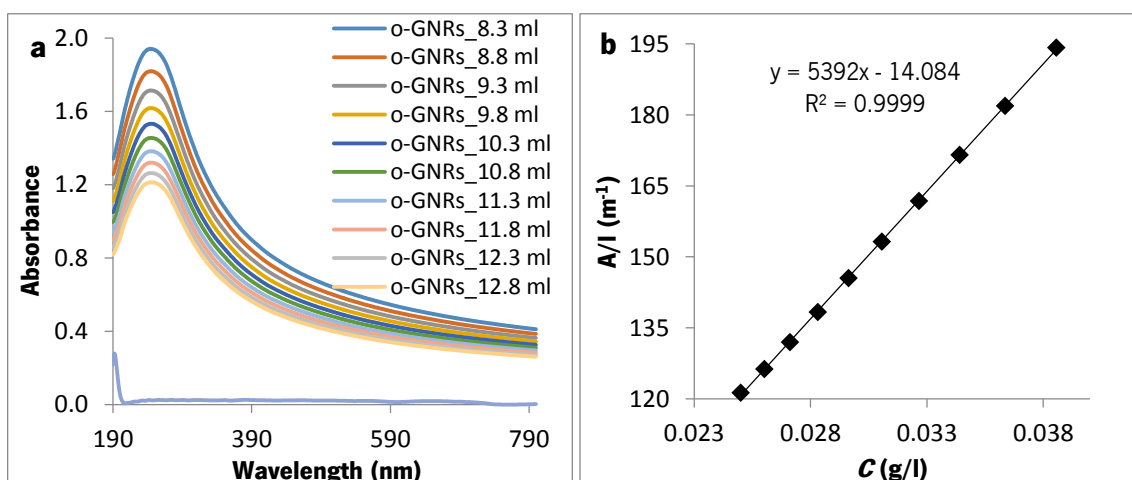
Figure 16: (a) UV-Vis spectrum of o-GNRs at different solution concentrations; **(b)** A/l vs. C graph for absorptivity coefficient calculation of o-GNRs through the graph slope
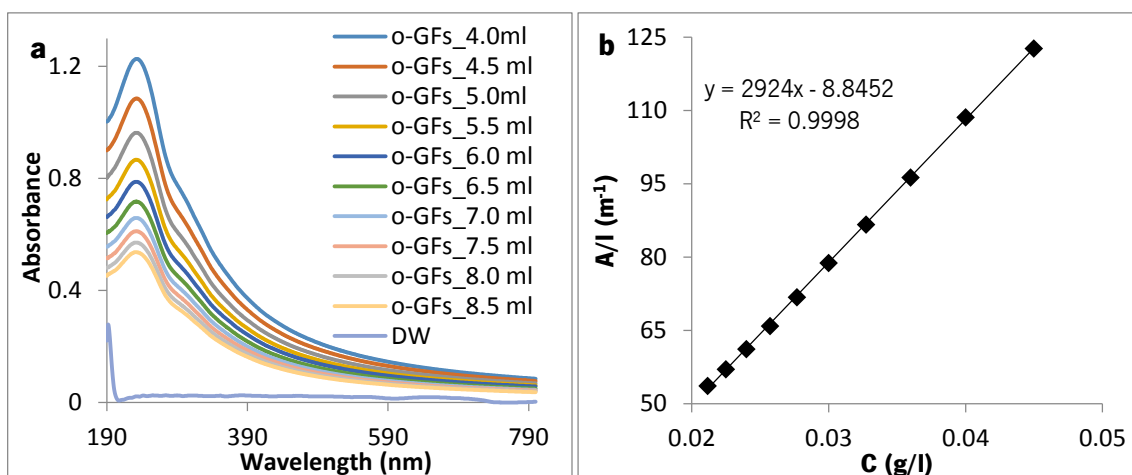
Figure 17: (a) UV-Vis spectrum of o-GFs at different solution concentrations; **(b)** A/l vs. C graph for absorptivity coefficient calculation of o-GFs through the graph slop

The absorptivity coefficient, given by the slope of A/l vs. C curves, and wavelength at maximum absorbance of all graphene types produced in this work are summarized in table 3. The absorptivity coefficient of f-GNRs and f-GFs was calculated using the absorbance values at the shoulder close to the main peak (250.0 nm and 236.5 nm for f-GNRs and f-GFs, respectively) because the maximum absorbance of ethanol is also observable at this wavelength (~200 nm).

Table 3: Absorptivity coefficient and wavelength for maximum absorbance of graphene samples

Sample	Wavelength at maximum absorbance (nm)	ε (L/g.m)
f-GNRs	250.0 ± 0.7	1620 ± 200
f-GFs	236.5 ± 0.6	1710 ± 172
o-GNRs	244.3 ± 0.7	5392 ± 81
o-GFs	232.3 ± 0.6	2924 ± 23

Similar absorptivity coefficients, with the same order of magnitude as those presented in table 3 were also presented in the literature for graphene solutions [97], [110], [111]. Values of 2460 and 3620 L/g.m were reported for GFs produced through exfoliation of graphite in the solvent N-methyl-pyrrolidone (NMP), under mild sonication [110], [111]. Oxidized graphene nanosheets, produced through oxidation of graphite, using sulfuric acid, nitric acid and potassium chlorate, were reported to have an absorptivity coefficient of 5300 L/g.m [97].

As reported in the literature, o-GFs present a wavelength of approximately 230 nm at maximum absorbance, followed by a shoulder at around 300 nm. The peak at 230 nm is attributed to π-π* transitions of C-C bonds in the aromatic regions and the shoulder at 300 nm to n- π* transitions of C=O bonds between graphene and functional groups [52], [112]–[115].

A wavelength of 234 nm at maximum absorbance was reported for o-GNRs by Kosynkin and coworkers. [53]

Similarly to o-GFs, f-GNRs (as can be seen in figure 18) and f-GFs also present an absorbance shoulder close to the maximum absorbance peak, between 230 and 260 nm. However, the maximum absorbance peak is greatly influenced by the solvent (ethanol).
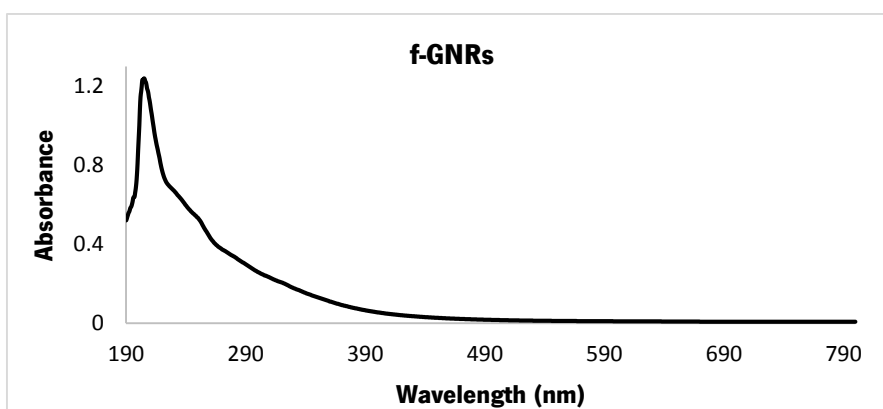
Figure 18: Example of f-GNRs UV-Vis spectra

Every single graphene solutions produced were analyzed by UV-Vis spectroscopy after centrifugation in order to confirm graphene formation and quantify its mass and concentration using the Beer-Lambert law.

Fifty solutions containing approximately 120 mg of f-MWNTs in 40 ml ethanol were produced to obtain an average concentration of 0.031 ± 0.002 mg/ml of f-GNRs solution, resulting in a yield process of 1.0%.

Average f-GFs solutions concentrations are presented in table 4, for different initial f-EG mass (in 40 ml ethanol) and sonication time. Those average concentration values are out of 3 samples, for each condition.

Table 4: f-GFs solutions concentration as a function of time and f-EG initial mass

f-EG mass (mg)	Sonication time (min)	C f-GFs (mg/ml)
40		0.016 ± 0.002
80	10	0.030 ± 0.003
120		0.041 ± 0.003
	15	0.043 ± 0.002
160	10	0.051 ± 0.002
	15	0.052 ± 0.002

As observable in table 4, the initial f-EG mass has a great influence in the final f-GFs concentration but that is not as evident with extra 5 minutes of sonication and as high sonication time may break graphene, the solutions were produced using 160 mg of f-EG, sonicated for 10 minutes. Ten more f-GFs batches were produced, completing a total of 28 f-GFs solutions.

Comparing the initial concentration of f-EG and the final concentration of f-GFs, the higher the initial f-EG content, the lower is the yield of f-GFs production. The highest yield of 1.6% was obtained for an initial f-EG mass of 40 mg and the lowest yield of 1.3% for an initial f-EG mass of 160 mg. Nevertheless, it is higher than the yield process of f-GNRs (1.0%). The lower the initial mass of f-MWNTs or f-EG, the higher the effect of ultrasounds in the solution, and the higher the yield process of f-GNRs or f-GFs production.

The as-obtained o-GNRs and o-GFs solutions were diluted for UV-Vis spectroscopy analysis in order to quantify their initial concentration. 1 ml of the o-GNRs and o-GFs solutions, were diluted in 25 and 5 ml of DW, and the initial concentrations were measured, yielding 0.906 and 0.319 mg/ml, respectively. A yield of 50.6% and 6.2% was calculated for o-GNRs and o-GFs, respectively. Such difference may be explained by the considerably different initial o-MWNTs and o-EG concentration and sonication time.

4.1.2. Infrared Spectroscopy

The covalent bonded species to all graphene samples were studied by FTIR. The results are presented below, in figures 19 (f-GNRs and f-GFs) and 20 (o-GNRs and o-GFs). FTIR spectra of

graphene flaks are presented by grey lines, corresponding to the right y-axis at grey, while FTIR spectra of graphene nanoribbons are presented by black lines, corresponding to the left y-axis at black.
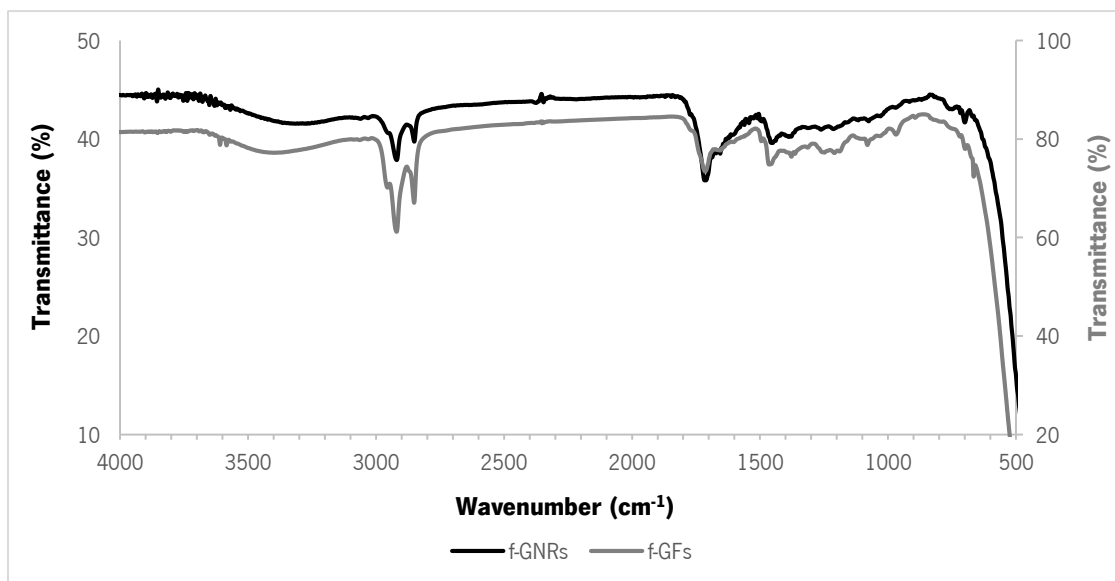
Figure 19: FTIR spectra of f-GNRs and f-GFs

As expected, similar spectra is observable for f-GNRs and f-GFs, once they were functionalized following the same procedure.

A large band is observable around 3400 cm^{-1}, probably due to O-H stretching and/or N-H stretching [116] found in pyrrolidine.

Two peaks close to each other are observable at approximately 2850 and 2920 cm^{-1}, likely due to the presence of aliphatic C-H [116].

A peak is observable at 1715 cm^{-1}, which may be attributed to C=O stretching [116], in the protected amine.

N–H stretching [116] coming from the pyrrolidine group might be associated with the peak at 1460 cm^{-1}.

Many more peaks are seen for wavelengths smaller than 1400 cm^{-1} but with very low intensity, and thus less significant and more difficult to interpret.

Although different procedures have been applied on the oxidation of MWNTs and EG, the resultant o-GNRs and o-GFs present similar transmittance peaks in the FTIR analysis, as presented in figure 20.
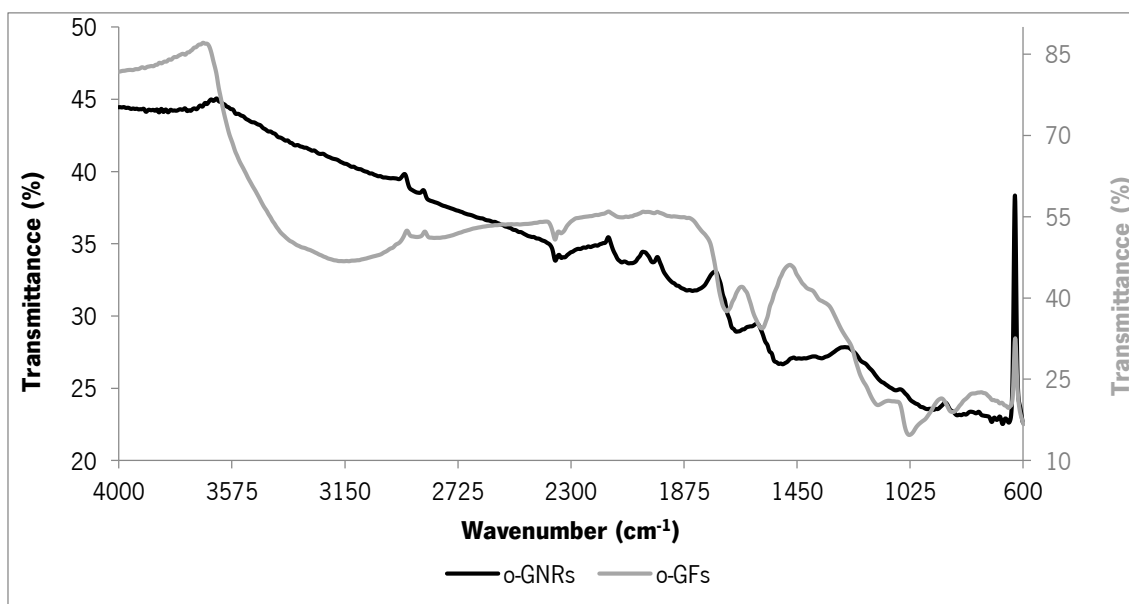
Figure 20: FTIR spectra of o-GFs and o-GNRs

Between approximately 3000 and 3600 cm^{-1}, a broad band is observable for o-GFs, which may correspond to hydroxyl groups (O-H) stretching from the carboxylic acid group, phenol, and/or intercalated water. [115]–[119].

Both o-GFs and o-GNRs present peaks at around 2100, 2320, 2360 and 2870 cm^{-1}. The peak at 2100 cm^{-1} may correspond to a combination of O-H stretching, while the peaks at 2320 and 2360 cm^{-1} are typical of CO_2 in the ambient air, and the peak at 2870 cm^{-1} might be due to C-H stretching [116].

A peak observable at around 1710 cm^{-1} for o-GFs, is observable at approximately 1660 cm^{-1} for o-GNRs, which might be attributed to carboxylic groups (C=O) stretching [115], [116], [118], [120].

The non-oxidized graphene domains (C=C stretching) are responsible for a peak at 1580 cm^{-1} [113], [116]–[118], [120].

Both o-GNRs and o-GFs present peaks at 1030 and 1150 cm^{-1} due to C-O stretching, [115], [116], [118], [120] of epoxy or alkoxy groups [119], though not as evident for o-GNRs as for o-GFs.

A peak at 870 cm^{-1}, for both o-GNRs and o-GFs, is observable and it is due to epoxy groups [119].

4.1.3. Thermogravimetric Analysis

The extent of the cycloaddition functionalization and oxidation of MWNTs and EG was evaluated by TGA. TGA curves of raw EG and MWNT (prior to functionalization/oxidation) and f-MWNTs, f-EG, o-MWNTs and o-EG (after functionalization/oxidation and prior to ultrasounds exposure), are presented below, in figures 21 to 24.

Figure 21 presents TGA curves of raw MWNTs and functionalized MWNTs (f-MWNTs).
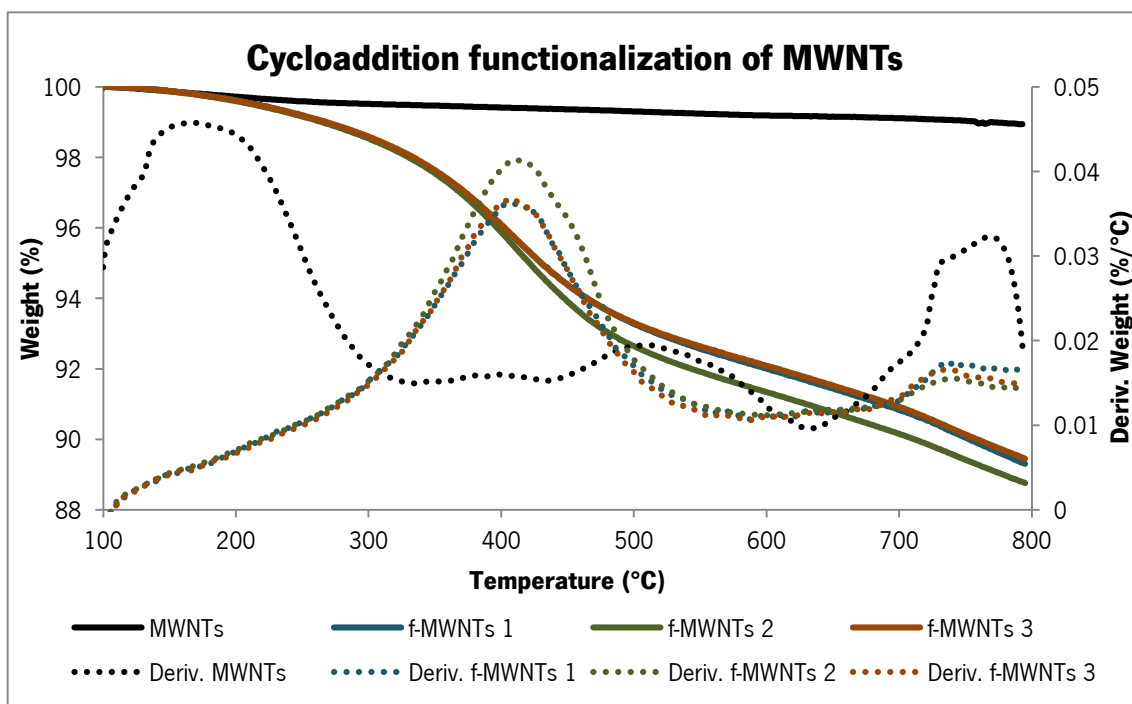
Figure 21: TGA curves of MWNTs prior (MWNTs) and after (f-MWNTs) functionalization

The weight loss of raw MWNTs was almost negligible, approximately 1%, while f-MWNTs presented an average weight loss of $10.8 \pm 0.3\%$. The higher rate of weight loss for f-MWNTs was verified at approximately 409 °C, corresponding to functional groups loss. Another peak is seen at around 770 °C, which might correspond to thermal degradation of impurities originated in the MWNTs production, since this peak is also notable in the derivative curve of the raw MWNTs.

Raw MWNTs present the higher rate of weight loss around 175 °C, which might correspond to adsorbed moisture loss, and two more peaks at around 520 and 770 °C.

Figure 22 presents TGA curves of raw EG and functionalized EG (f-EG).
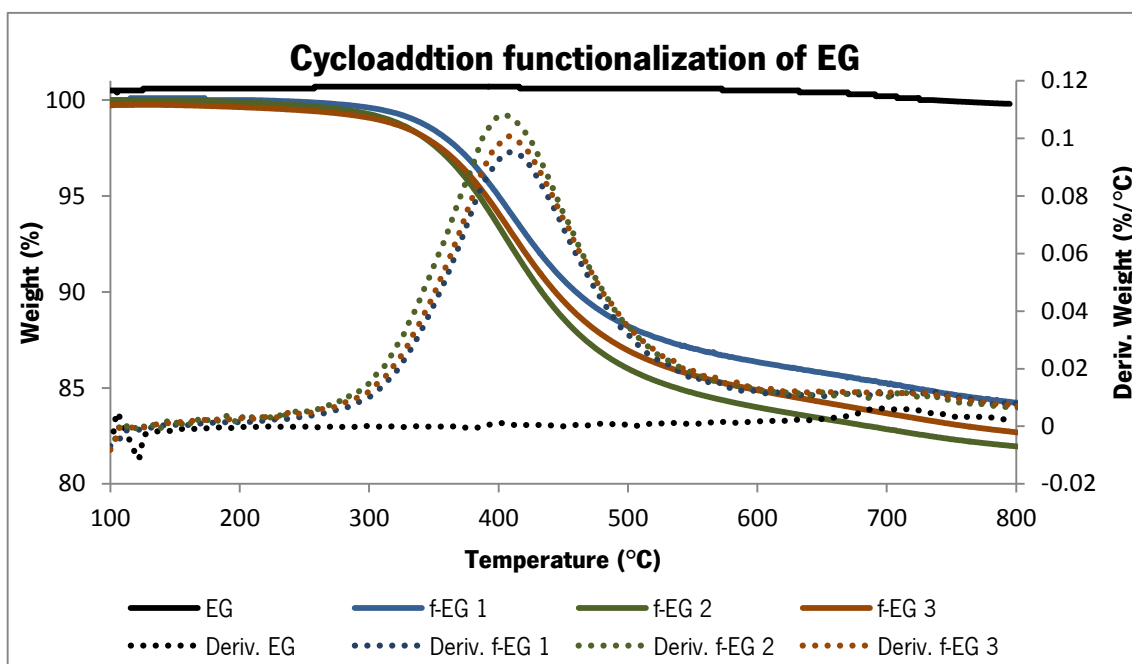
Figure 22: TGA curves of EG prior to (EG) and after (f-EG) functionalization

Raw EG presented a weight loss of circa 0.4% and f-EG presented an average weight loss of 17.3 ± 0.9%. Similarly to the TGA curves of f-MWNTs, TGA curves of f-EG present a maximum rate of weight loss at around 406 °C, which confirms this is the temperature corresponding to the functional groups loss.

A minute weight loss is observed, either in raw EG and f-EG curves, at approximately 710 °C, probably corresponding to impurities acquired in the exfoliation of natural graphite to produce EG. Another weight loss peak is also observable in the derivative curve of EG right above 100 °C, which may correspond to moisture removal.

TGA curves of oxidized MWNTs following the method proposed by Kosynkin and coworkers and is presented in figure 23. The raw MWNTs TGA curve is again plotted for comparison.
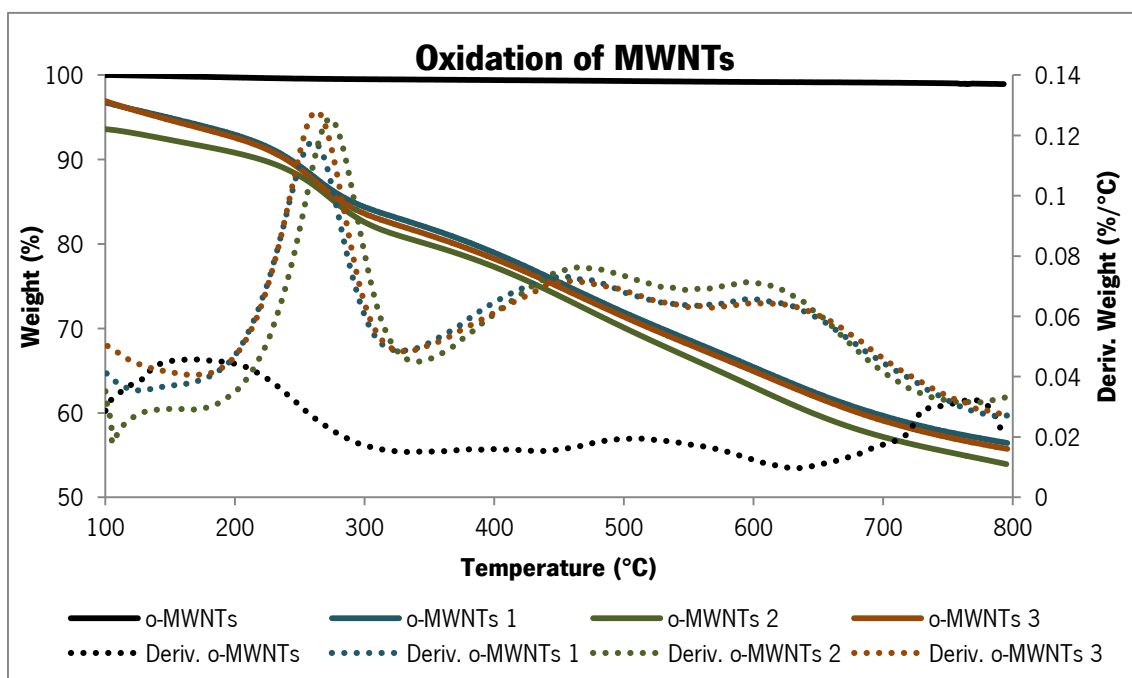
Figure 23: TGA curves of o-MWNTs according to the method described by Kosynkin and coworkers and raw MWNTs (already presented in figure 21)

o-MWNTs produced, following a method described by Kosynkin and coworkers, present three main thermal degradation stages, at approximately 270, 460 and 620 °C. The first weight loss peak might correspond to loss of unstable functional groups [52], the second peak to more strongly bonded functional groups and the last one could even be due to the loss of outermost layer of the o-MWNTs. These o-MWNTs presented an average weight loss of 42.5 ± 2%.

TGA curves of o-EG accomplished through a modified Hummers' method are presented in figure 24.
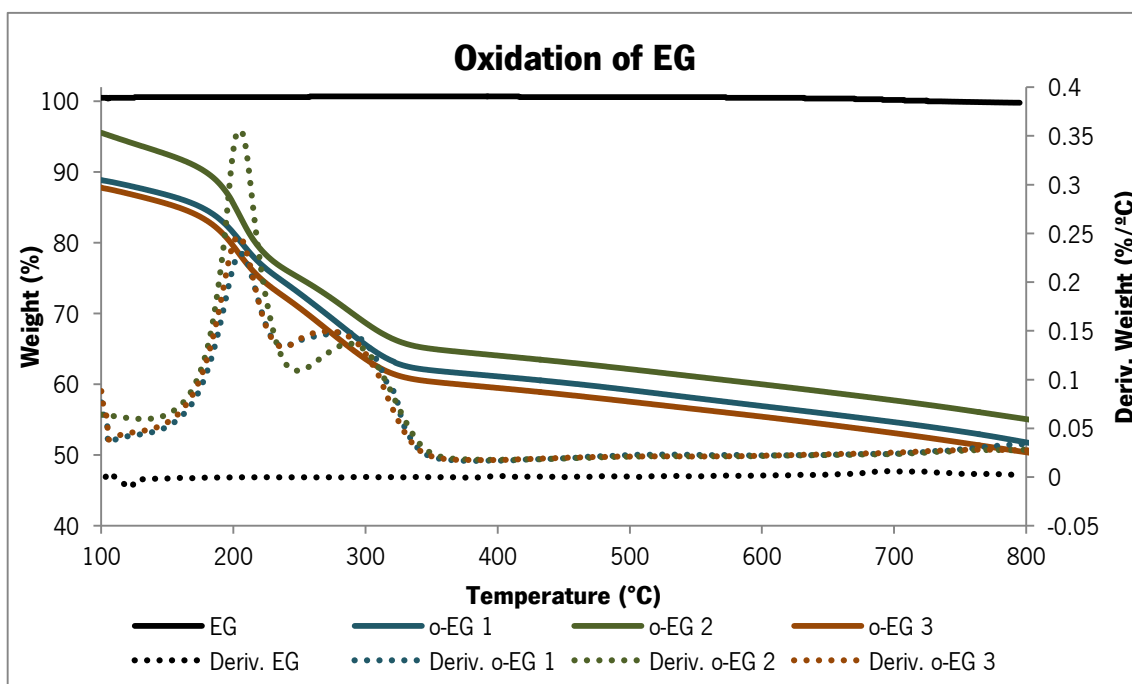
Figure 24: TGA curves of EG prior and after oxidation according to the modified Hummers' method

Oxidized EG, oxidized through the modified Hummers' method, presents two stages of thermal degradation according to TGA curves presented in figure 24. The first weight loss occurs at around 208 °C and the last one at around 290 °C, corresponding to an overall weight loss of 40.7 ± 2.9%.

By comparing the average weight loss of oxidized MWNTs (42.5 ± 2%) and EG (40.7 ± 2.9%) with functionalized MWNTs (10.8 ± 0.3%) and EG (17.3 ± 0.9%), it is expected that both oxidized GNRs and GFs present higher extent of functionalization than functionalized GNRs and GFs.

TGA curves of f-GNRs and f-GFs produced through sonication of f-MWNTs and f-EG, and further centrifugation, are presented in figures 25 and 26.
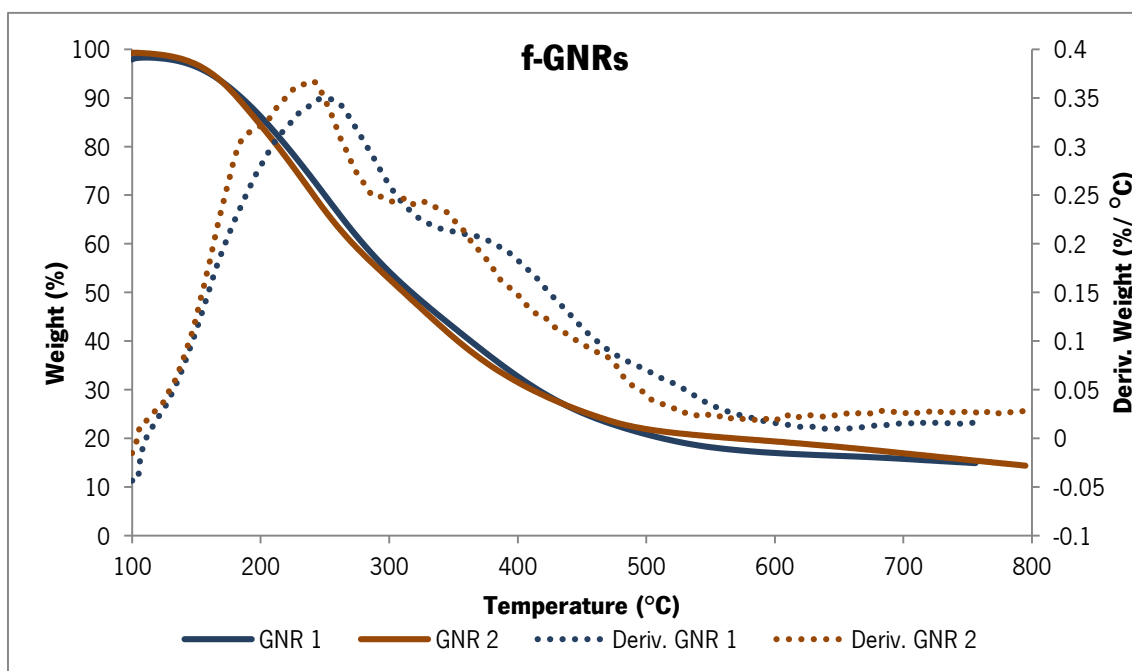
Figure 25: TGA curves of f-GNRs

f-GNRs present a peak of maximum rate of weight loss at 219 and 240 °C, average value 230 ± 11 °C, followed by a shoulder between approximately 290 and 420 °C, both features probably due to thermal degradation of the functional groups.
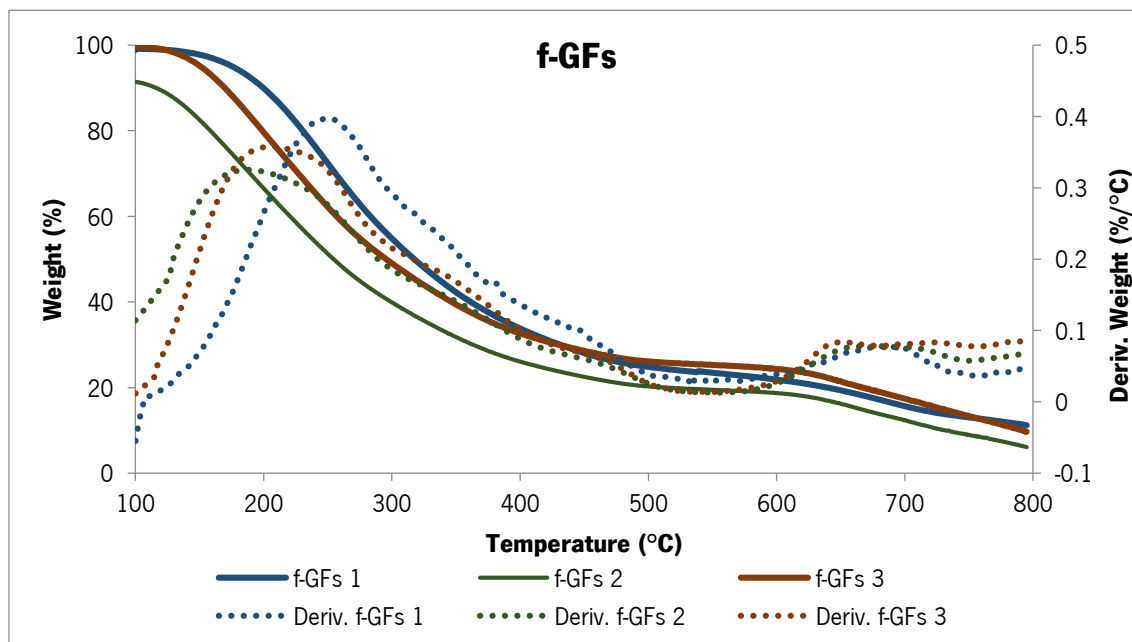
Figure 26: TGA curves of f-GFs

f-GFs present a peak of maximum rate of weight loss at quite distinct temperatures, 186, 206 and 251 °C, corresponding to an average value of 214 ± 27 °C, related to thermal degradation of the functional groups. Another weight loss peak, not so well defined, is visible around 670 °C, which might be caused by impurities present in the raw EG and f-EG, also observable in figure 22.

The overall weight loss was 83.9 ± 0.9% for f-GNRs and 87.7 ± 1.9% for f-GFs.

TGA curves of o-GNRs and o-GFs, produced through sonication of o-MWNTs produced according to the method presented by Kosynkin and coworkers and o-EG produced according to a modified Hummers' method, respectively, are presented in figures 27 and 28.
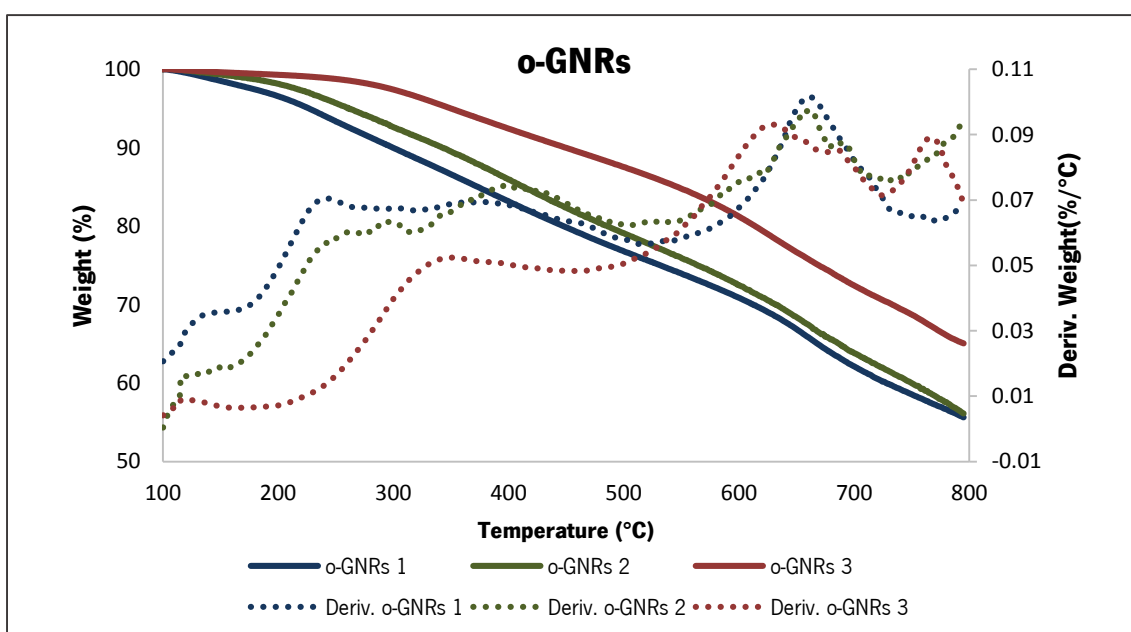
Figure 27: TGA curves of o-GNRs

o-GNRs present at least two stages of high weight loss rate, of what is likely to be due to thermal degradation of functional groups, one between 170 and 500 °C and another one centered at 628 °C for o-GNRs 3 and at approximately 660 °C for o-GNRs 1 and o-GNRs 2, resulting an average value of 649 ± 15 °C. Similar value was observable for o-MWNTs, which might indicate that this last peak could correspond to the loss of some of the o-GNRs. The overall weight loss was measured to be 41.1 ± 4.3%.
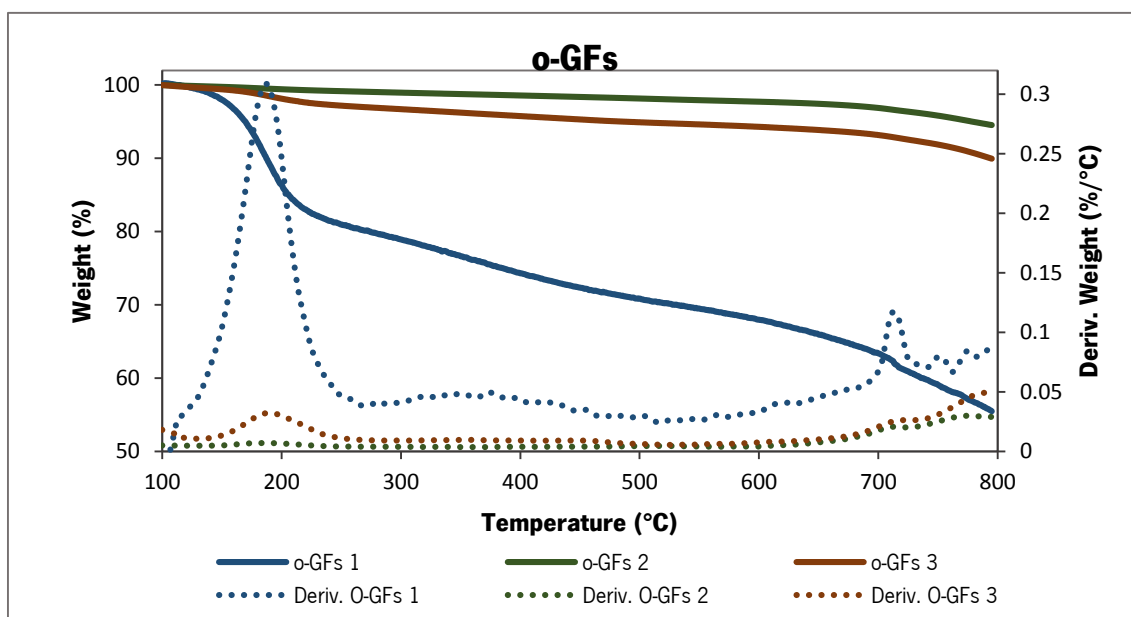
Figure 28: TGA curves of o-GFs

Concerning to o-GFs, two main peaks of weight loss are observable at 187 ± 2 °C and at 717 ± 5 °C, accounting for a total weight loss of $20.0 \pm 17.4\%$. Noticeable intensity variations are seen in these curves due to low initial mass used for these analysis. Even though, all of them consistently present high rate of weight loss at the same temperatures. The total weight loss is not a reliable value because the sample initial weight is low and the measurements are in the limit of detection of the balance. Similarly to what was verified before, the weight loss peaks at 717 ± 5 °C might correspond to impurities present in the raw EG and o-EG (hardly seen in figure 24).

With respect to thermal degradation resistance and resorting to the overall weight loss of the graphene types produced, it may be concluded that the oxidized graphene (both o-GNRs and o-GFs) present better thermal degradation resistance than functionalized graphene (both f-GNRs and f-GFs). As o-GNRs and o-GFs present similar percentage of weight loss to o-MWNTs and o-EG, mainly o-GNRs and o-MWNTs, it is likely that the weight loss corresponds mainly to the loss of oxygen containing functional groups and less to graphitic regions loss. In the other hand, the weight loss of f-GNRs and f-GFs is greatly superior to the weight loss of f-MWNTs and f-EG.

4.1.4. Scanning Transmission Electron Microscopy

STEM and EDS analyses were helpful to look for insights about graphene and impurities distribution, shapes and sizes of the graphene produced in solution, prior to AFM and STM observations.

STEM images of f-GNRs are presented below in figure 29.
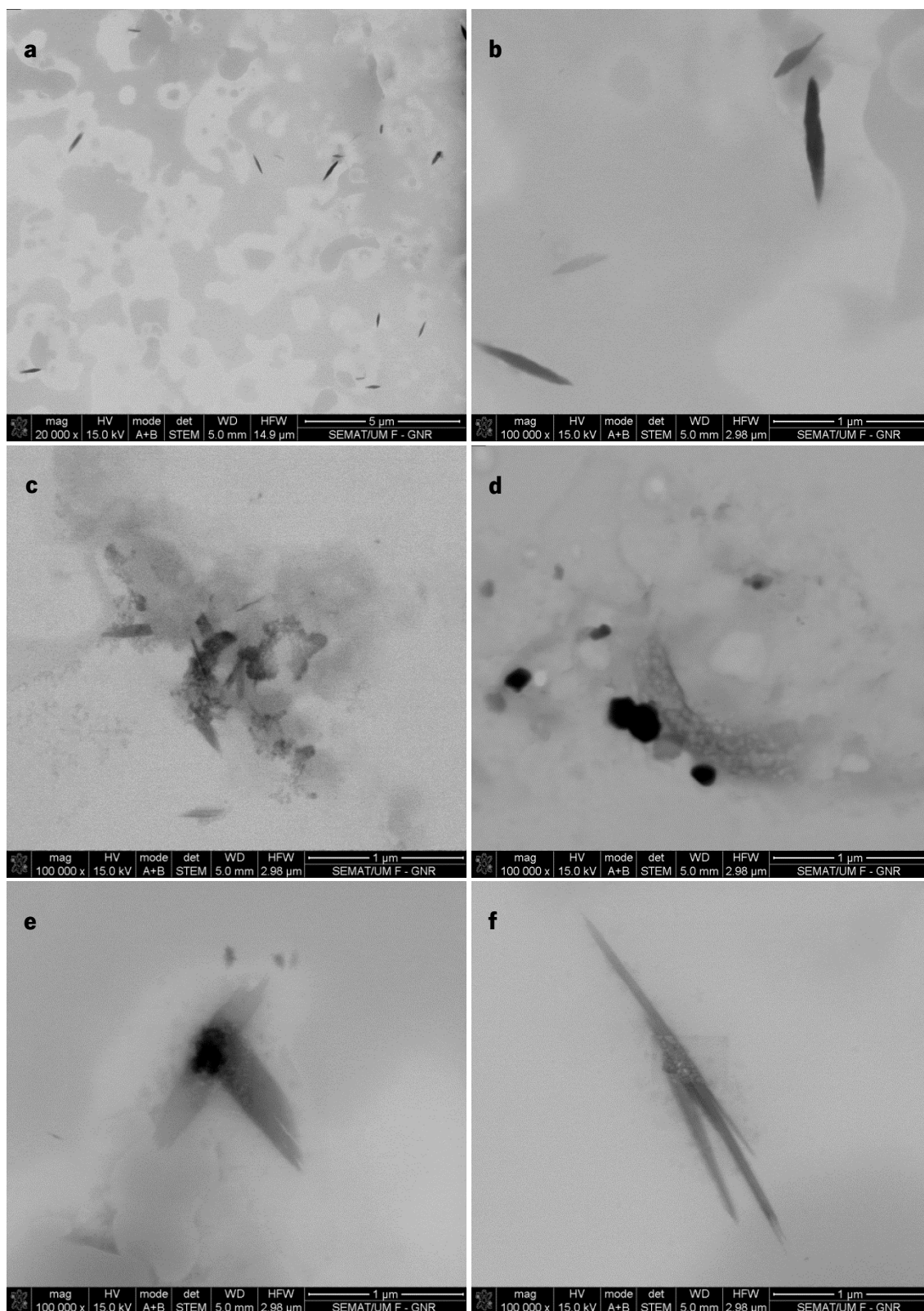
Figure 29: STEM images of f-GNRs: **(a – c)** dispersed clusters of f-GNRs; **(d)** Si impurities found in f-GNRs sample; **(e – f)** single clusters of f-GNRs. In f is possible to see that the electron beam was destroying the f-GNRs cluster

It is possible to observe that f-GNRs are quite flat and reasonably well dispersed, with similar elongated rectangular shapes among them. The images show that f-GNRs length roughly varies between 300 and 900 nm with widths varying between 70 and 300 nm, showing that they correspond to small aggregates of a few f-GNRs.

EDS analysis on the area of figure 29 (d) detected high amounts of silicon, Si, and oxygen, O. These might indicate presence of silicon dioxide (SiO_2) due to erosion of the glass flasks where these f-GNRs were subject to sonication. The EDS analysis is presented in figure 30.
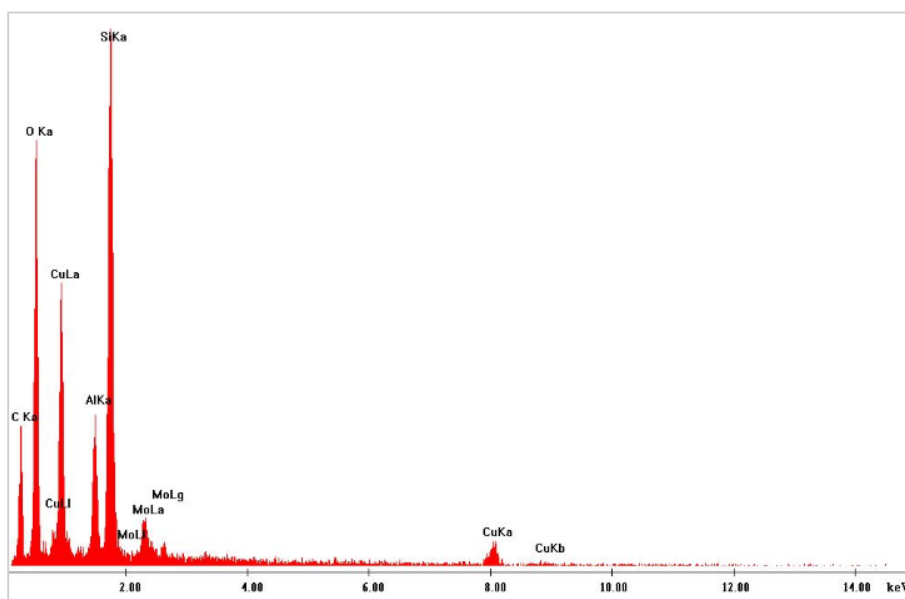
Figure 30: EDS analysis of f-GNRs in the area of figure 29 (d), where is possible to see some impurities

Carbon, C, from graphene, and nitrogen, N, (not signaled but it is presented close to the carbon peak), from the functional groups, were also detected. The other peaks correspond to the chemical elements present in the sample holder.

STEM images of f-GFs are presented in figure 31.
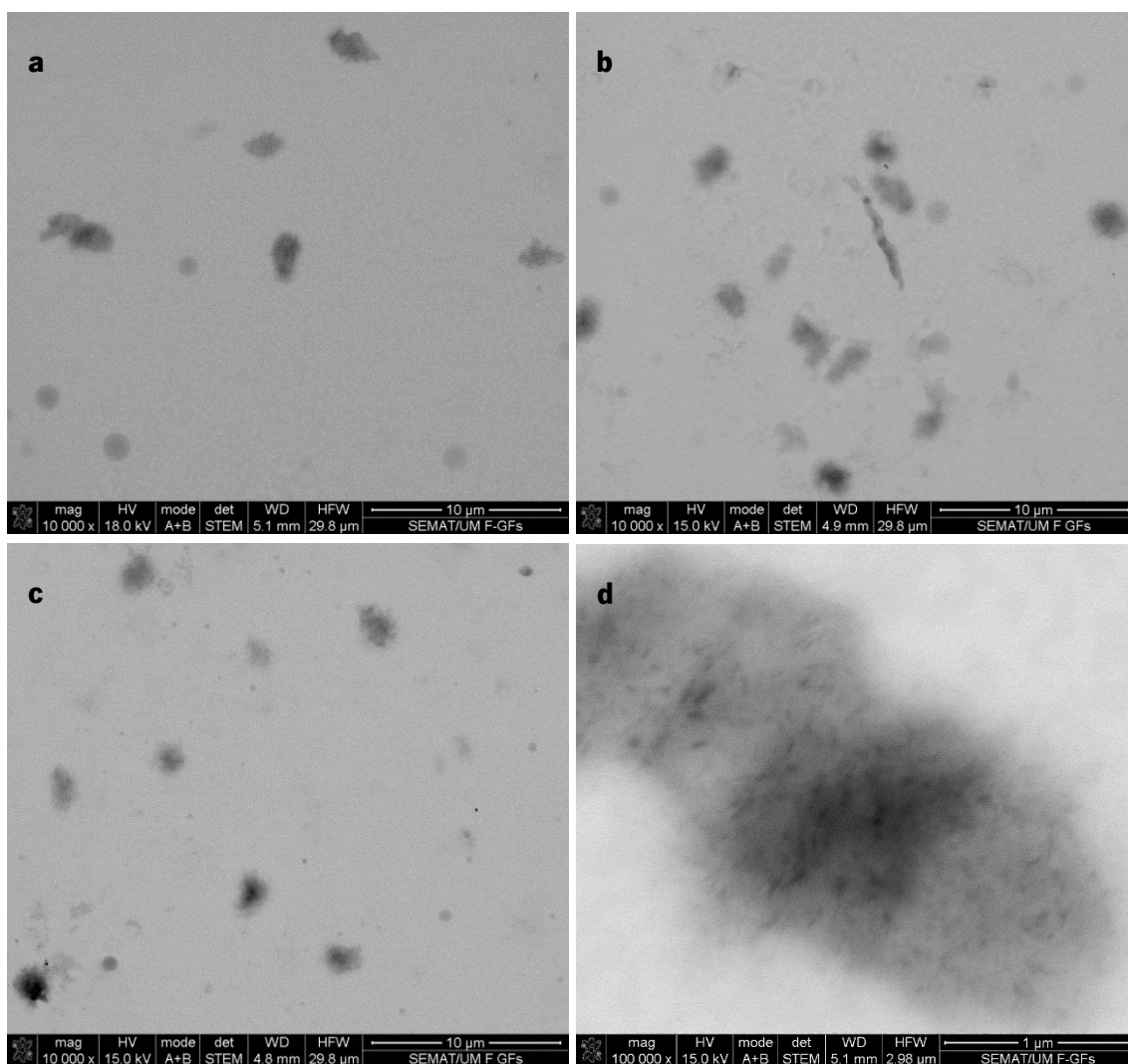
Figure 31: (a - c) STEM images of dispersed f-GFs and **(d)** single f-GF domain

Aiming to evaluate the area and diameter of f-GFs domains, figure 31 (a – c) were analyzed by the *ImageJ* software. The average area was found to be 2.4 ± 1.2 μm^2 and the equivalent diameter 2.5 ± 0.9 μm.

Figure 31 (d) is a magnifications of an f-GFs domain. Some dark points are seen, which might indicate presence of impurities. An EDS analysis (figure 32) on the area of figure 31 (d) revealed presence of C, N, O, sodium (Na), chlorine (Cl), potassium (K), and calcium (Ca), which might correspond to intercalated compounds in the raw EG or some degree of contamination during the chemical treatments. O and N might belong to the functional groups.
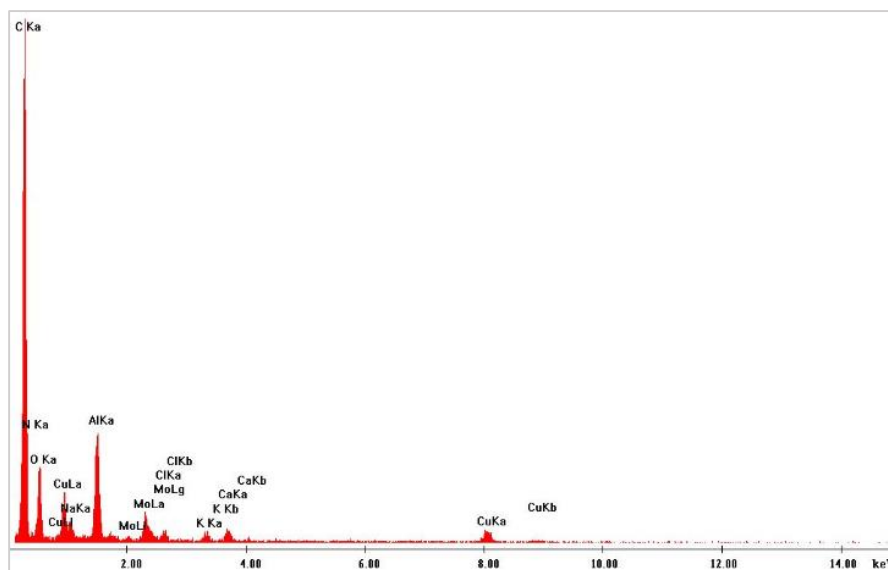
Figure 32: EDS analysis of f-GFs in the area of figure 31 (d)

Those elements not mentioned before presented in this EDS analysis are detected from the support and TEM grid.

STEM images and of o-GNRs are presented in figure 33.
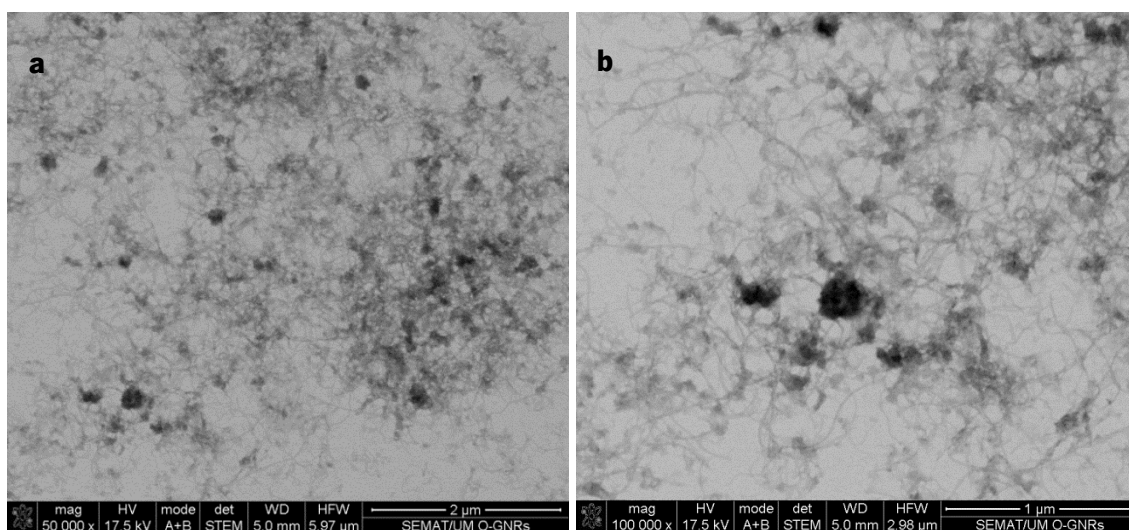
Figure 33: STEM images of o-GNRs

It is observed that o-GNRs are presented in a kind of network and those o-GNRs are quite narrow when compared to f-GNRs. This arrangement of o-GNRs might be an advantage to produce multilayer films, even though the concentration of the solution used for STEM observation is much higher than the 0.5 mg/ml o-GNRs concentrated solution used for LbL deposition. The high concentration of o-GNRs seen in these images also demonstrate the high yield of this method to produce GNRs.

Figure 34 shows the huge o-GFs that can be obtained by the oxidation of EG using a modified Hummers' method. Similarly to f-GFs, o-GFs can easily reach widths of approximately 2 µm. Some wrinkles are visible and impurities similar to those observable in figure 29 (d) are also observable in figure 34 (a) and (b).
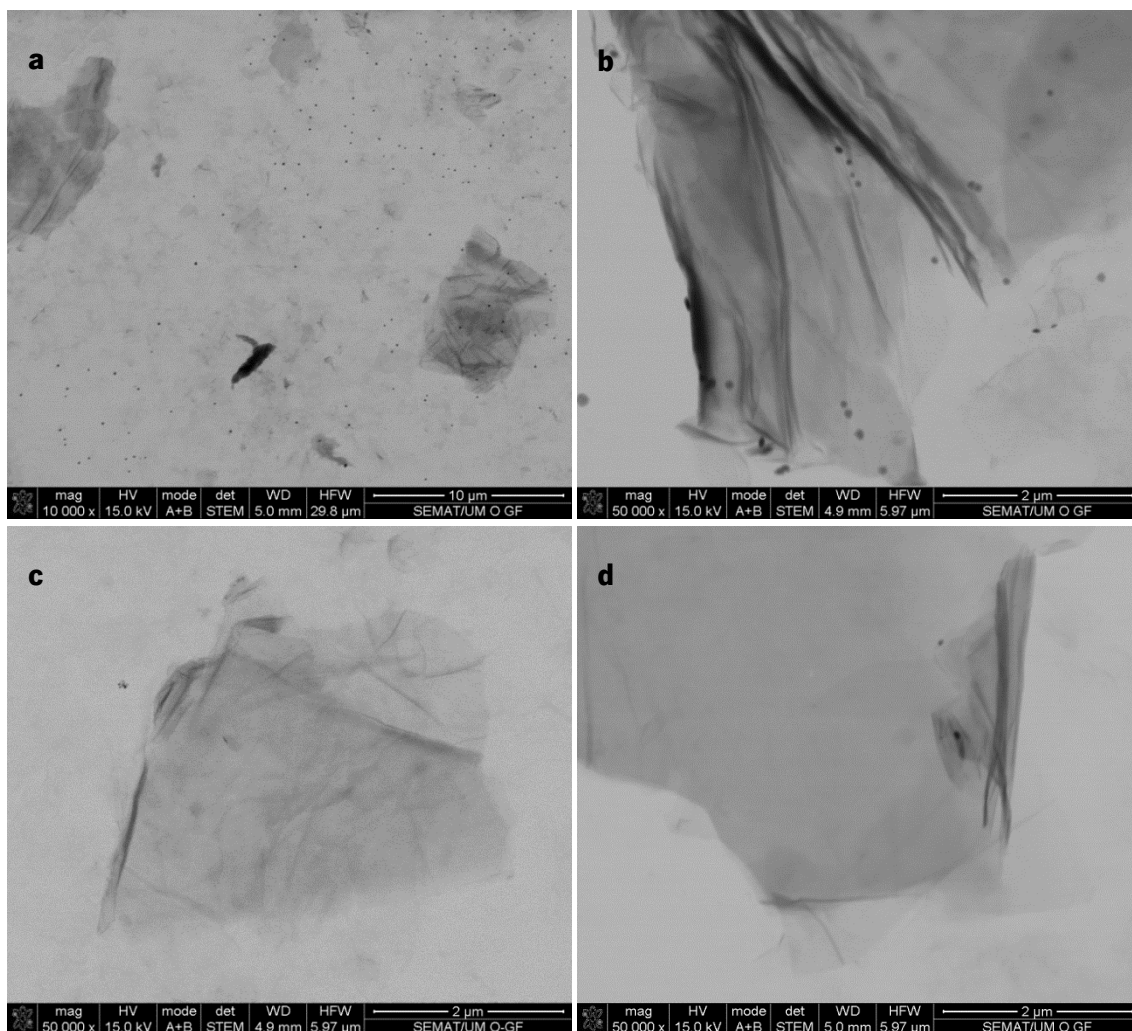
Figure 34: STEM images of o-GFs: **(a)** dispersed clusters of o-GFs with some visible impurities; **(b - d)** singles domains of o-GFs

An EDS analysis (figure 35) revealed the presence of Si and also C, N, O, Cl and K, also detected in the EDS analysis of f-GFs (figure 32).
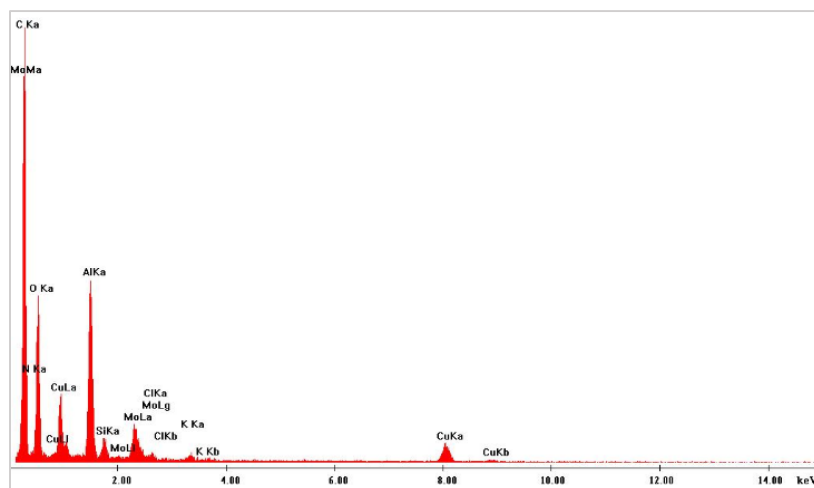
Figure 35: EDS analysis of o-GFs

Taking into account shapes and the way that those graphene flakes interact with each other, f-GNRs were chosen for STM analysis, as they are flat and this is an important requirement for the stability of the STM tip. However, it would be extremely difficult to find f-GNRs at this concentration under an STM, and so, the f-GNRs solution was further concentrated as mentioned in section 3.3.8.1.

4.1.5. Optical Microscopy

The OM images presented next aimed to evaluate the graphene patches size and density achieved by different deposition techniques on different substrates. This characterization allowed to select the best samples for further AFM characterization and later, STM analysis of the f-GNRs, prepared according to the best deposition technique.

Since the middle area is the main focus in STM analysis, the OM images presented here were taken from the middle area of each sample.

Figure 36 presents OM images of samples prepared by spin coating at 3500 rpm with 30 second cycles, for 1, 2, 3, 4, 7 and 12 cycles, on Au coated Si substrates.
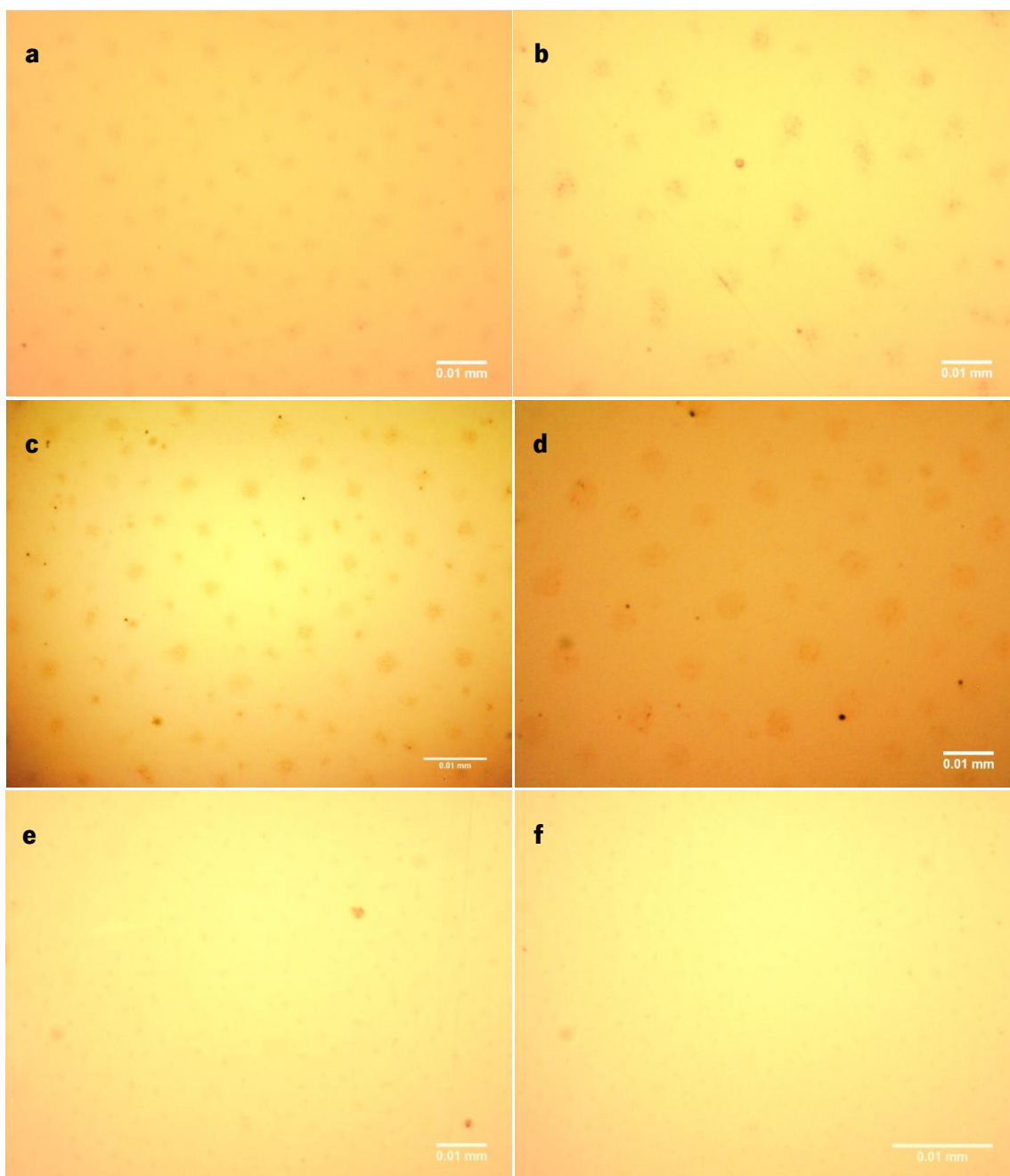
Figure 36: OM images of spin coated samples at 3500 rpm with 30 second cycles with different number of deposition cycles: **(a)** 1 deposition cycle (SC.1X.3500), **(b)** 2 deposition cycles (SC.2X.3500), **(c)** 3 deposition cycles (SC.3X.3500), **(d)** 4 deposition cycles (SC.4X.3500), **(e)** 7 deposition cycles (SC.7X.3500), and **(f)** 12 deposition cycles (SC.12X.3500)

It may be difficult to find and understand the effect of the number of deposition cycles on graphene patches size and density. Those samples prepared with 1 to 4 deposition cycles seem to have larger graphene patches with lower density than samples prepared with 7 and 12 cycles.

Analyzing samples SC.1X.3500 to SC.4X.3500, it appears that the number of cycles does not affect the graphene patches size and density because at each cycle, when more solution was added, it may re-dissolve and remove graphene that was deposited before. However, looking at

SC.7X.3500 and SC.12X.3500 samples, it is observed that the graphene patches are significantly smaller but denser, as if the addition of more graphene solution induced the separation into smaller graphene patches.

The substrates used were not perfect squares so it was not possible to perfectly center the substrates in the spin coater, which could induce film inhomogeneity.

For every spin coated sample it was possible to observe a higher concentration of graphene close to the sample edges.

Even though the number of cycles does not seem to affect the concentration of graphene patches, samples SC.1X.3500, SC.4X.3500 and SC.12X.3500, were analyzed by AFM.

Figure 37 shows an OM image of SC.7X.2000 sample, prepared by 7 cycles of spin coating, 30 seconds each, at 2000 rpm, on Au coated Si substrate.
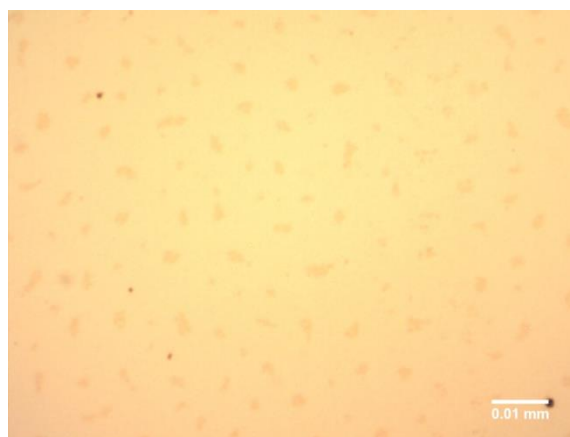
Figure 37: OM image of 7 deposition cycles spin coated sample at 2000 rpm with 30 second cycles (SC.7X.2000)

This image may be compared to figure 36 (e), with respect to sample SC.7X.3500, since they were subject to the same number of deposition cycles, in order to study the effect of spin speed.

The lower spin speed seems to decrease the graphene patches density and increase their size, as if the higher spin speed could spread out and separate the graphene patches into smaller graphene patches. This sample was further characterized by AFM.

Figure 38 are OM images of the spin coated samples prepared by an 11 mg/ml concentrated f-GNRs solution, with 1 cycle of 30 seconds, on Au coated Si substrates, using different spin speeds.

71
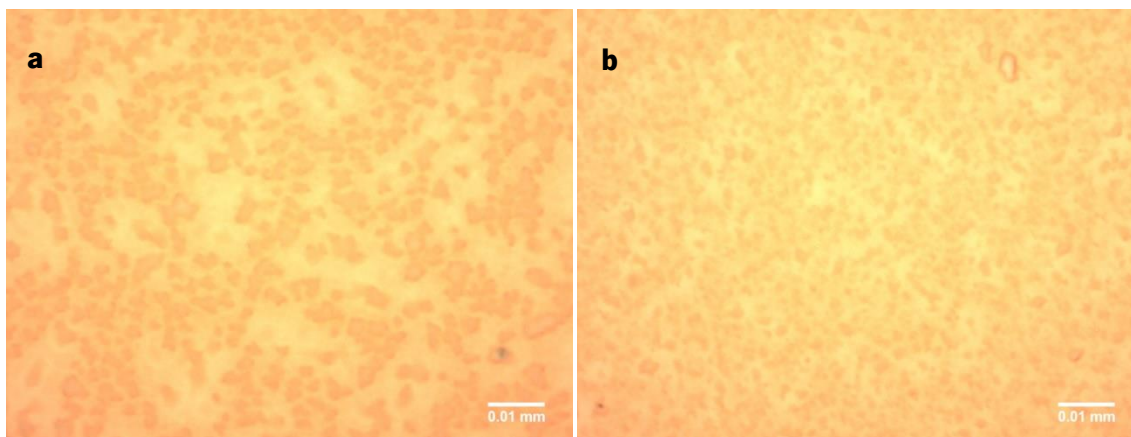
Figure 38: OM images of samples prepared by spin coating using an f-GNRs concentrated solution at different spin speeds: **(a)** 2000 rpm (SC.1X.2000.11), and **(b)** 3500 rpm (SC.1X.3500.11)

As observed before, it seems that the higher spin speed could spread out and separate the graphene patches into smaller graphene patches, which might lead to lower sample roughness, and that was evaluated by AFM analysis.

Figure 39 presents OM images of 2 samples prepared by droplet deposition in a hot plate, on Au coated Si substrates, using a volumetric pipette, varying the volume of f-GNRs solution by 0.2 and 0.4 ml, samples DD.HP.0.2 and DD.HP.0.4, respectively.
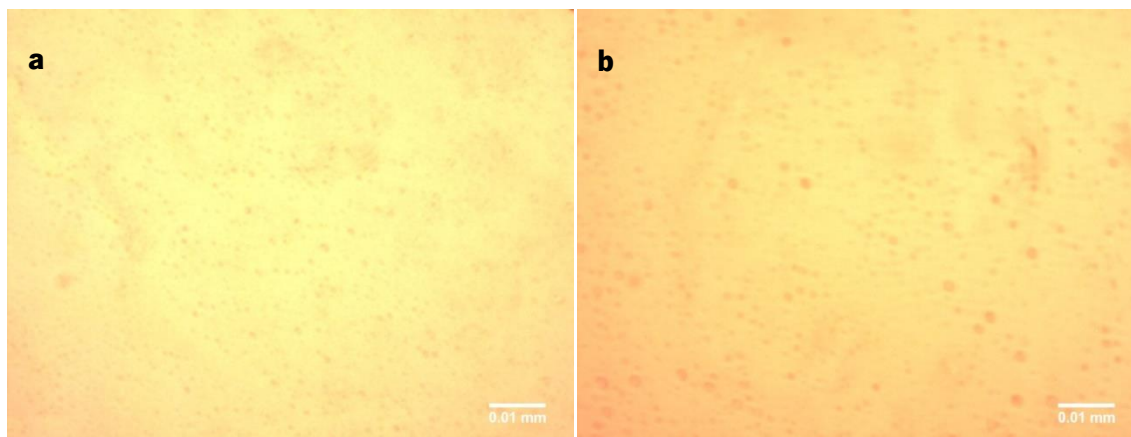
Figure 39: OM images of samples prepared by droplet deposition into a hot plate using a volumetric pipette with different volumes of f-GNRs solution: **(a)** 0.2 ml (DD.HP.0.2), and **(b)** 0.4 ml (DD.HP.0.4)

The graphene patches look well dispersed in both samples. It is possible to notice that graphene patches are larger in DD.HP.0.4 sample. Despite the good distribution of graphene patches, these samples were analyzed only through OM, since the graphene quality and functional groups might be compromised due to heating.

An OM image of DD.RT.0.4 sample, prepared by ethanol evaporation at room temperature, on Au coated Si substrate, is presented in figure 40.
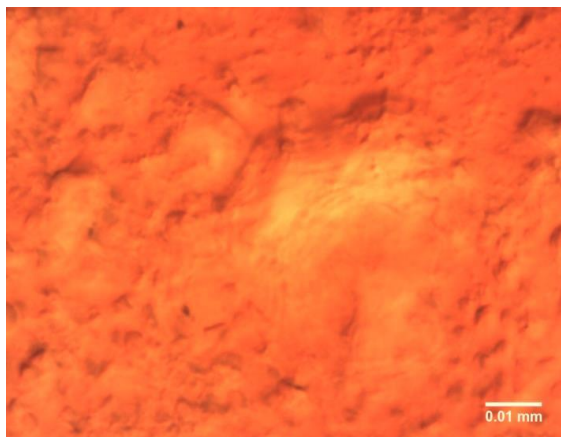
Figure 40: OM image of DD.RT.0.4 sample

As can be seen in figure 40, DD.RT.0.4 sample is very rough, which was also observable at the naked eye, thus this sample was considered not ideal for STM analysis, and thus it was not analyzed by AFM.

Figure 41 presents OM images of samples prepared by droplet deposition, on Au coated Si substrates, using a syringe, of 0.2 ml volume f-GNRs solution (DD.0.2.S) and 10 droplets of f-GNRs solution (DD.10drp.S), using the 2.2 mg/ml concentrated f-GNRs solution.
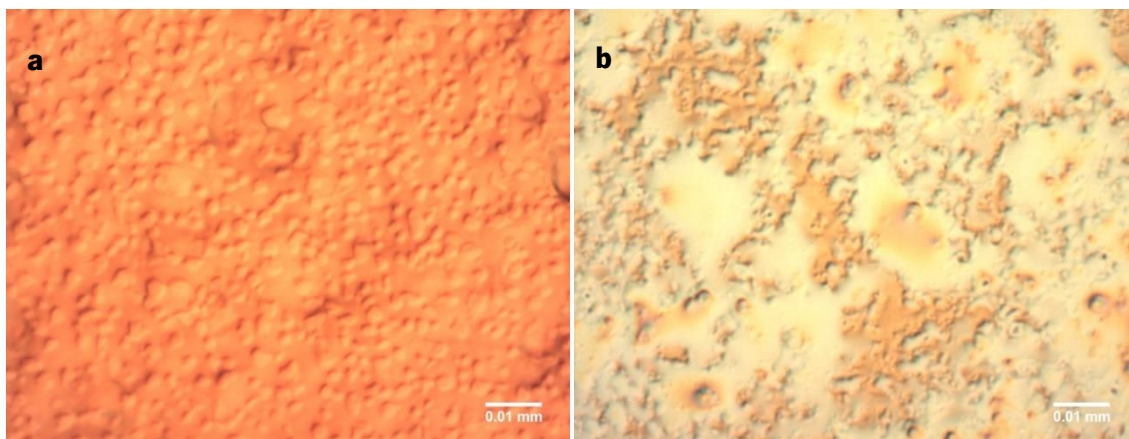
Figure 41: OM images of samples prepared by droplet deposition at room temperature using a syringe to deposit: **(a)** 0.2 ml f-GNRs solution (DD.0.2.S), and **(b)** 10 droplets of f-GNRs solution (DD.10drp.S)

Once again due to sample roughness, the DD.0.2.S sample was merely analyzed by OM, while DD.10drp.S was further analyzed by AFM.

An OM image of the DIP sample prepared by dipping of an Au coated Si substrate into the 2.2 mg/ml concentrated f-GNRs solution is presented in figure 42.
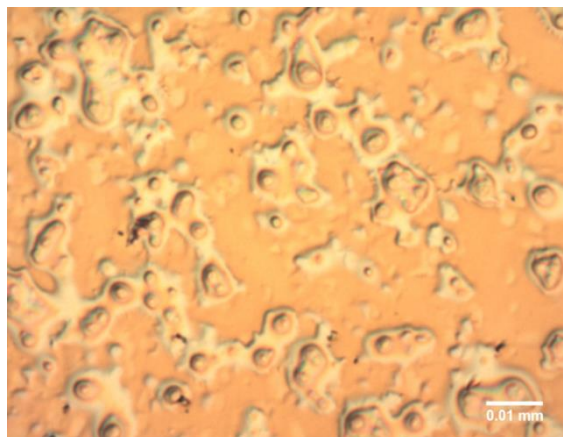
Figure 42: OM image of DIP sample

This sample was further analyzed by AFM. It appears that graphene is covering a great part of the substrate, which is an important advantage for STM experiments.

In summation, 9 of these 15 samples were further analyzed through AFM since they could be further observed by STM, or just to examine if there were further differences between them, for example, between those spin coated samples at 3500 rpm with 2.2 mg/ml f-GNRs solution. The samples DD.RT.0.4 and DD.0.2.S were immediately discarded of AFM analyzes because of their roughness (even at naked eye), and the 2 samples prepared by fast evaporation of ethanol on a hot plate were discarded as well, because it was likely that the graphene functional groups were damaged.

The same parameters of SC.1X.3500.11 sample were tested on Au coated mica and freshly cleaved HOPG substrates, and OM images are presented in figure 43.
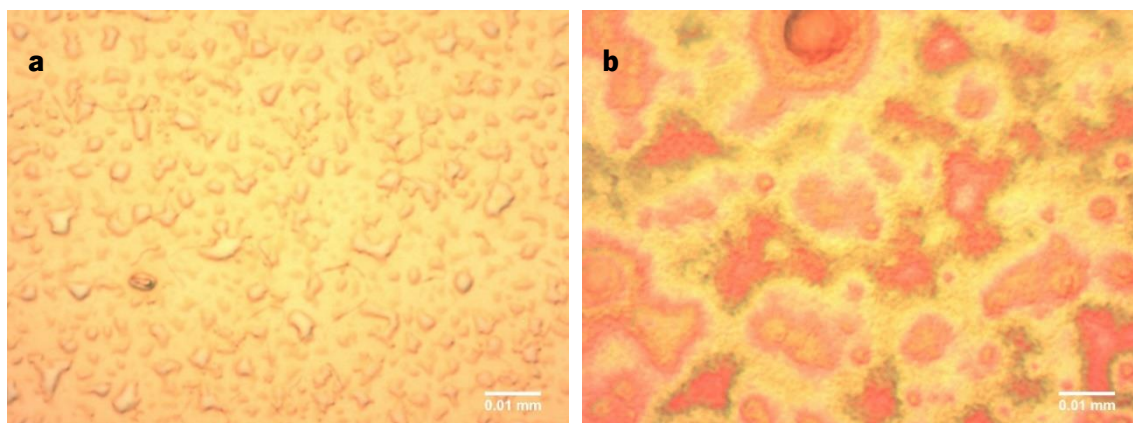
Figure 43: OM images of samples prepared by SC of 11 mg/ml concentrated f-GNRs solution on: **(a)** Au coated mica, and **(b)** HOPG

74

These OM images appear quite different from the SC.1X.3500.11 on Au coated Si substrate (figure 38 (b)), with larger and apparently, rougher structures. Both samples were analyzed by air-STM. Since it was possible, for the first time, to find GNRs on the SC.1X.3500.11.HOPG sample, this sample was also scanned on UHV-STM. However, it was not possible to resolve any feature on UHV-STM; it appeared that the tip was dragging material on the surface, which might be a consequence of high concentration and roughness.

Samples prepared by droplet deposition of 1 and 2.2 mg/ml concentrated f-GNRs solutions on HOPG, DD.2drp.1 and DD.1drp.2.2, are presented in figure 44.
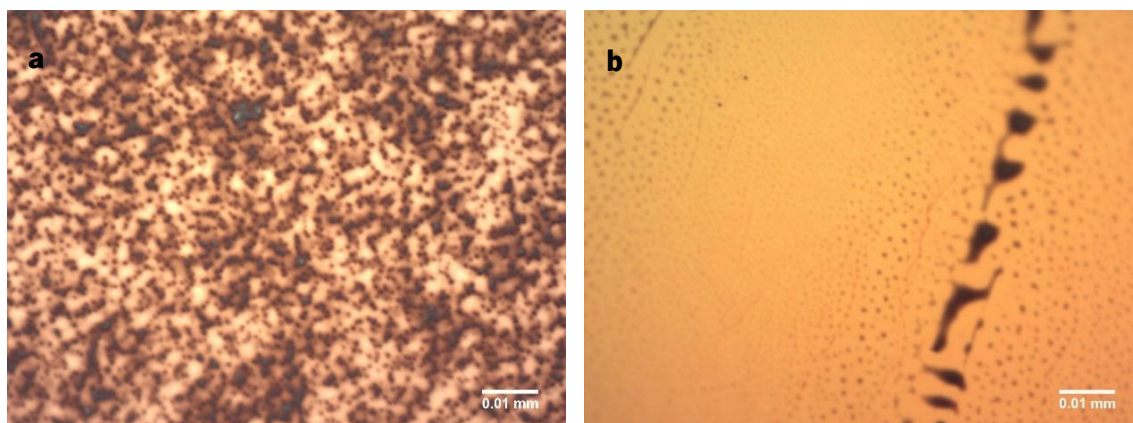
Figure 44: f-GNRs deposited on HOPG by droplet deposition: **(a)** 1 droplet of 2.2 mg/ml concentrated solution (DD.1drp.2.2); **(b)** 2 droplets of 1 mg/ml concentrated solution (DD.2drp.1)

Different deposited structures are observed. Somehow, the ethanol evaporation might be responsible for some of these features, for example, the large dark stains in figure 44 (b).

The OM image of f-GNRs on Au(111) substrate, prepared by droplet deposition of 1 droplet of 1mg/ml concentrated f-GNRs solution (DD.1drp.1.Au) is presented in figure 45.
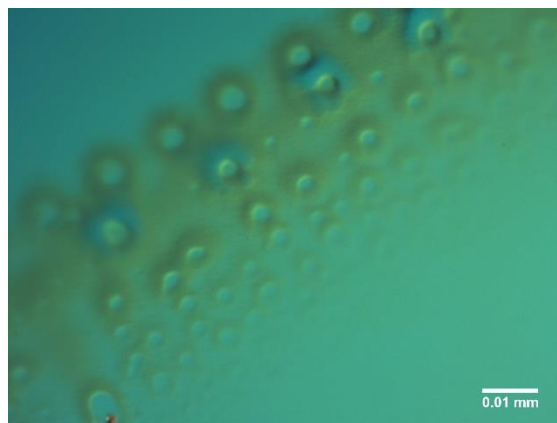
Figure 45: OM image of f-GNRs on Au(111) crystal

Again, the difference on the interference of these f-GNRs on different substrates, under OM, is noteworthy. Despite the morphological difference between this sample prepared on Au(111) crystal and the one prepared on HOPG substrate, DD.1drp.1.Au sample was observed by STM, as it is expected to find similar f-GNRs concentration on the surface.

OM was a very important first technique to study graphene patches density and size, and then to control and check every sample that were prepared.

4.1.6. Atomic Force Microscopy

After samples selection by OM, samples that might be amenable to be analyzed by STM were further analyzed by AFM.

Figures 46 to 48 show samples where graphene was deposited by spin coating at 3500 rpm, carried out with 1, 4 and 12 cycles, on Au coated Si substrates.
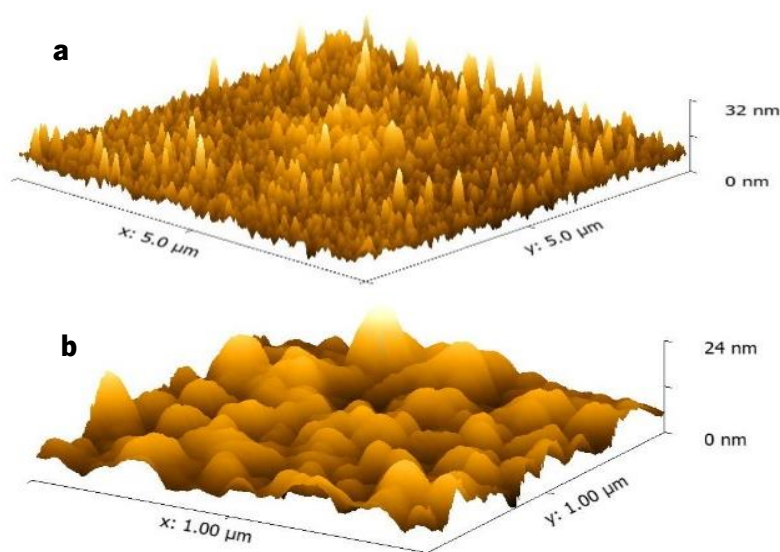
Figure 46: AFM images of SC.1X.3500 sample at different scales: **(a)** 5 µm; **(b)** 1 µm
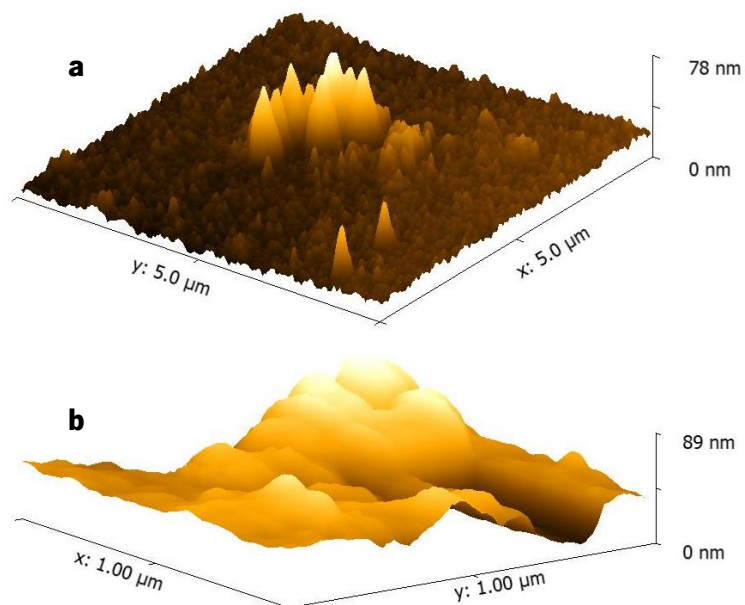
Figure 47: AFM images of SC.4X.3500 sample at different scales: **(a)** 5 µm; **(b)** 1 µm
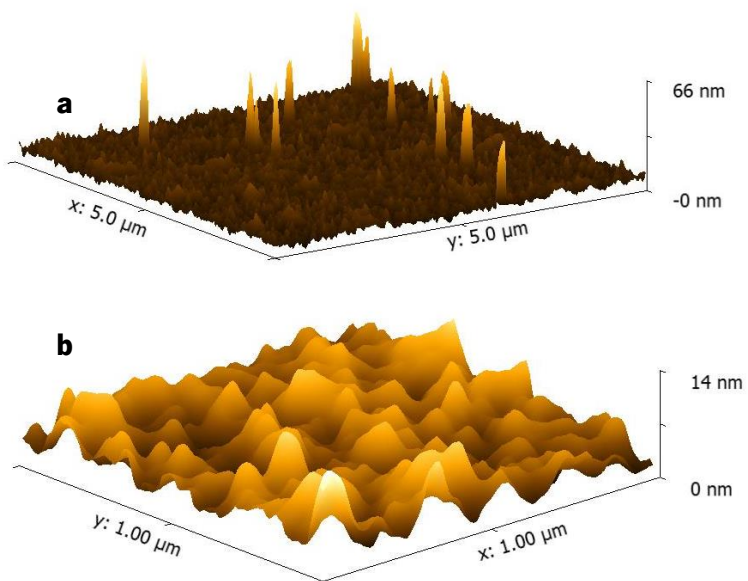
Figure 48: AFM images of SC.12X.3500 sample at different scales: **(a)** 5 µm; **(b)** 1 µm

Figure 49 presents AFM images of SC.7X.2000 sample, prepared by 7 cycles of spin coating at 2000 rpm.
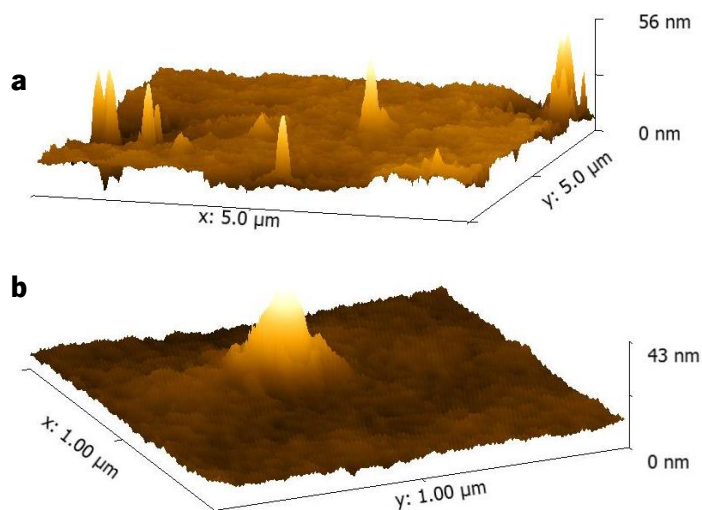
Figure 49: AFM images of SC.7X.2000 sample at different scales: **(a)** 5 µm; **(b)** 1 µm

Samples prepared by a single cycle spin coating using the 11 mg/ml concentrated f-GNRs solution, at different spin speeds, 2000 and 3500 rpm, are presented in figures 50 and 51.
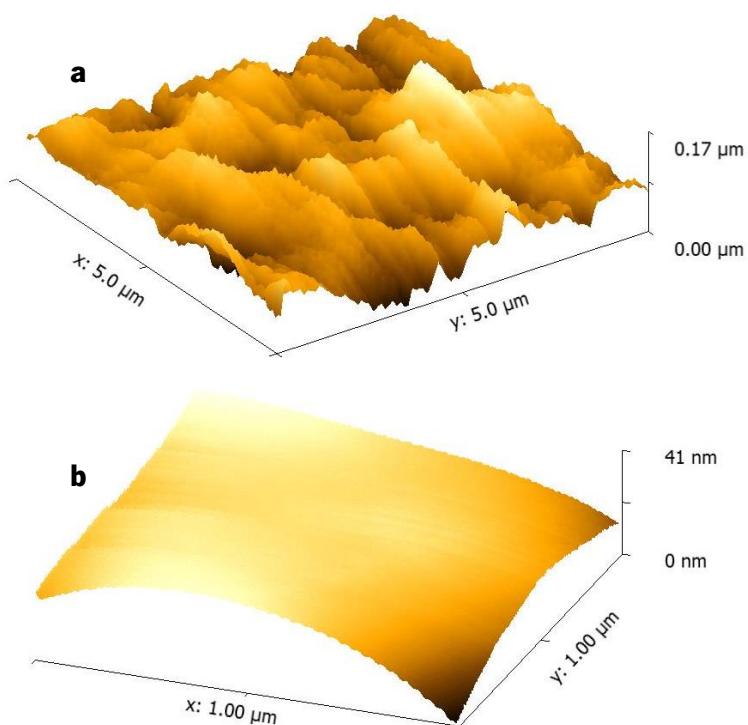
Figure 50: AFM images of SC.1X.2000.11 sample at different scales: **(a)** 5 µm; **(b)** 1 µm
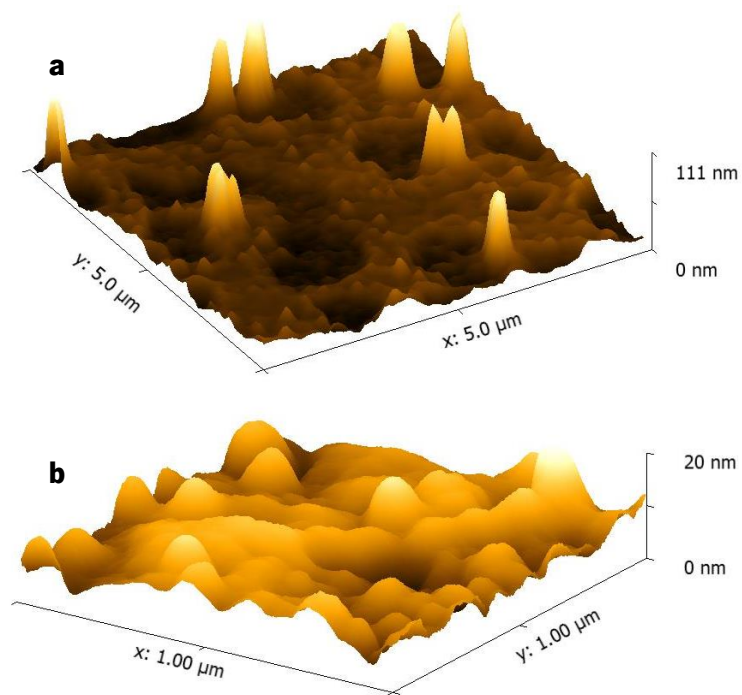
Figure 51: AFM images of SC.1X.3500.11 sample at different scales: **(a)** 5 μm; **(b)** 1 μm

Figure 52 presents AFM images of DD.10drp.S sample, prepared by droplet deposition of 10 droplets of f-GNRs solution using a syringe.
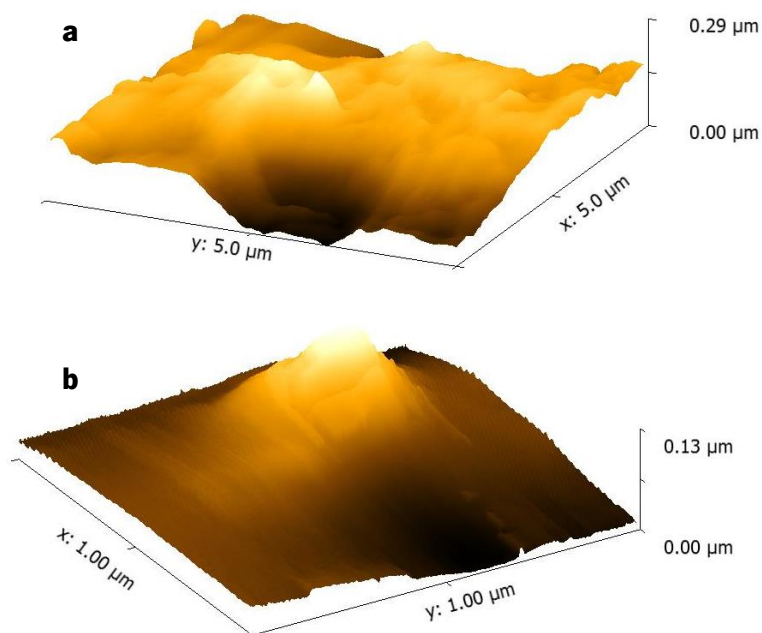
Figure 52: AFM images of DD.10drp.S sample at different scales: **(a)** 5 μm; **(b)** 1 μm

AFM images of the DIP sample, prepared by immersion of the substrate into the f-GNRs solution, are presented in figure 53.

79
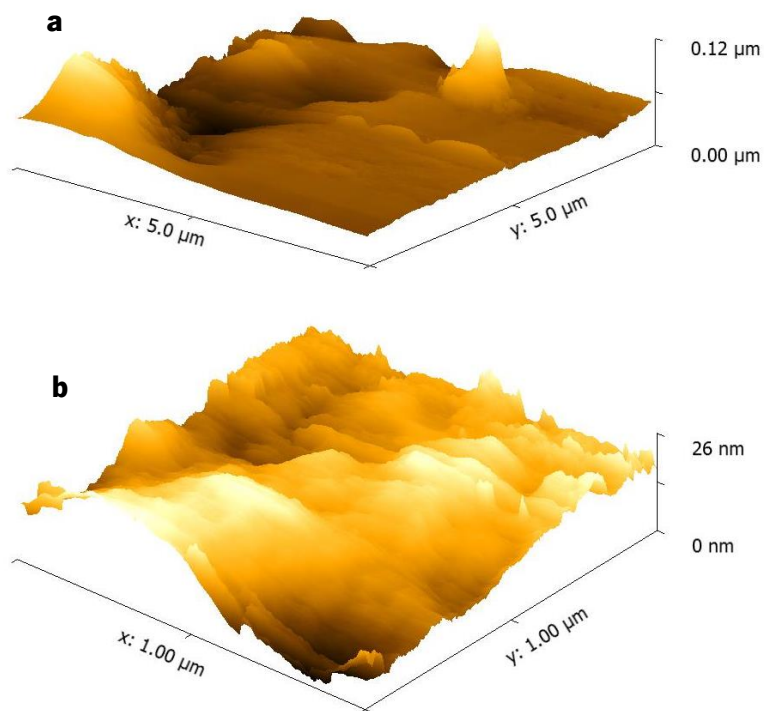
Figure 53: AFM images of DIP sample at different scales: **(a)** 5 µm; **(b)** 1 µm

The software Gwyddion used to measure surface roughness, presented on table 5, in terms of the root mean squared (RMS) roughness. 50 µm size images were used to obtain RMS roughness in order to get representative values of each sample, which would be difficult using smaller image sizes, as those presented above. Exceptionally, the RMS roughness of the substrate, Ref.Au, was obtained through a 60 µm size image.

Table 5: RMS roughness of AFM images

Sample	RMS (nm)
Ref.Au	2.4
SC.1X.3500	4.5
SC.4X.3500	2.8
SC.12X.3500	3.2
SC.7X.2000	3.4
SC.1X.2000.11	48.7
SC.1X.3500.11	45.1
DD.10drp.S	60.6
DIP	112.8

The samples prepared by spin coating at 3500 rpm using the 2.2 mg/mg concentrated f-GNRs solution present the same order of magnitude of RMS roughness, which could also be an indication that each new spin coating cycle removes the previously deposited graphene.

The increase of the f-GNRs solution concentration (SC.1X.3500.11 and SC.1X.2000.11 samples) increased the density of graphene patches, as it can be clearly seen on the OM images. On the other hand these samples presented higher roughness when compared to those prepared by spin coating, either at 2000 or 3500 rpm, using the lower solution concentration.

Both DIP and DD.10drp.S samples proved to be considerably rough.

According to the roughness values obtained by AFM analysis, and graphene patches density evaluated by OM images, the parameters used on sample SC.1X.3500.11 were selected to produce a sample with an Au coated Si substrate 7x7 mm dimensions for air-STM analysis.

Further studies on other substrates were only performed by OM.

4.1.7. Scanning Tunneling Microscopy

Scanning Tunneling Microscopy was used to study graphene at atomic scale and later to evaluate its electronic properties using a LT-STM.

Image dimensions and parameters (tunneling current, I_t, and tunneling voltage, V_t) for each image scanned are described on each figure caption. The images presented are for f-GNRs deposited on HOPG.

Images of samples deposited on Au coated Si, Au coated mica and Au(111) substrates are not presented here, since no image of f-GNRs was obtained due to high corrugation of theses substrates, especially for Au coated Si.

4.1.8.1. Air-STM

The Aarhus air-STM was a fundamental technique to observe the distribution of GNRs for later study in an Aarhus UHV-STM and Createc LT-STM. Additionally, the air-STM was important to understand the STM principles and fundamentals in a user perspective. For example, figure 54 shows a f-GNR found while scanning on DD.2drp.1 sample, where is possible to see the result of a "double tip", once double features are observed.
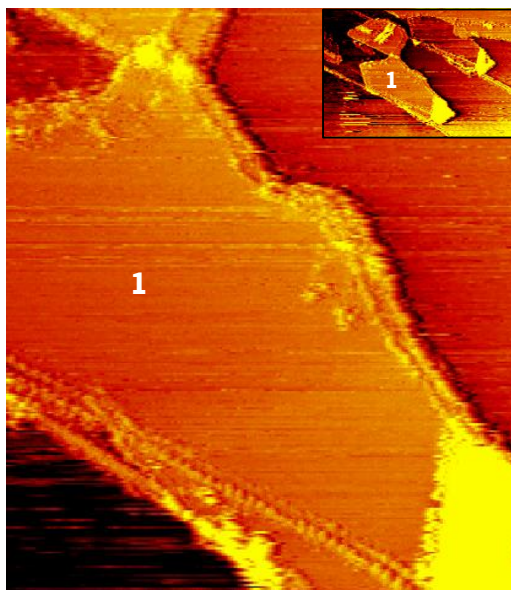
Figure 54: Image resulting from a "double-tip" (115x132 nm, 1.030 nA, 10.4 mV). The image on the upper right corner shows 2 more GNRs found close to GNR 1

Two more f-GNRs were found close to the f-GNR in figure 54 (see upper right corner), sitting on a HOPG step edge, presenting similar dimensions to f-GNRs 1 (approximately 170 nm long and 60 nm wide).

In figure 55 a flat monolayer f-GNR is presented, scanned on sample DD.1drp.2.2. Atomically resolved images of the edge were obtained and are presented in figure 56 for three different areas (highlighted with white ellipses in figure 55 (b)).
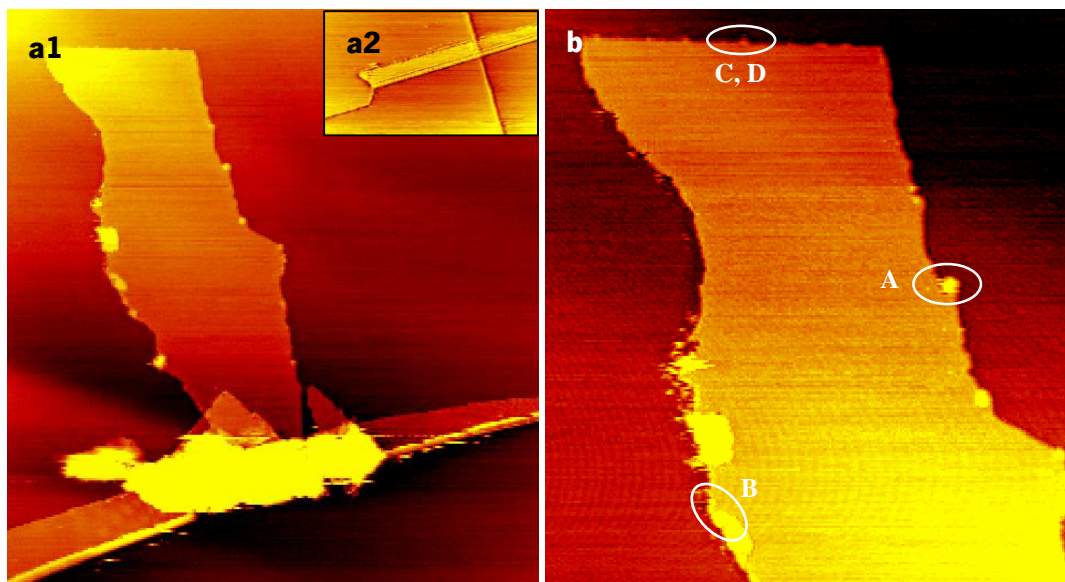
Figure 55: (a1) vertically oriented f-GNR scanned on DD.2drp.1 sample with a possible f-GNR horizontally oriented on the bottom (328x357 nm, -1.010 nA, -26 mV); **(a2)** Left extremity of the "bottom GNR" in (a1); **(b)** vertically oriented f-GNR in (a1) (164x179 nm, -1.090 nA, -26 mV)

Occasionally, it could be difficult to interpret specific features. For instance, in figure 55 (a2), it is not clear if that is an f-GNR or simply a folded HOPG step edge. The feature observed in figure 55 (a2) is what appears like a GNR sitting below the larger GNR, horizontally oriented, across the entire figure 55 (a1).
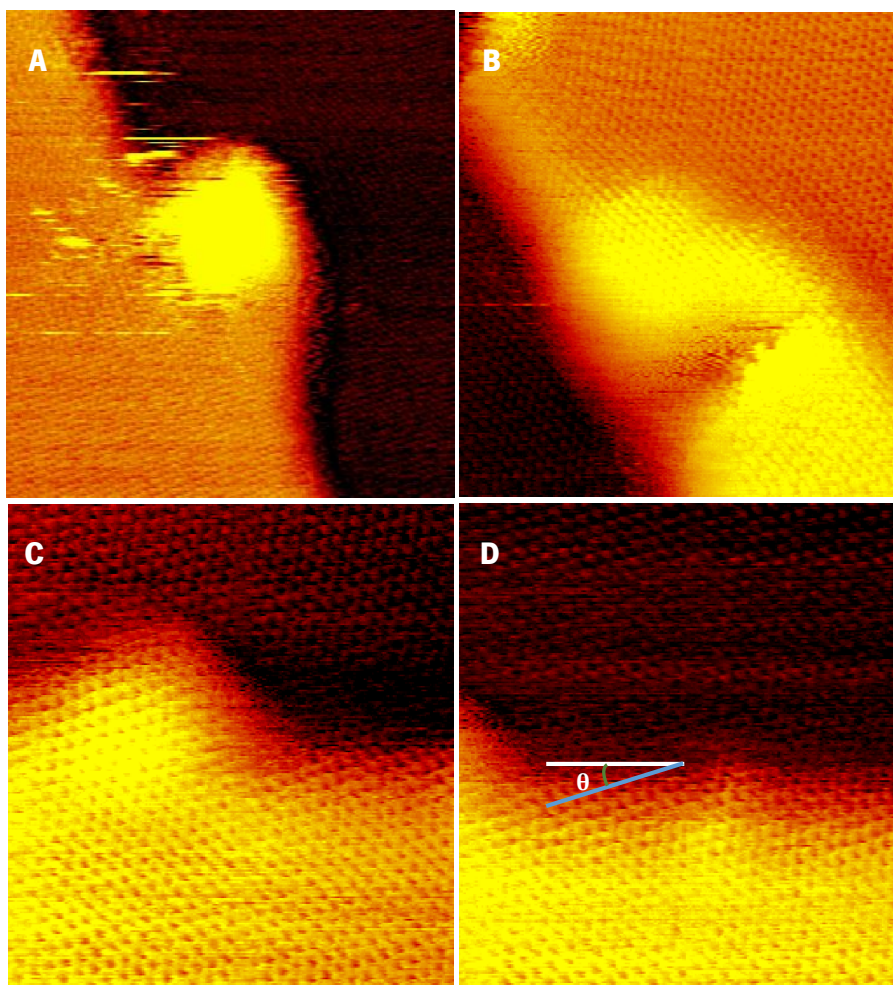
Figure 56: Atomically resolved images of the f-GNR at different areas pointed in figure 55 (b); **(A)** 16.4x17.8 nm, -1.040 nA, 26 mV; **(B)** 10.9x11.9 nm, -1.090 nA, -26 mV; **(C)** 7.7x8.3 nm, -1.080 nA, -26 mV; **(D)** 7.7x8.3 nm, -1.050 nA, -26 mV

These atomically resolved images could be used to calculate the GNR chirality. The chiral angle, θ, is given by the angle between a line following the zigzag direction and a line following the edge termination (blue and white lines, respectively, in figure 56 (D)) [33]. Resorting to ImageJ software, the chiral angle θ in figure 56 (D) was measured to be approximately 14°. These measurements are interesting when it is possible to simultaneously measure the electronic properties, to study and establish relations between electronic and atomic structure of GNRs [33].

The HOPG substrate revealed a trigonal lattice, while the GNR revealed a hexagonal lattice.

Along the f-GNR edge it is possible to observe several structures with an almost globe-like aspect, as in figure 56 (A), (B) and (C). These features could be due to functional groups sitting under the GNR.

A GNR longer than 1 µm, is presented next in figure 57 (a), sitting across a HOPG step edge.
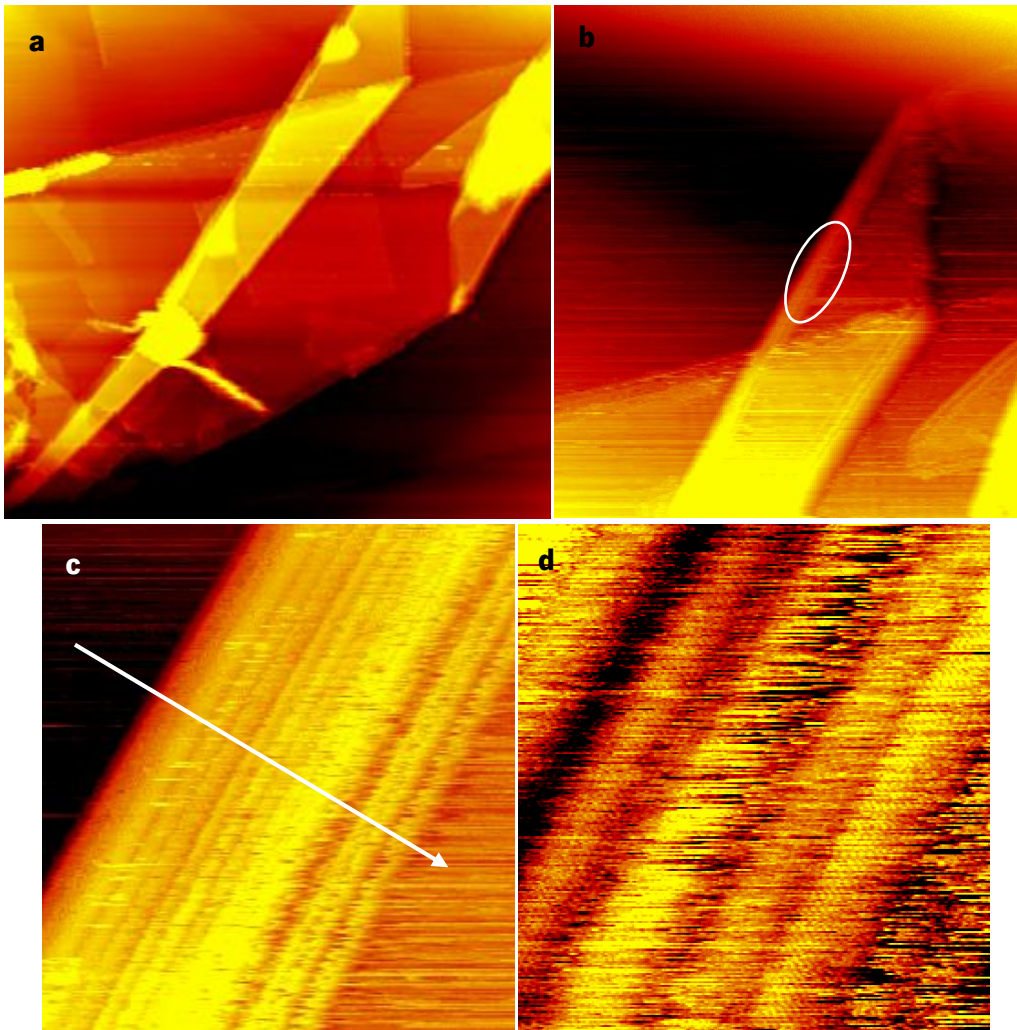
Figure 57: (a) GNR across a HOPG step edge (1081x1013 nm, -1.060 nA, -26 mV); **(b)** GNR upper area (765.8x833.0 nm, -2.140 nA, -26 mV); **(c)** GNR edge in area signalized in (b) (76.6x83.3 nm, -0.860 nA, -26 mV); **(d)** atomically resolved image of the GNR edge (16.4x17.8 nm, -1.020 nA, -168.5 mV)

Figure 57 (c) and (d) are images of the GNR edge on the area signalized in figure 57 (b) and a height profile along the white line on figure 57 (c) is presented in figure 58. Atomically resolved images were attained on this GNR edge (figure 57 (d)).
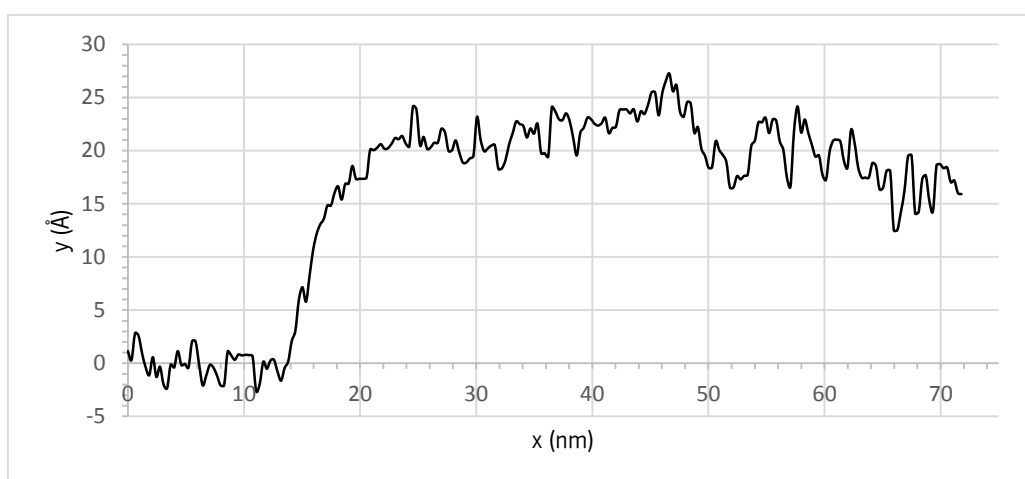
Figure 58: Height profile of the f-GNR edge along the line on figure 57 (c)

According to X-ray Diffraction (XRD) results, supported by theoretical calculations (not published yet), these f-GNRs tend to stack with interlayer distances of about 0.5 nm (which is higher than the graphite value 0.335 nm [14]). Figure 58 shows that this f-GNR is about 2 nm high, corresponding to a 4-layers GNR. However, these 4 layers are not perceptible on this height profile graph neither in the STM images (figure 57 (c) and (d)). These laminated structures on the GNR edge appear very smooth on the height profile graph (length axis between ˜ 14 and 65 nm), making it difficult to distinguish different layers.

4.1.8.2. UHV-STM

The f-GNRs were analyzed by UHV-STM, as well, and a stack of f-GNRs was observed on figure 59. This f-GNR was imaged on a sample prepared following DD.2drp.1 sample.

In figure 59 (a), a feature that appears like a GNR in one extremity of a folded HOPG layer is observed. This GNR is approximately 140 nm wide and approximately 28 Å high, as measured in figure 59 (b). A magnification of figure 59 (a) can be seen on figure 59 (b), where it is possible to distinguish a folded single layer GNR on top, as may be verified by the height profile graph in figure 60 (blue height profile), where the height difference between the 2 consecutive layers is about 6 Å, a value similar to that measured on XRD and theoretical predictions.
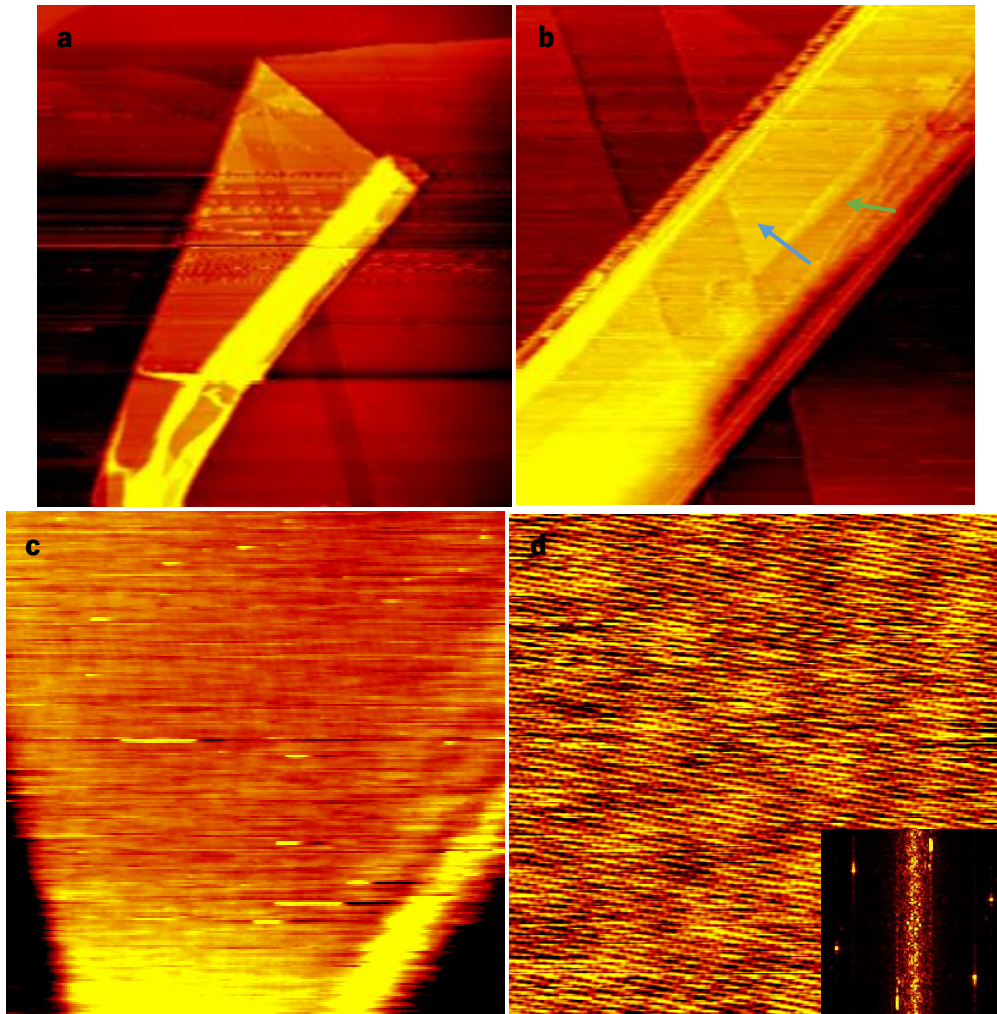
Figure 59: (a) 140 nm wide GNR (1111x1171 nm, -1.110 nA, -758 mV); **(b)** magnification of the GNR in (a) (358x393 nm, -0.560 nA, -691 mV); **(c)** Moiré pattern on top of the GNR (59.7x60.1 nm, -0.550 nA, -691.2 mV); **(d)** Moiré pattern on top of the GNR and FFT (16.5x16.7 nm, -0.350 nA, -999.1 mV)
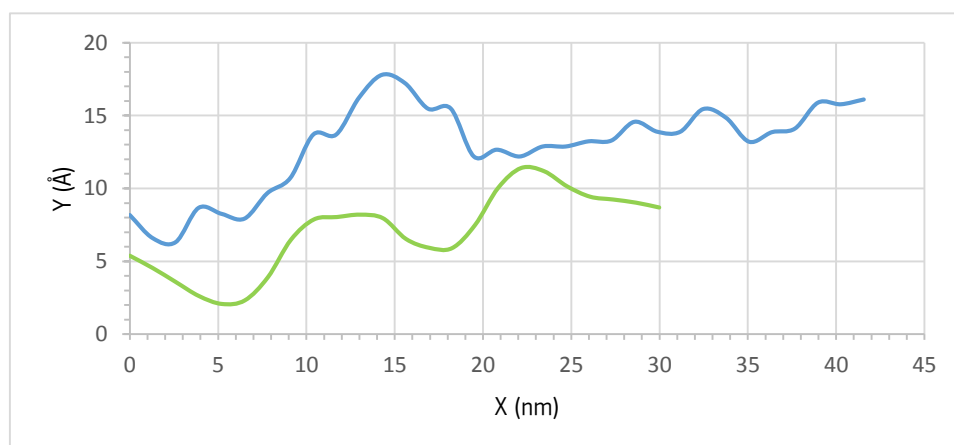
Figure 60: Height profile along blue and green arrows in figure 59 (b)

In the green height profile of figure 60, a height profile along the green arrow on figure 59 (b), is possible to measure an interlayer distance between 4 and 6 Å between these 3 layers, not far from the previous results.

Moiré patterns, superstructures observable by STM due to adjacent lattice mismatches [121], [122], were imaged in figure 59 (c) and even at atomic scale in figure 59 (d). A FFT is presented on right lower corner of figure 59 (d), which allowed to calculate a graphene lattice constant of 2.5 ± 0.1 Å and a Moiré pattern periodicity of 35.7 ± 3.5 Å.

Some difficulties were found when scanning these f-GNRs on HOPG, as GNR mobility could be noticed while scanning over the same area. Also, distinguish between HOPG steps and GNRs was sometimes difficult due to their atomic structure similarities. To overcome this problem f-GNRs were deposit on Au(111) crystal substrate but it was not possible to image any GNR.

4.1.8.3. LT-STM

The f-GNRs were analyzed in a Createc LT-STM cooled down to 77 K, by liquid nitrogen, aiming to study their electronic properties.

The stability of the tip was not easy to achieve since the temperature was not low enough for this type of measurements. However, to a certain extent, some measurements were reproducible, on the GNR presented in figure 61.
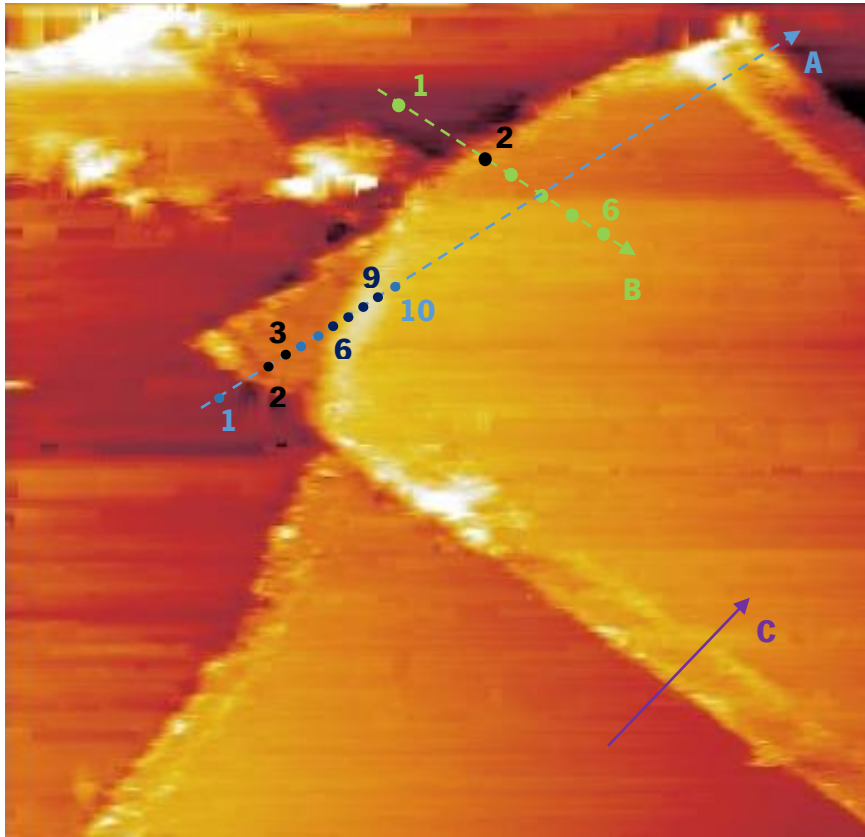
Figure 61: LT-STM image of a functionalized GNR (105x105 nm, 0.44nA, 411 mV)

The GNR presented in figure 61 is sitting on a HOPG step edge and has a width of approximately 70 nm.

STS measurements were obtained at those points along the blue (A) and green (B) arrows (figures 62 and 63, respectively) and height profiles along arrows A, B and C are presented in figure 66. Figure 62 presents stacked differential conductance measured at the points at the blue arrow, where dot number 1 is on HOPG, dots 2 and 3 are close to the GNR edge, dots 4 and 5 are on the interior of the corner of the GNR sitting on the HOPG, dots 6 to 9 are on the brighter region between the corner and the interior of the GNR sitting in another HOPG step edge, and dot number 10 is on the interior of the GNR sitting in the second HOPG step edge. Figure 63 presents stacked differential conductance measured at the points at the green arrow, where dot number 1 is on HOPG, dot number 2 is on the GNR edge and dots 3 to 6 are on the interior of the GNR.
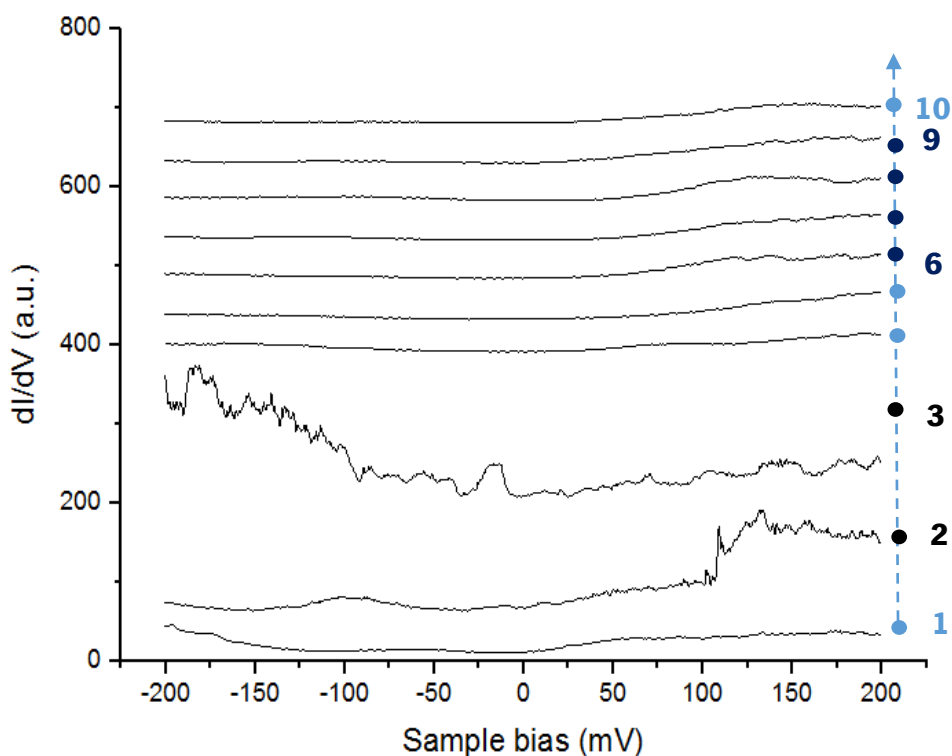
Figure 62: Stacked differential conductance at the blue and dark dots along the blue arrow in figure 61. The dots are not placed in the same distances of figure 61 since they were shifted to be side by side with the respective differential conductance curve
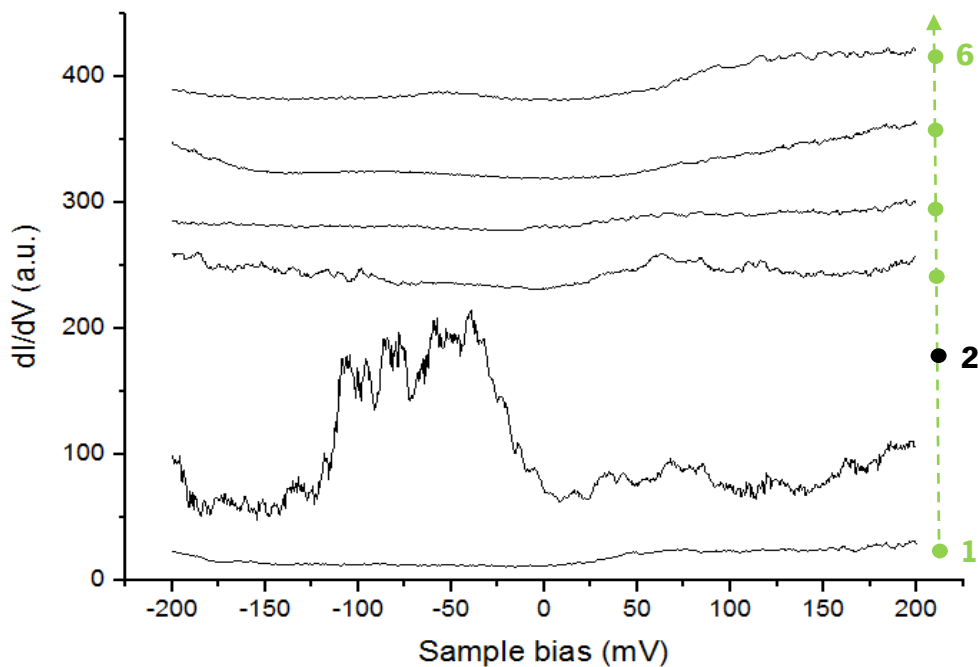
Figure 63: Stacked differential conductance at the green and dark dots along the green arrow in figure 61. The dots are not placed in the same distances of figure 61 since they were shifted to be side by side with the respective differential conductance curve

A higher intensity of differential conductance (dI/dV), is observable at the GNR edges, marked with black dots at both blue and green arrows. This higher current is owed to the LDOS at the GNR edge, which might be due to the presence of the protruding functional groups at these locations. Within the GNR, the STS is not symmetrical: higher signals are observed for positive bias corresponding to the conduction/ empty band.

Three different measurements of this type were done across the right side edge of the GNR in figure 61, from the HOPG substrate towards the interior of the GNR (figure 64), and a representative one is presented in figure 65. Although tip instability was noticed, among the 3 measurements higher intensities of differential conductance were observable around the GNR edge, as well.
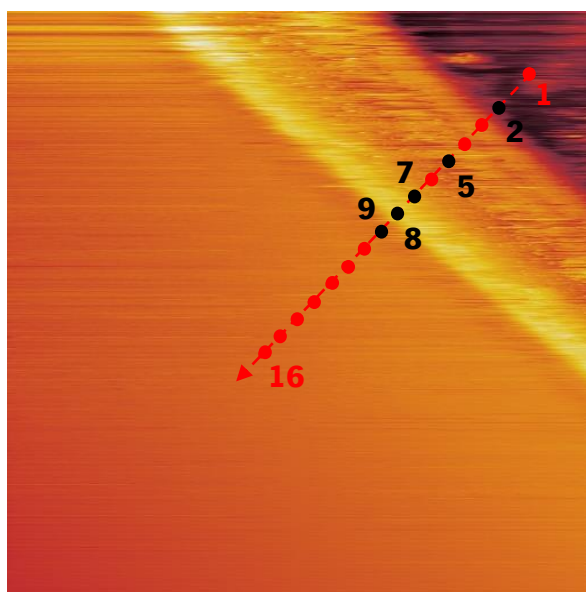
Figure 64: Right side edge of the GNR presented in figure 61 (31x29 nm, 0.44 nA, 291 mV)
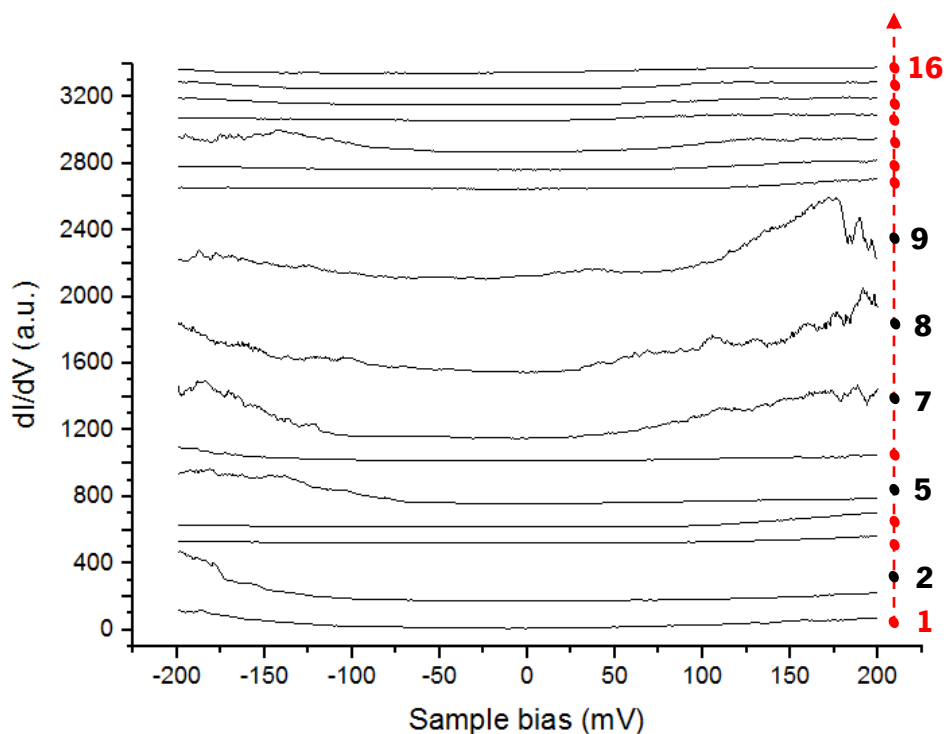
Figure 65: Stacked differential conductance at the red and dark dots along the red arrow in figure 64. The dots are not placed in the same distances of figure 64 since they were shifted to be side by side with the respective differential conductance curve

Similarly to what was observed before, the signal is high at the GNR edge, between HOPG and the very extremity of the GNR (black dot number 2). Additionally, high current densities were also observed between the interior of the GNR and the left side of the edge (black dots number 7 - 9), and in the middle of the edge (black dot number 5). The black dot number 5 has the lowest STTS values among the black dots, where dots 7 to 9, present the highest STS values. Functional groups are also likely to be sitting at these locations.

Height profiles along arrows A, B and C of figure 61 are presented in figure 66.
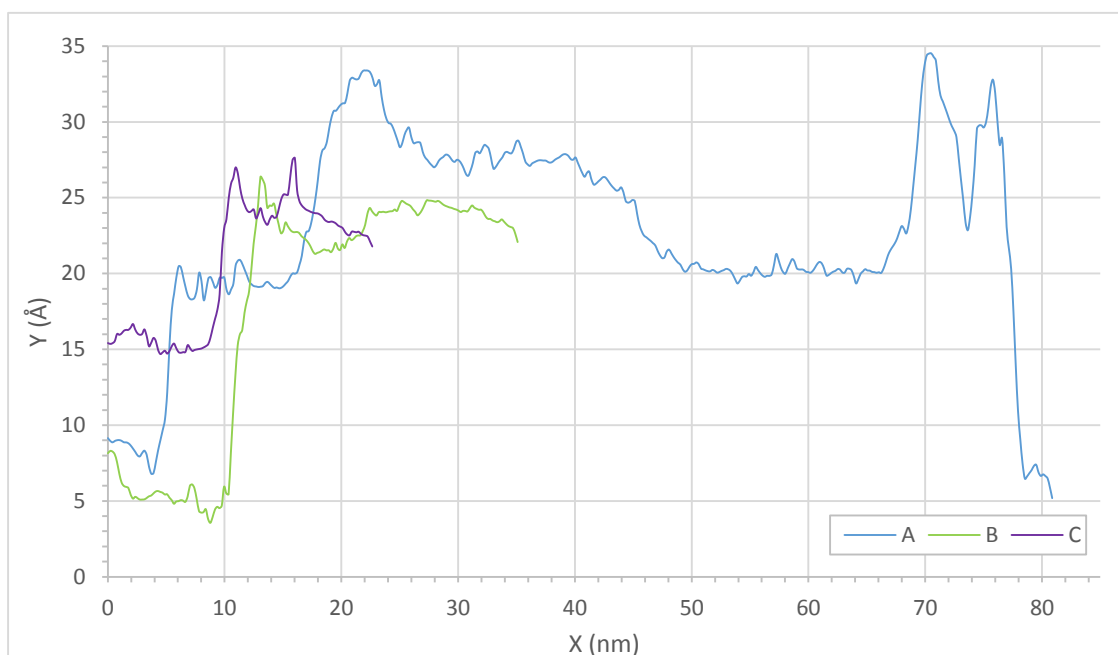
Figure 66: Height profiles along arrows A, B and C in figure 61

Profile A passes along the line of blue dots in figure 61 and in a similar place to the red dots on figure 64, and profile B passes along the arrow under the green dots in figure 61.

The GNR edge present different features. A 'valley' shape is observed in profiles A (at the right side edge, at ~70 nm) and C, approximately 15 Å high for profile A and 5 Å high for profile C, and both are approximately 5 nm wide. Profile B presents a 'quasi-conical' shape feature, about 5 Å high and 5 nm wide. At the left side edge of the GNR in profile A, an irregular shape is observable in an extension of approximately 5 nm with a maximum height of 3 Å, followed by a 'quasi-conical' shape feature, with a height of about 5 Å and width of 8 nm, when the GNR meets the HOPG step edge. With exception of the right and left side edges of the GNR in profile A, all other features present a height of about 5 Å, similar value to the interlayer spacing of these GNRs. The height values were measured relatively to the mid-plane terrace of the GNR.

L. Jiao et al. claims that they are able to distinguish between terminal curved edges and folded edges. A terminal curved edge presents a 'hump' feature with a height of 3.2 Å above the mid-plane terrace of the GNR, while a folded edge presents 2 or 3 times this value [33]. This statement might mean that the GNR presented in figure 61 presents top and left side terminal curved edges and a right side folded edge. The black points with higher energy of the LDOS are coincident with these taller regions at the GNR edges.

In the upper-left corner of the GNR, a transition from a dark to a bright area is observable, where Profile A and dark blue (6 - 9) dots in figure 61 pass along. Even though, a topography peak is observable in this area in figure 66, a higher value of STS is not observable in figure 65 for dots 6 – 9, and they present a similar shape to those within the GNR, which shows that this brighter area is due to the GNR topography, where a new HOPG step edge starts.

In none of the observed f-GNRs was possible to positively identify the presence of functional groups, however the different differential conductance measured at the GNR edges might indicate that the functional groups are concentrated in these regions.

4.1.8. Zeta Potential

The ZP of the 4 different graphene solutions produced was measured. Besides to as-prepared graphene solutions, other polyelectrolytes containing both ALG and graphene, with different solvents (different fractions of DW and ethanol) were also prepared, as described in section 3.4, and their ZP was measured. The ZP results are presented in table 6.

The ZP results allowed to choose polymeric electrolytes (PE) with an adequate charge for the LbL film production, i.e., opposite to that measured in those solutions prepared. The PE chosen for each graphene solution is indicated in table 6, as well.

Table 6: ZP of graphene solutions and chosen PE

Sample	ZP (mV)	PE
f-GNRs	+2.1 ± 1.3	ELP
f-GFs	+16.2 ± 0.7	ALG
o-GNRs	-59.5 ± 0.3	CHT
o-GFs	-35.0 ± 1.1	CHT
f-GNRs-50	-4.6 ± 0.2	ELP
f-GFs-50	-1.0 ±0.1	ELP
f-GNRs-ALG	-21.8 ± 0.8	CHT
f-GFs-ALG	-26.0 ± 0.9	CHT

As expected, f-GNRs and f-GFs present a positive ZP, +2.1 ± 1.3mV and +16.2 ± 0.7 mV, respectively, since they are amine functionalized, and similarly to the literature, o-GNRs and o-GFs present a negative ZP [113], -59.5 ± 0.3 mV and -35.0 ± 1.1 mV, respectively.

f-GFs revealed a reasonable ZP to be used in LbL assembly boosted by electrostatic interactions, while, in the other hand, f-GNRs revealed a low charge, not so favorable for the same purpose. Therefore, the PE indicated in table 6 were chosen based on their charge and graphene solutions charge, their adequate properties regarding biomedical applications and also because they have demonstrated their great ability for LbL assembly [66], [123]. CHT was chosen as a PC to be used together with f-GFs and also to produce multilayer films together with o-GFs and o-GNRs, through the LbL technique. For f-GNRs an elastin-like polymer (ELP) was used instead of CHT, since adsorption of proteins may include many other interactions than electrostatic interactions, such as van der Waals, hydrophobic interactions and hydrogen bonding [123]. This feature could boost the adsorption of f-GNRs in a LbL approach. An ELP is a biocompatible biopolymer, bioengineering made, inspired on human elastin, and consists on short repeating peptide sequences [123], [124].

The f-GNRs (f-GNRs-50) and f-GFs (f-GFs-50) solutions dissolved in 50% ethanol and 50% DW, surprisingly turned out to have a negative ZP, an opposite charge to the as-obtained f-GNRs and f-GFs (dissolved in ethanol). Since these solutions also revealed a low ZP, -4.6 ± 0.2 mV and -1.0 ±0.1 mV, for f-GNRs,50%et,50%DW and f-GFs,50%et,50%DW, respectively, they were tried with ELP. The ELP used presents a slightly positive ZP, +1.6 ± 0.1 mV [61].

A mixture of ALG with f-GNRs dissolved in 25% ethanol and 75% DW (f-GNRs-ALG) and a mixture of ALG with f-GFs dissolved in 25% ethanol and 75% DW (f-GFs-ALG) revealed negative ZP, -21.8 ± 0.8 mV and -26.0 ± 0.9 mV, respectively, suitable to be used together with the PC CHT.

4.2. Multilayer films Assembly

The multilayer films assembly was monitored using a QCM-D. The QCM-D is capable of measuring frequency and dissipation variations in real time. A frequency decrease proves the adsorption of the polyelectrolyte and so, the construction of the multilayer film [108]. The dissipation factor is useful to investigate the viscoelastic properties of the built multilayer film [108]. The QCM-D data presented here in figures 67 – 71 correspond only to the successful experiments. Nevertheless, a short discussion of the possible reasons for not achieving a successful film production in some of the experiments is also presented, before the discussion of the data of figures 67 – 71.

For all the experiments, successful or unsuccessful, every solution containing CHT or ALG was adjusted to pH 5.5 as this is a pH value above ALG pKa and below CHT pKa, as already discussed in section 2.4. This is a commonly reported value in the literature for LbL assemblies of natural polymers based multilayer films [109], [125]. Many studies have reported the use of PE in a concentration of 0.5 mg/ml [109], [125], [126], and this was also the typical concentration adopted in the present experiments.

A build-up consisting on alternating deposition of a PC of f-GFs ethanolic solution and a PA of an ALG aqueous solution was tried using a PE concentration of 0.5 mg/ml and a pH 5.5 for ALG. As in a normal LbL procedure, between the adsorption of each PE there was washing steps that besides of removing weakly adsorbed PE, also aimed to stabilize the assembly being produced, since two different solvents - DW and ethanol – were used in the same assembly. Thus, right after the deposition of ALG, DW was feed to the QCM for 2.5 minutes followed by 2.5 minutes of ethanol, while after the deposition of f-GFs ethanolic solution, ethanol for 2.5 minutes followed by DW for 2.5 minutes were feed to the QCM, in order to stabilize the film to receive the next layer. A frequency decrease was recorded for the first bilayer deposition, but some peaks/fluctuations on frequency and dissipation were observed when the other solution/solvent was feed to the QCM-D. In the follow layers there were abrupt frequency decreases, followed by abrupt frequency increases to the same frequency level. Probably in this experiment, a first layer of f-GFs might not have been homogeneously deposited, which consequently might have hampered the deposition of a consistent CHT layer, preventing the assembling of the next layers. Therefore, a second attempt was made by depositing two bilayers of CHT and ALG, to serve as a support for f-GFs deposition, followed by f-GFs and ALG bilayers.

As expected, a frequency decrease and dissipation increase was verified for the 2 bilayers of CHT/ALG. However, every time that f-GFs and ALG solutions were deposited there were peaks/fluctuations on frequency and dissipation. Yet, frequency decreased with ALG deposition, after f-GFs deposition, which may indicate that some graphene was still there and so ALG could be adsorbed.

The use of different conditions (pH and solvent - ethanol as the solvent of f-GFs and DW as the solvent of ALG) in the different PE might be an issue in the LbL online QCM-D experiments, once it may induce disturbances in the recorded values. Thus, the experiment mentioned above was

tried in an offline approach. However, this experiment has also failed, since it was not verified a gradual frequency decrease in the f-GFs/ALG deposition.

The deposition time was different for the previous experiments, as it was decreased at each experiment, since after some time of deposition, the frequency did not continue to decrease and a frequency level was always reached, indicating that PE was neither adsorbed nor removed, once the frequency level was achieved.

This dissertation comes in a continuation of a previous work under the scope of the Individual Project, where the dispersion of f-GNRs in aqueous media turned out to be a problem. Thus, the solvent (ethanol) of the obtained solutions was completely evaporated and it was added DW. To dissolve the f-GNRs in DW, it was used ultrasounds intercalated by magnetic stirring aided by temperature, but f-GNRs revealed to be water-insoluble. Therefore, to overcome this problem and to avoid using different solvents in the QCM-D experiments, f-GNRs and natural polymers were dispersed in mixtures of ethanol and DW.

A f-GNRs solution of with a concentration of 0.5 mg/ml in 50% ethanol and 50% DW (f-GNRs-50) was prepared and assembled with an ELP solution, as it turned out to have a low and negative charge. ELP was dissolved in 50% ethanol and 50% DW, as well, with a concentration of 0.5 mg/ml and pH 5.5. As the deposition of graphene revealed to be most sensitive issue in the previous experiments, the f-GNRs was feed to the QCM with a slower flow, 25 µl/min, and longer time, 20 minutes, than ELP solution. The same build-up was also unsuccessfully tried with an f-GFs solution (f-GFs-50), since there was no frequency decrease when graphene was being feed, after deposition of ELP solution.

Regarding the successful experiments, some different conditions that were tried led to the formation of films (figures 68, 70 and 71). For example, a solution of f-GNRs and ALG in 25% ethanol and 75% DW was prepared in a concentration of 0.5 mg/ml and alternatively deposited with a 0.5 mg/ml concentrated CHT solution in 25% ethanol and 75% DW and 1% (v/v) acetic acid. Each PE was successfully assembled in 9-layer build-up to form the (CHT/f-GNRs-ALG)4.5 multilayer film. A (CHT/f-GFs-ALG)4.5 multilayer film was also assembled by repeating this procedure with a f-GFs solution. A CHT/ALG control multilayer film, (CHT/ALG)4.5, was built for comparison and its raw QCM-D data is presented in figure 67 as an example.
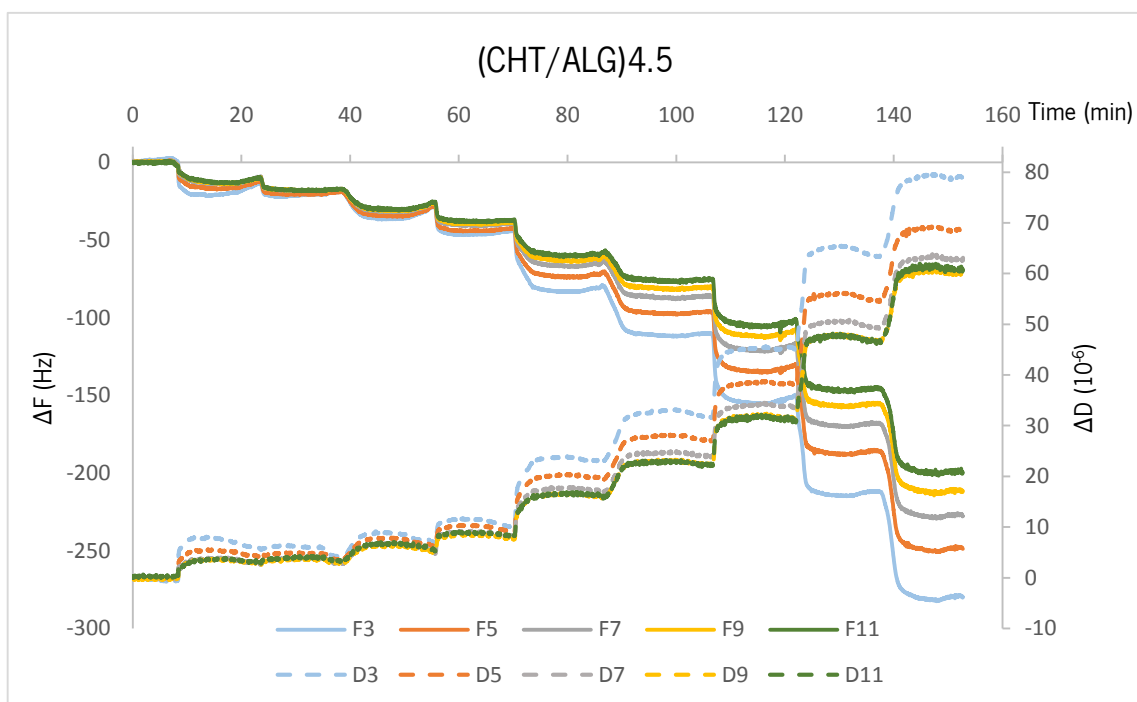
Figure 67: QCM-D raw data of frequency and dissipation factor variations for 5 overtones: 3rd, 5th, 7th, 9th and 11th, of the control multilayer film (CHT/ALG)4.5

It should be noted that a frequency increase may be observed at washing steps, between polyelectrolytes adsorption, due to some polyelectrolyte particles/molecules removal that were not strongly bonded to the particles/molecules underneath. But if the extent of the frequency increase during washing is not equal or higher than the frequency decrease in the previous polyelectrolyte deposition, it means that some particles/molecules remained bonded and the multilayer build-up still works.

For easy reading of the graphs, frequency and dissipation values of one overtone (7th overtone) after washing of each polyelectrolyte (values related to the final bonded mass of the respective layer) were taken from the QCM-D raw data. Frequency variations are plotted in terms of normalized frequency ($\Delta f/\upsilon$) and together with dissipation variations, they are plotted next as a function of the layers number for the assembled films, described on section 3.4. The indication of the natural polymer layers can be also found in these graphs, wherein those not marked layers correspond to graphene containing layers.

Figure 68 presents normalized frequency and dissipation variations as a function of the layer number of the multilayer films (CHT/f-GNRs-ALG)4.5, (CHT/f-GFs-ALG)4.5 and a control multilayer film (CHT/ALG)4.5. The deposition of the polycation, CHT, is highlighted in the x-axis. The

polyanions were a mixture of f-GNRs and ALG, f-GNRs-ALG, a mixture of f-GFs and ALG, f-GFs-ALG, and ALG to produce a control multilayer film.
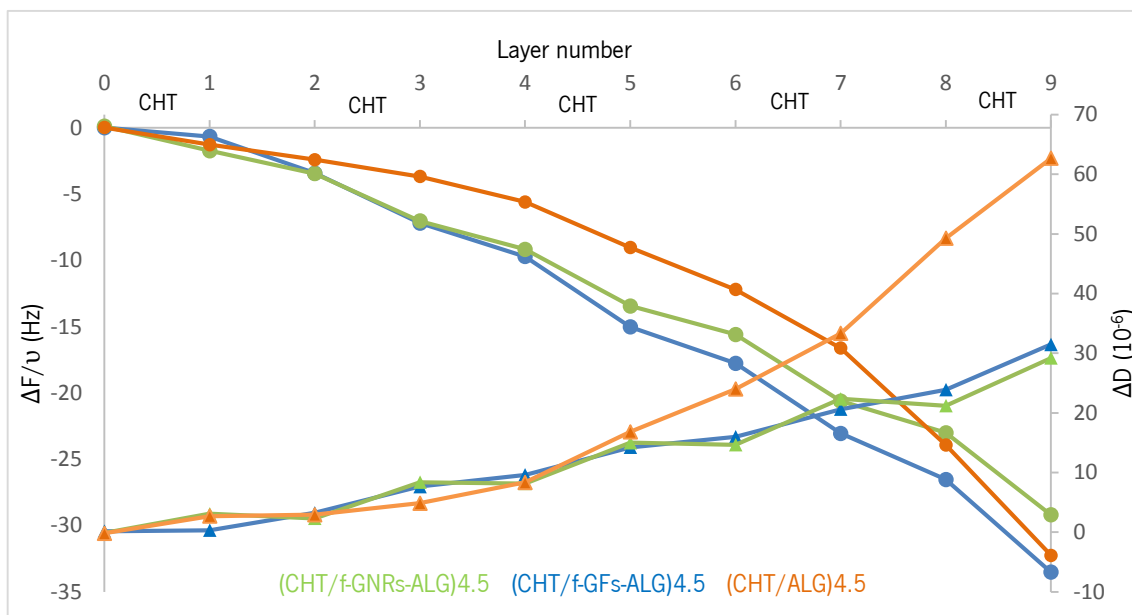
Figure 68: Normalized frequency (circles) and dissipation (triangles) variations as a function of the layer number of (CHT/f-GNRs-ALG)4.5, (CHT/f-GFs-ALG)4.5 and (CHT/ALG)4.5 multilayer films. CHT deposition is indicated in the x-axis

(CHT/f-GFs-ALG)4.5 multilayer film presents the higher frequency variation, followed by the (CHT/ALG)4.5 control and then (CHT/f-GNRs-ALG)4.5. Nevertheless, one can notice a similar overall frequency variation among the three multilayer films.

Regarding to dissipation variation, (CHT/ALG)4.5 control film presents considerably higher dissipation variation than the graphene based multilayer films, (CHT/f-GFs-ALG)4.5 and (CHT/f-GNRs-ALG)4.5.

It is also observable that both frequency and dissipation variations of the multilayer films containing graphene are similar, since normalized frequency and dissipation lines follow approximately the same slope at each deposited layer. (CHT/ALG)4.5 presents a slower frequency variation for the first layers than those graphene based films but it rapidly increases for the last layers.

The increase of dissipation in (CHT/ALG)4.5 is a consequence of the viscoelastic properties of this natural polymer based multilayer film. However, the dissipation increase is not so evident in the (CHT/f-GNRs-ALG)4.5 and (CHT/f-GFs-ALG)4.5. As can be seen in more detail in figure 69, every time the mixture f-GNRs-ALG or f-GFs-ALG are deposited there is not such a big ΔD increase as when ALG is deposited in the control film, and it may even decrease.
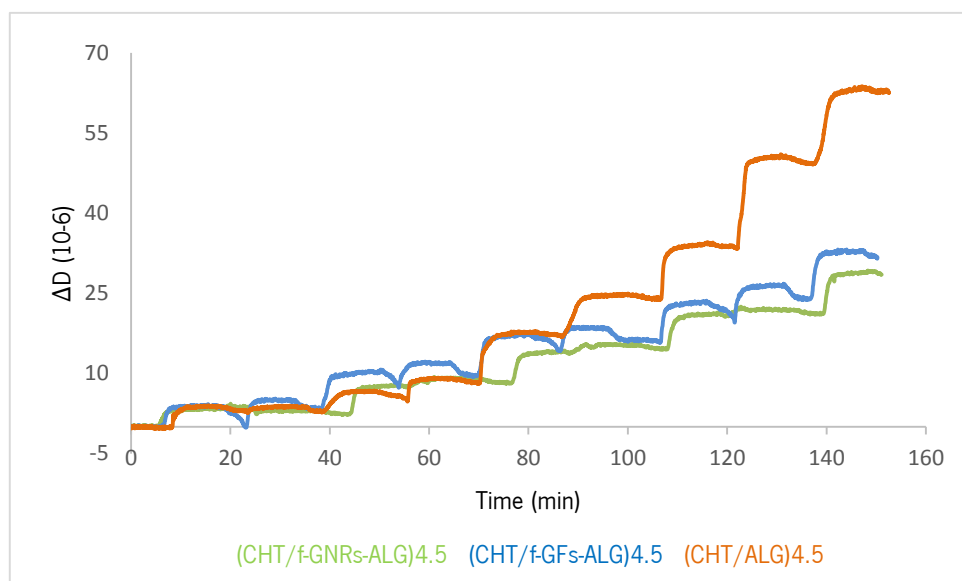
Figure 69: Dissipation variations as a function of time for the multilayer films (CHT/f-GNRs-ALG)4.5, (CHT/f-GFs-ALG)4.5 and (CHT/ALG)4.5.

These results might be an indication of thinner, more rigid and less water rich films [109], regarding to the graphene based films, which can be verified in the next section, once higher shear modulus and smaller thickness were the result of the modeling using the Voigt based model. Furthermore, it indicates that f-GNRs and f-GFs are bonded to the previous layer and not only ALG of the mixture f-GNRs-ALG.

Figure 70 shows the frequency and dissipation variation with Met. CHT polycation deposition, soluble at pH 7, and o-GNRs and o-GFs polyanions, to form the multilayer films (Met. CHT/o-GNRs)3 and (Met. CHT/o-GFs)2.
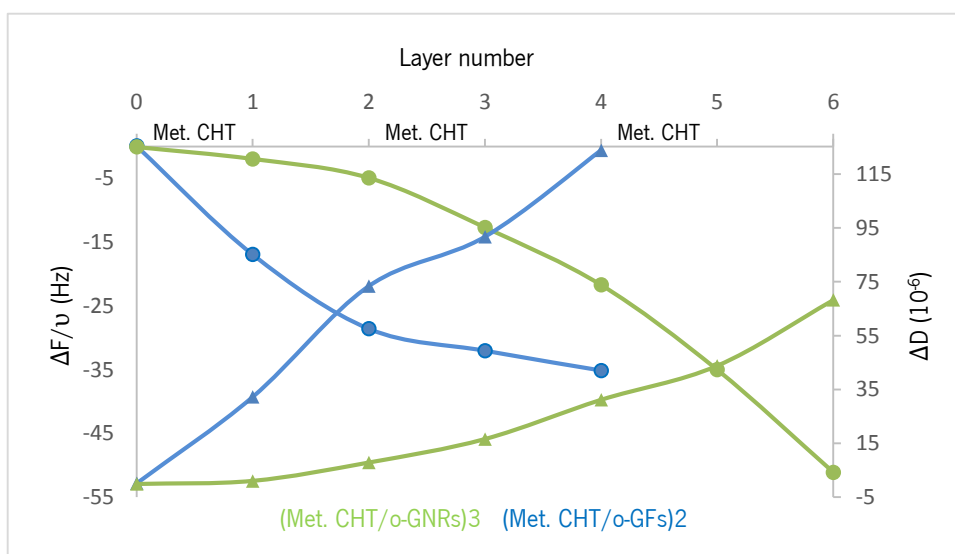
Figure 70: Normalized frequency (circles) and dissipation (triangles) variations as a function of the layer number of the multilayer films (Met. CHT/o-GNRs)3 and (Met. CHT/o-GFs)2. Met. The 3 polyelectrolytes aqueous solutions were in a concentration of 0.5 mg/ml. CHT deposition is indicated in the x-axis

The frequency decreases in figure 70 prove the success of these multilayer films made of alternate layers of Met. CHT and o-GNRs and Met. CHT and o-GFs. By comparing these films at the end of the second bilayer of (Met. CHT/o-GNRs)3, (Met.CHT/o-GFs)2 presents higher frequency variation than (Met. CHT/o-GNRs)3, indicating higher amount of mass bonded to the crystal surface and therefore, a thicker film. Higher ΔD is also observable for (Met.CHT/o-GFs)2 whether at the end of the second or third bilayer of (Met. CHT/o-GNRs)3.

It is also possible to notice that the frequency decrease for the first layer, corresponding to Met. CHT, are already quite different in these experiments, which might indicate some instability in one of the sensors. The frequency decrease is also more significant for o-GFs than for o-GNRs deposition.

Frequency and dissipation variations as a function of layer number of multilayer films constructed by alternate layers of CHT polycation and o-GNRs and o-GFs polyanions are presented in figure 71.
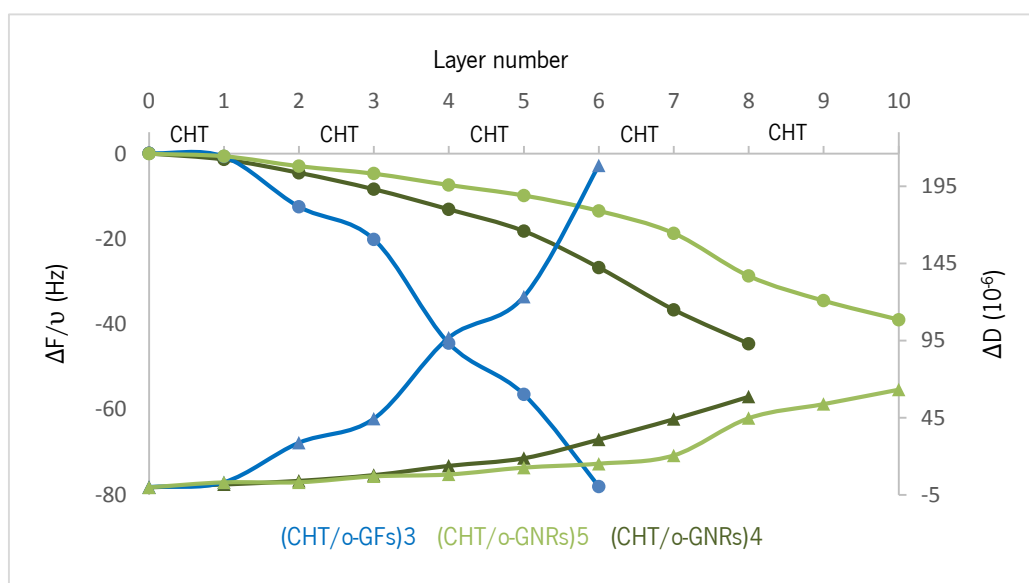
Figure 71: Normalized frequency (circles) and dissipation (triangles) variations as a function of the layer number of (CHT/o-GFs)3, (CHT/o-GNRs)5 and (CHT/o-GNRs)4 multilayer films. The multilayer films (CHT/o-GFs)3 and (CHT/o-GNRs)5 used o-GFs and o-GNRs solutions, respectively, with a concentration of 0.25 mg/ml and the multilayer film (CHT/o-GNRs)4 used o-GNRs solution with a concentration of 0.5 mg/ml. CHT was dissolved in a concentration of 0.5 mg/ml and pH 5.5. CHT layers are indicated in the x-axis

Once again, the frequency decrease prove the successful assemble of multilayer films of CHT with o-GNRs and o-GFs, even at lower solution concentration, 0.25 mg/ml in comparison with 0.5 mg/ml, and at a pH 5.5.

(CHT/o-GNRs)4 presents a higher frequency decrease than (CHT/o-GNRs)5, even though (CHT/o-GNRs)4 presents one less bilayer than (CHT/o-GNRs)5, but (CHT/o-GNRs)4 used the higher o-GNRs solution concentration. One can observe that frequency decrease due to CHT deposition is approximately in the same magnitude for both (CHT/o-GNRs)4 and (CHT/o-GNRs)5 but higher frequency decreases were recorded for 0.5 mg/ml concentrated o-GNRs solution deposition in (CHT/o-GNRs)4 than for 0.25 mg/ml concentrated o-GNRs solution deposition in (CHT/o-GNRs)5.

(CHT/o-GFs)3 presents the lower layer number of those multilayer films presented in figure 71, but the highest overall frequency decrease and dissipation increase were recorded for this film, though it used a 0.25 mg/ml concentrated o-GFs solution. Consequently and as expected, higher shear modulus and smaller thicknesses were modeled for (CHT/o-GNRs)4 and (CHT/o-GNRs)5, as presented in section 4.3.

Summarizing the QCM-D results, it can be said that in general graphene obtained from EG, whether from its oxidation or cycloaddition functionalization, produced multilayer films that presented higher frequency variations and therefore, thicker films may be obtained with GFs, when compared to similar f-GNRs containing multilayer films.

4.3. Multilayer films modeling

Three different overtones of Δf and ΔD were used to estimate the thickness and viscoelastic properties, namely shear modulus and viscosity, of the films assembled, using a Voigt based model with resort to the QTools software.

To model the multilayer films QCM-D data, solution density, ρ_s, solution viscosity, η_s, and density of the adsorbed film, ρ_L, values were changed in the QTools software, to get the lowest possible Total ChiSqr value. Those parameters and Total ChiSqr value are presented in table 7.

Table 7: Solution density and viscosity and density of the adsorbed film values used in the modeling of the multilayer films produced and resultant Total ChiSqr

Multilayer film	ρ_s (kg/m³)	η_s (Pa.s)	ρ_L (kg/m³)	Total ChiSqr
(CHT/f-GNRs-ALG)5	1021	0.001	1320	1.9442E5
(CHT/f-GFs-ALG)4.5	1109	0.0009	1252	82967
(CHT/ALG)5	1032	0.0009	1250	8.7294E5
(Met. CHT/o-GNRs)3	1100	0.001	1340	5.1166E6
(Met. CHT/o-GFs)2	1000	0.0006	1292	3.235E6
(CHT/o-GNRs)4	1004	0.0011	1250	3.6242E6
(CHT/o-GNRs)5	1035	0.001	1258	4.7181E6
(CHT/o-GFs)3	839	0.0013	1265	4.8005E5

Figure 72 presents modelled cumulative Viscosity (a), Shear Modulus (b) and Thickness (c) as a function of the layer number for (CHT/f-GNRs-ALG)4.5, (CHT/f-GFs-ALG)4.5 and (CHT/ALG)4.5 multilayer films.
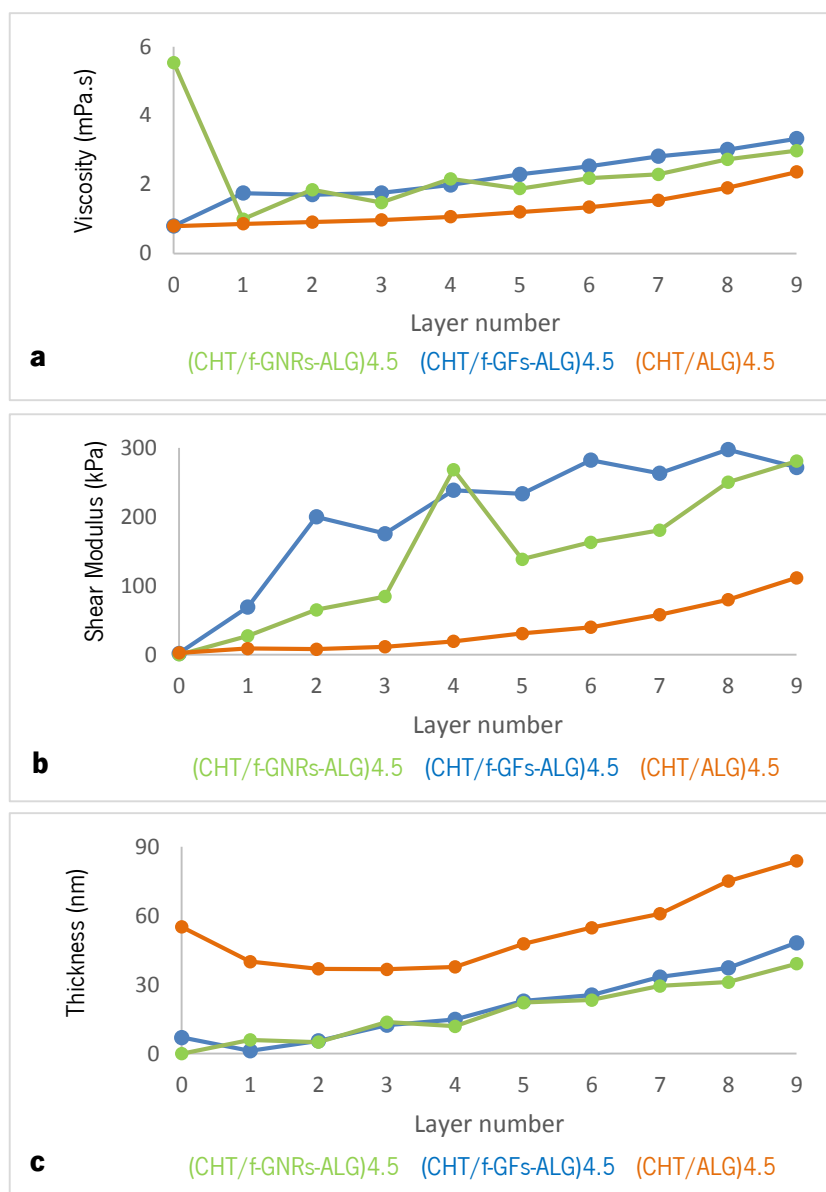
Figure 72: Modelled cumulative **(a)** Viscosity, **(b)** Shear Modulus and **(c)** Thickness as a function of the layer number for (CHT/f-GNRs-ALG)4.5, (CHT/f-GFs-ALG)4.5 and (CHT/ALG)4.5 multilayer films, using a Voigt based model

As expected, by analyzing Δf and ΔD curves in section 4.2, the (CHT/f-GFs-ALG)4.5 presents higher thickness than (CHT/f-GNRs-ALG)4.5. However, (CHT/ALG)4.5 natural polymer control multilayer film presents considerably higher thickness than the graphene based multilayer films.

Mainly for (CHT/ALG)4.5 and (CHT/f-GFs-ALG)4.5, is possible to notice a thickness decrease for the first layers assembled, which might be a cause of compression or dehydration phenomena, but then, it normally increases. In the case of (CHT/f-GNRs-ALG)4.5, the increase of thickness is not so well notice when f-GNRs-ALG solution is injected and it happened to decrease at some layers.

It was found that (CHT/ALG)4.5 presents a final thickness of approximately 84 nm, while (CHT/f-GFs-ALG)4.5 and (CHT/f-GNRs-ALG)4.5 present a final thickness of 48 and 39 nm, respectively.

Generally, the shear modulus tends to increase with the layer number, but some fluctuations are visible. (CHT/f-GFs-ALG)4.5 and (CHT/f-GNRs-ALG)4.5 present similar final shear modulus, 272 and 281 kPa, respectively while (CHT/ALG)4.5 presents a final shear modulus of 112 kPa. At some extent, this modeling allowed to verify that graphene may improve the mechanical properties of the multilayer films made of natural polymers, (CHT/ALG)4.5, but a higher number of layers is required to get a specified thickness, when compared to the (CHT/ALG)4.5 multilayer film.

In general, there was an increase in the modeled viscosity to approximatly 3 mPa.s for the three containing CHT and ALG multilayer films.

Modelled cumulative Viscosity (a), Shear Modulus (b) and Thickness (c) curves, as a function of the layer number, for (Met. CHT/o-GNRs)3 and (Met. CHT/o-GFs)2 multilayer films are presented in figure 73.
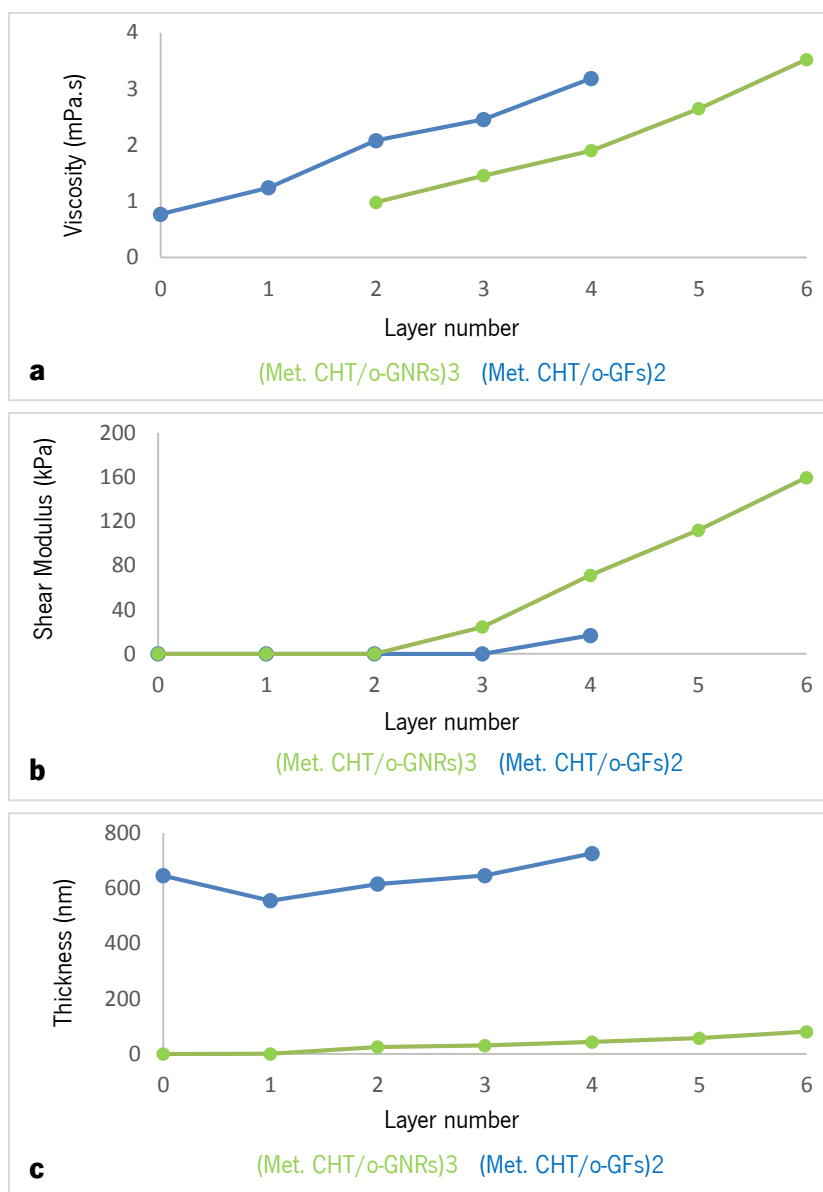
Figure 73: Modelled cumulative **(a)** Viscosity, **(b)** Shear Modulus and **(c)** Thickness as a function of the layer number for (Met. CHT/o-GNRs)3 and (Met. CHT/o-GFs)2 multilayer films, using a Voigt based model

A huge difference in thickness was modeled for (Met. CHT/o-GNRs)3 and (Met. CHT/o-GFs)2 multilayer films, the first measuring around 81 nm and the last around 726 nm, although (Met. CHT/o-GFs)2 has one less layer. At the end of the second layer (Met. CHT/o-GNRs)3 presents a thickness of 43 nm. Similarly to (CHT/ALG)4.5 and (CHT/f-GFs-ALG)4.5, (Met. CHT/o-GFs)2 experienced a decrease of thickness in the first layer. One can also notice that the biggest thickness increase happens right in the first layer, ~ 645 nm, and it reached a maximum thickness of ~ 726 nm in the end of the second bilayer.

Shear modulus of (Met. CHT/o-GNRs)3 and (Met. CHT/o-GFs)2 increased with the layer number, up to 159 and 17 kPa, respectively. (Met. CHT/o-GNRs)3 seems to present better mechanical

properties than (Met. CHT/o-GFs)2, since it was modeled a shear modulus of 71 kPa at the end of the second bilayer of (Met. CHT/o-GNRs)3.

Likewise figure 72 (a), the viscosity of (Met. CHT/o-GNRs)3 and (Met. CHT/o-GFs)2 multilayer films increases to a maximum of about 3 mPa.s. Viscosity values are not presented until the second layer of (Met. CHT/o-GNRs)3 since huge variations were modeled for these steps.

Figure 74 presents modelled cumulative Viscosity (a), Shear Modulus (b) and Thickness (c) curves, as a function of the layer number, for (CHT/o-GFs)3, (CHT/o-GNRs)5, and (CHT/o-GNRs)4 multilayer films.
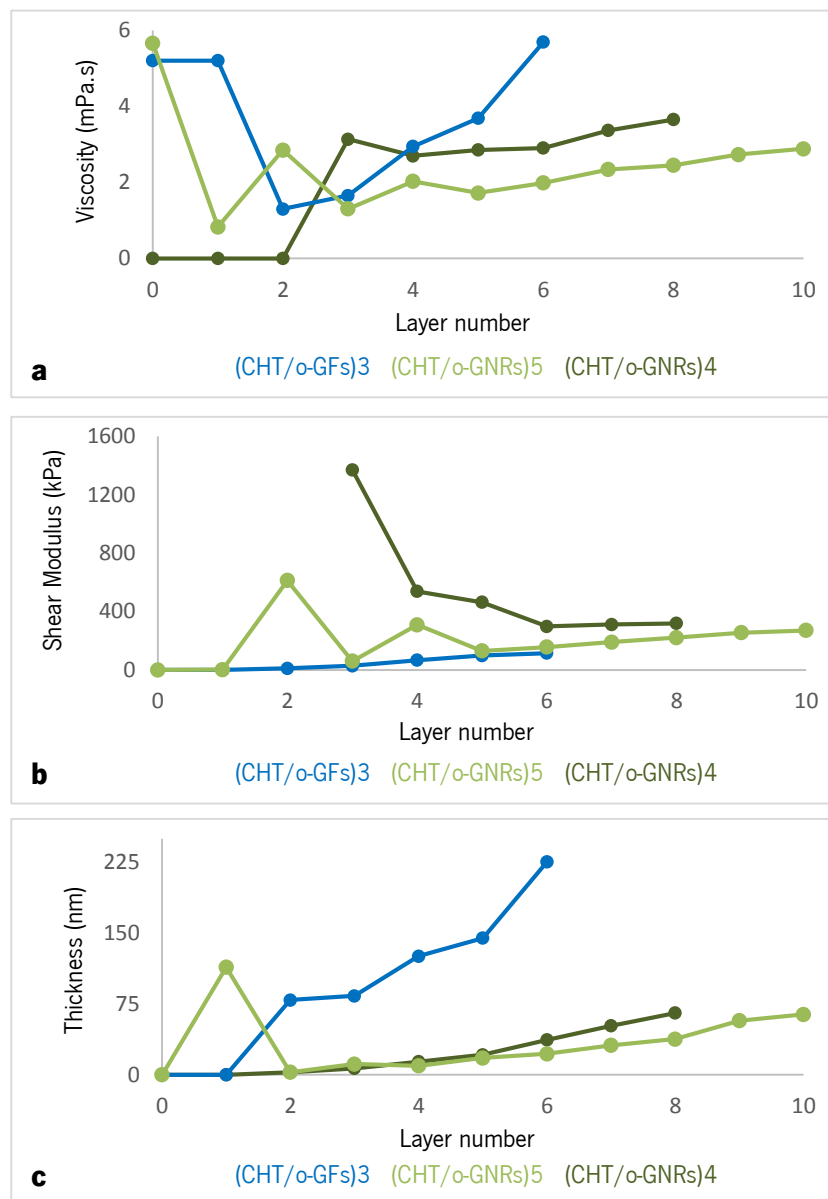
Figure 74: Modelled cumulative Viscosity **(a)**, Shear Modulus **(b)** and Thickness **(c)** as a function of the layer number for (CHT/o-GFs)3, (CHT/o-GNRs)5, and (CHT/o-GNRs)4 multilayer films, using a Voigt based model

Once again, the o-GFs containing multilayer film, (CHT/o-GFs)3, revealed to be thicker than o-GNRs containing multilayer films, (CHT/o-GNRs)5 and (CHT/o-GNRs)4, even with less bilayers assembled, 3 bilayers against 4 and 5 bilayers. At the end of the third bilayer a thickness of 225, 37, and 22 nm for (CHT/o-GFs)3, (CHT/o-GNRs)4 and (CHT/o-GNRs)5, respectively.

o-GFs containing multilayer film also presented a lower shear modulus than o-GNRs containing multilayer films. Some fluctuations are observed in the shear modulus of (CHT/o-GNRs)5 and (CHT/o-GFs)3, which might be a cause of compression or dehydration phenomena, but they all generally increase to a value of the same order of magnitude.

After stabilization of likely compression or dehydration phenomena, as soon as the film gets stable, the increase of the thickness tend to be generally linear. This behavior was also reported for CHT/ALG multilayer films and is explained by the incapability of the PE to diffuse 'in' and 'out' of the film after its deposition step [125]. By other side, an exponential growth may be explained by the ability of the PE to diffuse 'in' and 'out' at each bilayer deposition or by the increase of the fil surface roughness as the film build-up progresses [109].

Table 8 summarizes the final shear modulus and thicknesses of the multilayer films produced.

Table 8: Summary of the multilayer films thickness and shear modulus

Multilayer film	Thickness (nm)	Shear Modulus (kPa)
(CHT/f-GNRs-ALG)4.5	39	281
(CHT/f-GFs-ALG)4.5	48	272
(CHT/ALG)4.5	84	112
(Met. CHT/o-GNRs)3	81	159
(Met. CHT/o-GFs)2	726	17
(CHT/o-GNRs)4	65	318
(CHT/o-GNRs)5	64	270
(CHT/o-GFs)3	225	115

In general, GNRs (both f-GNRs and o-GNRs) containing multilayer films present higher final shear modulus than GFs containing multilayer films, even at the end of same layer number for a similar

GFs containing multilayer film. The f-GNRs-ALG and f-GFs-ALG mixtures also gave rise to multilayer films with higher shear modulus, when compared to o-GNRs and o-GFs containing multilayer films, which might be explained by the lower amount of functional groups of functionalized graphene and consequent better mechanical properties.

GFs containing multilayer film are much thicker than GNRs containing multilayer films even with smaller number of bilayers assembled.

Regarding to the STEM images of graphene, it seems that the o-GNRs 'network' organization leads to more compact multilayer films, while the large dimensions of f-GFs and o-GFs leads to thicker multilayer films assembly.

It should be noticed that those modeled values regarding to oxidized graphene based multilayer films are a bit more far from the real values than those values modeled for functionalized graphene based multilayer films and the control CHT and ALG multilayer film, as oxidized graphene based multilayer films generally presented higher Total ChiSqr values.

Conclusions

Four different types of graphene were successfully produced in solution by application of different chemical methods and ultrasounds on MWNTs and EG. A functionalization consisting on a 1,3-dipolar cycloaddition reaction produced functionalized GNRs and GFs (f-GNRs and f-GFs) with protected amine and pyrrolidine functional groups.

A modified Hummers' method, using H_2SO_4 and $KMnO_4$, was applied to EG to obtain oxidized GFs (o-GFs), and a method proposed by Kosynkin and coworkers was applied to MWNTs to produce oxidized GNRs (o-GNRs), therefore o-GNRs and o-GFs contain covalently bonded oxygen containing functional groups.

UV-Vis spectroscopy revealed the efficiency of the methods used. High concentrations of oxidized GNRs and GFs were obtained in solution, 0.906 and 0.319 mg/ml, respectively. These concentrations are approximately one order of magnitude larger than those obtained for functionalized GNRs and GFs (0.031 and 0.051 mg/ml, respectively).

IR spectroscopy showed the general chemical nature of the functional groups bonded to the GNRs and GFs. TGA experiments also proved the success of the functionalization and oxidation reaction, they were helpful to quantify the degree of functionalization and to evaluate the thermal resistance properties of the graphene produced. The overall weight loss was 83.9% for f-GNRs, 87.7 % for f-GFs, 41.1% for o-GNRs and 20.0% for o-GFs.

STEM was used to evaluate graphene distribution and morphology for subsequent STM studies. Functionalized GNRs revealed to be flat and well dispersed and therefore, they were further analyzed by STM, for atomic and electronic characterization. OM and AFM were valuable techniques to study and validate sample preparation.

STM analysis was done in three different conditions, air-STM, UHV- STM and LT- STM. The air-STM was very important to understand the distribution and morphology of GNRs, for later studies in UHV-STM and LT-STM. Additionally, the air-STM was convenient for understanding the STM principles and fundamentals in a user perspective.

The air-STM allowed to scan f-GNRs edges and atomically resolved images were obtained, nevertheless it was not possible to distinguish layers in a multilayer GNR. In the UHV-STM a 1 μm long and 140 nm wide GNR was imaged, which revealed Moiré pattern on the top layer, with a periodicity of approximately 36 Å. Resorting to STS, using a LT-STM, the electronic properties were studied, within some limitations, since tip instabilities were noticed. A 70 nm wide GNR presented

higher differential conductance at its edges, possibly due to the presence of protruding functional groups at these sites.

All different types of graphene solutions produced were successfully assembled with alternate layers of natural polymers, CHT and Met. CHT, in an LbL approach and real-time monitored by a QCM-D, to produce multilayer films.

Oxidized GNRs and GFs were alternatively deposited with CHT and Met. CHT, while functionalized GNRs and GFs were mixed with the ALG natural polymer and alternatively deposited with CHT. A control multilayer film for functionalized graphene containing multilayer films was also produced by alternating layers of ALG and CHT. The resultant multilayer films were (CHT/f-GNRs-ALG)4.5, (CHT/f-GFs-ALG)4.5, (CHT/ALG)4.5, (Met. CHT/o-GNRs)3, (Met. CHT/o-GFs)2, (CHT/o-GNRs)4, (CHT/o-GNRs)5 and (CHT/o-GFs)3.

Modelling approaches using a Voigt based model were helpful to evaluate multilayer films thicknesses and shear modulus. Generally, multilayer films containing f-GNRs and o-GNRs present higher final shear modulus than GFs, even at the end of the same layer number for a similar GFs containing multilayer film. GFs originate much thicker multilayer films than GNRs. Functionalized graphene also produced multilayer films with higher shear modulus.

These multilayer films may find application in the biomedical area.

Future Perspectives

The validation of these films to be used in biomedical applications will require the production of free-standing micrometer multilayer films, in order to characterize their mechanical, electrical, electrochemical, topographic and biological properties. The use of the multilayer films in regenerative medicine of electrically conducting tissues or devices may be possible by favorable electrical properties, which could be evaluated by the Four Probe Method.

Dynamic Mechanical Analysis, DMA, and tensile tests may be useful for mechanical characterization, AFM for topographic characterization and SEM for thickness measurement of the multilayer films and morphology studies. Regarding the biological response, standard cell adhesion, proliferation and viability tests should be conducted.

The validation of the multilayer films, that may find application as sensors, would require electrochemical characterization, which could be performed by cyclic voltammetry, CV, in order to evaluate the electrocatalytic activity of the films towards the analytes.

,

References

[1]   S. G. Kumbar, C. T. Laurencin, and M. Deng, *Natural and Synthetic Biomedical Polymers*, 1st ed. United States of America: Elsevier, 2014.

[2]   T. Kuila, S. Bose, P. Khanra, A. K. Mishra, N. H. Kim, and J. H. Lee, "Recent advances in graphene-based biosensors.," *Biosens. Bioelectron.*, vol. 26, no. 12, pp. 4637–48, Aug. 2011.

[3]   Y. Shao, J. Wang, H. Wu, J. Liu, I. A. Aksay, and Y. Lin, "Graphene Based Electrochemical Sensors and Biosensors: A Review," *Electroanalysis*, vol. 22, no. 10, pp. 1027–1036, May 2010.

[4]   M. H. Chakrabarti, C. T. J. Low, N. P. Brandon, V. Yufit, M. A. Hashim, M. F. Irfan, J. Akhtar, E. Ruiz-Trejo, and M. A. Hussain, "Progress in the electrochemical modification of graphene-based materials and their applications," *Electrochim. Acta*, vol. 107, pp. 425–440, Sep. 2013.

[5]   M. Terrones, A. R. Botello-Méndez, J. Campos-Delgado, F. López-Urías, Y. I. Vega-Cantú, F. J. Rodríguez-Macías, A. L. Elías, E. Muñoz-Sandoval, A. G. Cano-Márquez, and J.-C. Charlier, "Graphene and graphite nanoribbons: Morphology, properties, synthesis, defects and applications," *Nano Today*, vol. 5, no. 4, pp. 351–372, Aug. 2010.

[6]   K. S. Novoselov, V. I. Fal'ko, L. Colombo, P. R. Gellert, M. G. Schwab, and K. Kim, "A roadmap for graphene," *Nature*, vol. 490, no. 7419, pp. 192–200, Oct. 2012.

[7]   Y. Zhu, S. Murali, W. Cai, X. Li, J. W. Suk, J. R. Potts, and R. S. Ruoff, "Graphene and graphene oxide: synthesis, properties, and applications.," *Adv. Mater.*, vol. 22, no. 35, pp. 3906–24, Sep. 2010.

[8]   J. N. Coleman, U. Khan, W. J. Blau, and Y. K. Gun'ko, "Small but strong: A review of the mechanical properties of carbon nanotube–polymer composites," *Carbon N. Y.*, vol. 44, no. 9, pp. 1624–1652, Aug. 2006.

[9]   "Immunopathologie et Chimie Thérapeutique - CNRS-UPR3572 - Carbon nanotubes." [Online]. Available: http://www-ibmc.u-strasbg.fr/ict/article83.html?lang=en.

[10]   K.-W. Ng, W.-H. Lam, and S. Pichiah, "A review on potential applications of carbon nanotubes in marine current turbines," *Renew. Sustain. Energy Rev.*, vol. 28, pp. 331–339, Dec. 2013.

[11]   S. H. Kim, G. W. Mulholland, and M. R. Zachariah, "Density measurement of size selected multiwalled carbon nanotubes by mobility-mass characterization," *Carbon N. Y.*, vol. 47, no. 5, pp. 1297–1302, 2009.

[12]   N. Ooi, A. Rairkar, and J. B. Adams, "Density functional study of graphite bulk and surface properties," *Carbon N. Y.*, vol. 44, no. 2, pp. 231–242, Feb. 2006.

[13]   R. Sanjinés, M. D. Abad, C. Vâju, R. Smajda, M. Mionić, and A. Magrez, "Electrical properties and applications of carbon based nanocomposite materials: An overview," *Surf. Coatings Technol.*, vol. 206, no. 4, pp. 727–733, Nov. 2011.

[14]   H. Shioyama, "The interactions of two chemical species in the interlayer spacing of graphite," *Synth. Met.*, vol. 114, no. 1, pp. 1–15, Jul. 2000.

[15]   "Ultrafast science: Ultrafast science at the MAX BORN INSTITUTE for Nonlinear Optics and Short Pulse Spectroskopy - Highlight." [Online]. Available: http://www.mbi-berlin.de/en/research/highlights/highlight_graphite.html.

[16]   K. Sever, İ. H. Tavman, Y. Seki, A. Turgut, M. Omastova, and I. Ozdemir, "Electrical and mechanical properties of expanded graphite/high density polyethylene nanocomposites," *Compos. Part B Eng.*, vol. 53, pp. 226–233, Oct. 2013.

[17]   Y. Zhao, J. Shi, and H. Wang, "A sandwich structure graphite block with excellent thermal and mechanical properties reinforced by in-situ grown carbon nanotubes," *Carbon N. Y.*, vol. 1, pp. 5–8, 2012.

[18]   A. Elleuch, J. Yu, A. Boussetta, K. Halouani, and Y. Li, "Electrochemical oxidation of graphite in an intermediate temperature direct carbon fuel cell based on two-phases electrolyte," *Int. J. Hydrogen Energy*, vol. 38, no. 20, pp. 8514–8523, Jul. 2013.

[19]   P. Trinuruk and T. Obara, "Concept of prismatic high temperature gas-cooled reactor with SiC coating on graphite structures," *Ann. Nucl. Energy*, vol. 63, pp. 437–445, 2014.

[20]   H. Badenhorst, "Microstructure of natural graphite flakes revealed by oxidation: Limitations of XRD and Raman techniques for crystallinity estimates," *Carbon N. Y.*, vol. 66, pp. 674–690, Jan. 2014.

[21]   M. Bonnissel, L. Luo, and D. Tondeur, "Compacted exfoliated natural graphite as heat conduction medium," *Carbon N. Y.*, vol. 39, no. 14, pp. 2151–2161, Nov. 2001.

[22]   N. Sykam and K. K. Kar, "Rapid synthesis of exfoliated graphite by microwave irradiation and oil sorption studies," *Mater. Lett.*, vol. 117, pp. 150–152, Feb. 2014.

[23]   P.-H. Chen and D. D. L. Chung, "Thermal and electrical conduction in the compaction direction of exfoliated graphite and their relation to the structure," *Carbon N. Y.*, vol. 77, pp. 538–550, Oct. 2014.

[24]   J. H. Warner, F. Schaffel, M. Rummeli, and A. Bachmatiuk, *Graphene: Fundamentals and emergent applications*, 1st ed. United Kingdom: Elsevier Inc., 2013.

[25]   A. H. Castro Neto, N. M. R. Peres, K. S. Novoselov, and A. K. Geim, "The electronic properties of graphene," *Rev. Mod. Phys.*, vol. 81, no. 1, pp. 109–162, Jan. 2009.

[26]   H.-S. P. Wong and D. AKINWANDE, *Carbon Nanotube and Graphene Device Physics*, 1st ed. United Kingdom: Cambridge University Press, 2011.

[27]   V. Skálalová and A. Kaiser, "Graphene Properties, preparation, characterisation and devices," 1st ed., United Kingdom: Woodhead Publishing, 2014.

[28]   S. K. Choudhary and A. K. Gupta, "Scanning tunneling microscopy and spectroscopy study of charge inhomogeneities in bilayer graphene," *Solid State Commun.*, vol. 151, no. 5, pp. 396–399, Mar. 2011.

[29]   A. Kumar, S. Patil, A. Joshi, V. Bhoraskar, S. Datar, and P. Alegaonkar, "Mixed phase, sp2–sp3 bonded, and disordered few layer graphene-like nanocarbon: Synthesis and characterizations," *Appl. Surf. Sci.*, vol. 271, pp. 86–92, Apr. 2013.

[30]   K. N. Kudin, B. Ozbas, H. C. Schniepp, R. K. Prud'homme, I. A. Aksay, and R. Car, "Raman spectra of graphite oxide and functionalized graphene sheets.," *Nano Lett.*, vol. 8, no. 1, pp. 36–41, Jan. 2008.

[31]   A. Luican, G. Li, and E. Y. Andrei, "Scanning tunneling microscopy and spectroscopy of graphene layers on graphite," *Solid State Commun.*, vol. 149, no. 27–28, pp. 1151–1156, Jul. 2009.

[32] H. Ö. Doğan, D. Ekinci, and Ü. Demir, "Atomic scale imaging and spectroscopic characterization of electrochemically reduced graphene oxide," *Surf. Sci.*, vol. 611, pp. 54–59, May 2013.

[33] C. Tao, L. Jiao, O. V. Yazyev, Y.-C. Chen, J. Feng, X. Zhang, R. B. Capaz, J. M. Tour, A. Zettl, S. G. Louie, H. Dai, and M. F. Crommie, "Spatially resolving edge states of chiral graphene nanoribbons," *Nat. Phys.*, vol. 7, no. 8, pp. 616–620, May 2011.

[34] S. Hattendorf, A. Georgi, M. Liebmann, and M. Morgenstern, "Networks of ABA and ABC stacked graphene on mica observed by scanning tunneling microscopy," *Surf. Sci.*, vol. 610, pp. 53–58, Apr. 2013.

[35] D. Pandey, R. Reifenberger, and R. Piner, "Scanning probe microscopy study of exfoliated oxidized graphene sheets," *Surf. Sci.*, vol. 602, no. 9, pp. 1607–1613, May 2008.

[36] K. a Ritter and J. W. Lyding, "The influence of edge structure on the electronic properties of graphene quantum dots and nanoribbons.," *Nat. Mater.*, vol. 8, no. 3, pp. 235–42, Mar. 2009.

[37] L. Jiao, X. Wang, G. Diankov, H. Wang, and H. Dai, "Facile synthesis of high-quality graphene nanoribbons.," *Nat. Nanotechnol.*, vol. 5, no. 5, pp. 321–5, May 2010.

[38] A. K. Geim and K. S. Novoselov, "The rise of graphene," *Nat. Mater.*, vol. 6, no. 3, pp. 183–91, Mar. 2007.

[39] L. G. De Arco, Y. Zhang, and C. Zhou, "Large Scale Graphene by Chemical Vapor Deposition : Synthesis , Characterization and Applications," in *Graphene - Synthesis, Characterization, Properties and Applications*, C. De Arco, L.G., Zhang, Y., Zhou, Ed. United States of America: InTech, 2011.

[40] J. Bai and Y. Huang, "Fabrication and electrical properties of graphene nanoribbons," *Mater. Sci. Eng. R Reports*, vol. 70, no. 3–6, pp. 341–353, Nov. 2010.

[41] A. Nekahi, P. H. Marashi, and D. Haghshenas, "Transparent conductive thin film of ultra large reduced graphene oxide monolayers," *Appl. Surf. Sci.*, vol. 295, pp. 59–65, Mar. 2014.

[42] L. Gomez De Arco, Y. Zhang, C. W. Schlenker, K. Ryu, M. E. Thompson, and C. Zhou, "Continuous, highly flexible, and transparent graphene films by chemical vapor deposition for organic photovoltaics.," *ACS Nano*, vol. 4, no. 5, pp. 2865–73, May 2010.

[43] X. Shen, Y. Cui, Y. Pang, and H. Qian, "Graphene oxide nanoribbon and polyhedral oligomeric silsesquioxane assembled composite frameworks for pre-concentrating and electrochemical sensing of 1-hydroxypyrene," *Electrochim. Acta*, vol. 59, pp. 91–99, Jan. 2012.

[44] T. Premkumar and K. E. Geckeler, "Graphene–DNA hybrid materials: Assembly, applications, and prospects," *Prog. Polym. Sci.*, vol. 37, no. 4, pp. 515–529, Apr. 2012.

[45] A. Singh, G. Sinsinbar, M. Choudhary, V. Kumar, R. Pasricha, H. N. Verma, S. P. Singh, and K. Arora, "Graphene oxide-chitosan nanocomposite based electrochemical DNA biosensor for detection of typhoid," *Sensors Actuators B Chem.*, vol. 185, pp. 675–684, Aug. 2013.

[46]   T. Kuilla, S. Bhadra, D. Yao, N. H. Kim, S. Bose, and J. H. Lee, "Recent advances in graphene based polymer composites," *Prog. Polym. Sci.*, vol. 35, no. 11, pp. 1350–1375, Nov. 2010.

[47]   R. Hao, W. Qian, L. Zhang, and Y. Hou, "Aqueous dispersions of TCNQ-anion-stabilized graphene sheets.," *Chem. Commun. (Camb).*, no. 48, pp. 6576–8, Dec. 2008.

[48]   W.-W. Liu, S.-P. Chai, A. R. Mohamed, and U. Hashim, "Synthesis and characterization of graphene and carbon nanotubes: A review on the past and recent developments," *J. Ind. Eng. Chem.*, Sep. 2013.

[49]   M. C. Paiva, W. Xu, M. F. Proença, R. M. Novais, E. Laegsgaard, and F. Besenbacher, "Unzipping of functionalized multiwall carbon nanotubes induced by STM.," *Nano Lett.*, vol. 10, no. 5, pp. 1764–8, May 2010.

[50]   H. Aoki and M. S. Dresselhaus, *Physics of Graphene - NanoScience and Technology*, 1st ed. New York: Springer, 2014.

[51]   M. Pumera, "Electrochemistry of graphene, graphene oxide and other graphenoids: Review," *Electrochem. commun.*, vol. 36, pp. 14–18, Nov. 2013.

[52]   G. Wang, X. Sun, C. Liu, and J. Lian, "Tailoring oxidation degrees of graphene oxide by simple chemical reactions," *Appl. Phys. Lett.*, vol. 99, no. 5, p. 053114, 2011.

[53]   D. V Kosynkin, A. L. Higginbotham, A. Sinitskii, J. R. Lomeda, A. Dimiev, B. K. Price, and J. M. Tour, "Longitudinal unzipping of carbon nanotubes to form graphene nanoribbons.," *Nature*, vol. 458, no. 7240, pp. 872–6, Apr. 2009.

[54]   L. Jiao, L. Zhang, X. Wang, G. Diankov, and H. Dai, "Narrow graphene nanoribbons from carbon nanotubes.," *Nature*, vol. 458, no. 7240, pp. 877–80, Apr. 2009.

[55]   A. G. Cano-Márquez, F. J. Rodríguez-Macías, J. Campos-Delgado, C. G. Espinosa-González, F. Tristán-López, D. Ramírez-González, D. a Cullen, D. J. Smith, M. Terrones, and Y. I. Vega-Cantú, "Ex-MWNTs: graphene sheets and ribbons produced by lithium intercalation and exfoliation of carbon nanotubes.," *Nano Lett.*, vol. 9, no. 4, pp. 1527–33, Apr. 2009.

[56]   M. Vakili, M. Rafatullah, B. Salamatinia, A. Z. Abdullah, M. H. Ibrahim, K. B. Tan, Z. Gholami, and P. Amouzgar, "Application of chitosan and its derivatives as adsorbents for dye removal from water and wastewater: A review," *Carbohydr. Polym.*, vol. 113, pp. 115–130, Jul. 2014.

[57]   J. Kumirska, M. Czerwicka, Z. Kaczyński, A. Bychowska, K. Brzozowski, J. Thöming, and P. Stepnowski, "Application of spectroscopic methods for structural analysis of chitin and chitosan.," *Mar. Drugs*, vol. 8, no. 5, pp. 1567–636, Jan. 2010.

[58]   C. Pandis, S. Madeira, J. Matos, A. Kyritsis, J. F. Mano, and J. L. G. Ribelles, "Chitosan-silica hybrid porous membranes.," *Mater. Sci. Eng. C. Mater. Biol. Appl.*, vol. 42, pp. 553–61, Sep. 2014.

[59]   M. Dash, F. Chiellini, R. M. Ottenbrite, and E. Chiellini, "Chitosan—A versatile semi-synthetic polymer in biomedical applications," *Prog. Polym. Sci.*, vol. 36, no. 8, pp. 981–1014, Aug. 2011.

[60]   L. Wu, A. P. Gadre, H. Yi, M. J. Kastantin, G. W. Rubloff, W. E. Bentley, G. F. Payne, and R. Ghodssi, "Voltage-Dependent Assembly of the Polysaccharide Chitosan onto an Electrode Surface," no. 14, pp. 8620–8625, 2002.

[61]   R. R. Costa, A. M. Testera, F. J. Arias, J. C. Rodríguez-Cabello, and J. F. Mano, "Layer-by-layer film growth using polysaccharides and recombinant polypeptides: a combinatorial approach.," *J. Phys. Chem. B*, vol. 117, no. 22, pp. 6839–48, Jun. 2013.

[62]   L. M. Y. Yu, K. Kazazian, and M. S. Shoichet, "Peptide surface modification of methacrylamide chitosan for neural tissue engineering applications.," *J. Biomed. Mater. Res. A*, vol. 82, no. 1, pp. 243–55, Jul. 2007.

[63]   P. Agulhon, M. Robitzer, J.-P. Habas, and F. Quignard, "Influence of both cation and alginate nature on the rheological behavior of transition metal alginate gels," *Carbohydr. Polym.*, vol. 112, pp. 525–531, Nov. 2014.

[64]   A. D. Augst, H. J. Kong, and D. J. Mooney, "Alginate hydrogels as biomaterials.," *Macromol. Biosci.*, vol. 6, no. 8, pp. 623–33, Aug. 2006.

[65]   J. Jang, Y.-J. Seol, H. J. Kim, J. Kundu, S. W. Kim, and D.-W. Cho, "Effects of alginate hydrogel cross-linking density on mechanical and biological behaviors for tissue engineering.," *J. Mech. Behav. Biomed. Mater.*, vol. 37, pp. 69–77, Sep. 2014.

[66]   M. Alves, C. Picart, and F. Mano, "Self Assembling and Crosslinking of Polyelectrolyte Multilayer Films of Chitosan and Alginate Studied by QCM and IR Spectroscopy," *Macromol. Biosci*, vol. 9, pp. 776–785, 2009.

[67]   N. Kamalian, H. Mirhosseini, S. Mustafa, and M. Y. A. Manap, "Effect of alginate and chitosan on viability and release behavior of Bifidobacterium pseudocatenulatum G4 in simulated gastrointestinal fluid.," *Carbohydr. Polym.*, vol. 111, pp. 700–6, Oct. 2014.

[68]   D. S. Morais, M. A. Rodrigues, T. I. Silva, M. A. Lopes, M. Santos, J. D. Santos, and C. M. Botelho, "Development and characterization of novel alginate-based hydrogels as vehicles for bone substitutes.," *Carbohydr. Polym.*, vol. 95, no. 1, pp. 134–42, Jun. 2013.

[69]   A. Quinn, G. K. Such, J. F. Quinn, and F. Caruso, "Polyelectrolyte Blend Multilayers: A Versatile Route to Engineering Interfaces and Films," *Adv. Funct. Mater.*, vol. 18, pp. 17–26, 2008.

[70]   F. N. Crespilho, V. Zucolotto, O. N. O. Jr, and F. C. Nart, "Electrochemistry of Layer-by-Layer Films : a review," vol. 1, pp. 194–214, 2006.

[71]   Y.-Q. Zhang, Y.-J. Fan, L. Cheng, L.-L. Fan, Z.-Y. Wang, J.-P. Zhong, L.-N. Wu, X.-C. Shen, and Z.-J. Shi, "A novel glucose biosensor based on the immobilization of glucose oxidase on layer-by-layer assembly film of copper phthalocyanine functionalized graphene," *Electrochim. Acta*, vol. 104, pp. 178–184, Aug. 2013.

[72]   J. Ma, P. Cai, W. Qi, D. Kong, and H. Wang, "The layer-by-layer assembly of polyelectrolyte functionalized graphene sheets: A potential tool for biosensing," *Colloids Surfaces A Physicochem. Eng. Asp.*, vol. 426, pp. 6–11, Jun. 2013.

[73]   B. Zhang, Q. Li, and T. Cui, "Ultra-sensitive suspended graphene nanocomposite cancer sensors with strong suppression of electrical noise.," *Biosens. Bioelectron.*, vol. 31, no. 1, pp. 105–9, Jan. 2012.

[74]   C. Shan, L. Wang, D. Han, F. Li, Q. Zhang, X. Zhang, and L. Niu, "Polyethyleneimine-functionalized graphene and its layer-by-layer assembly with Prussian blue," *Thin Solid Films*, vol. 534, pp. 572–576, May 2013.

[75]   X. Weng, Q. Cao, L. Liang, J. Chen, C. You, Y. Ruan, H. Lin, and L. Wu, "Simultaneous determination of dopamine and uric acid using layer-by-layer graphene and chitosan assembled multilayer films.," *Talanta*, vol. 117, pp. 359–65, Dec. 2013.

[76]   L. Tang, X. Li, D. Du, and C. He, "Fabrication of multilayer films from regenerated cellulose and graphene oxide through layer-by-layer assembly," *Prog. Nat. Sci. Mater. Int.*, vol. 22, no. 4, pp. 341–346, Aug. 2012.

[77]   X. Xu, D. Huang, K. Cao, M. Wang, S. M. Zakeeruddin, and M. Grätzel, "Electrochemically reduced graphene oxide multilayer films as efficient counter electrode for dye-sensitized solar cells. supplementary," *Sci. Rep.*, vol. 3, p. 1489, 2013.

[78]   S. Liu, J. Ou, Z. Li, S. Yang, and J. Wang, "Layer-by-layer assembly and tribological property of multilayer ultrathin films constructed by modified graphene sheets and polyethyleneimine," *Appl. Surf. Sci.*, vol. 258, no. 7, pp. 2231–2236, Jan. 2012.

[79]   K. Sheng, H. Bai, Y. Sun, C. Li, and G. Shi, "Layer-by-layer assembly of graphene/polyaniline multilayer films and their application for electrochromic devices," *Polymer (Guildf).*, vol. 52, no. 24, pp. 5567–5572, Nov. 2011.

[80]   Y. Zhu and J. M. Tour, "Graphene nanoribbon thin films using layer-by-layer assembly.," *Nano Lett.*, vol. 10, no. 11, pp. 4356–62, Nov. 2010.

[81]   X. Ou, L. Jiang, P. Chen, M. Zhu, W. Hu, M. Liu, J. Zhu, and H. Ju, "Highly Stable Graphene-Based Multilayer Films Immobilized via Covalent Bonds and Their Applications in Organic Field-Effect Transistors," *Adv. Funct. Mater.*, vol. 23, no. 19, pp. 2422–2435, May 2013.

[82]   L. S. Nair and C. T. Laurencin, "Biodegradable polymers as biomaterials," *Prog. Polym. Sci.*, vol. 32, no. 8–9, pp. 762–798, Aug. 2007.

[83]   S. Vaddiraju, I. Tomazos, D. J. Burgess, F. C. Jain, and F. Papadimitrakopoulos, "Emerging synergy between nanotechnology and implantable biosensors: a review.," *Biosens. Bioelectron.*, vol. 25, no. 7, pp. 1553–65, Mar. 2010.

[84]   S. Hou, M. L. Kasner, S. Su, K. Patel, and R. Cuellari, "Highly Sensitive and Selective Dopamine Biosensor Fabricated with Silanized Graphene," *J. Phys. Chem. C*, vol. 114, no. 35, pp. 14915–14921, Sep. 2010.

[85]   T. H. Qazi, R. Rai, and A. R. Boccaccini, "Tissue engineering of electrically responsive tissues using polyaniline based polymers: A review.," *Biomaterials*, vol. 35, no. 33, pp. 9068–9086, Nov. 2014.

[86]   R. Balint, N. J. Cassidy, and S. H. Cartmell, "Conductive polymers : Towards a smart biomaterial for tissue engineering," *Acta Biomater.*, vol. 10, pp. 2341–2353, 2014.

[87]   C. Vallejo-Giraldo, A. Kelly, and M. J. P. Biggs, "Biofunctionalisation of electrically conducting polymers.," *Drug Discov. Today*, vol. 19, no. 1, pp. 88–94, Jan. 2014.

[88]   M. Deng, X. Yang, M. Silke, W. Qiu, M. Xu, G. Borghs, and H. Chen, "Electrochemical deposition of polypyrrole/graphene oxide composite on microelectrodes towards tuning the electrochemical properties of neural probes," *Sensors Actuators B Chem.*, vol. 158, no. 1, pp. 176–184, Nov. 2011.

[89]   K. Zhou, G. A. Thouas, C. C. Bernard, D. R. Nisbet, D. I. Finkelstein, D. Li, and J. S. Forsythe, "Method to impart electro- and biofunctionality to neural scaffolds using graphene-

polyelectrolyte multilayers.," *ACS Appl. Mater. Interfaces*, vol. 4, no. 9, pp. 4524–31, Sep. 2012.

[90]   S. Franz, S. Rammelt, D. Scharnweber, and J. C. Simon, "Immune responses to implants - a review of the implications for the design of immunomodulatory biomaterials.," *Biomaterials*, vol. 32, no. 28, pp. 6692–709, Oct. 2011.

[91]   A. W. Bridges and A. J. García, "Anti-inflammatory polymeric coatings for implantable biomaterials and devices.," *J. Diabetes Sci. Technol.*, vol. 2, no. 6, pp. 984–94, Nov. 2008.

[92]   S. Gaur, R. K. Singh Raman, and A. S. Khanna, "In vitro investigation of biodegradable polymeric coating for corrosion resistance of Mg-6Zn-Ca alloy in simulated body fluid.," *Mater. Sci. Eng. C. Mater. Biol. Appl.*, vol. 42, pp. 91–101, Sep. 2014.

[93]   J. Ma, M. Thompson, N. Zhao, and D. Zhu, "Similarities and differences in coatings for magnesium-based stents and orthopaedic implants," *J. Orthop. Transl.*, vol. 2, no. 3, pp. 118–130, Jul. 2014.

[94]   N. Argarate, B. Olalde, G. Atorrasagasti, J. Valero, S. Carolina Cifuentes, R. Benavente, M. Lieblich, and J. Luis González-Carrasco, "Biodegradable Bi-layered coating on polymeric orthopaedic implants for controlled release of drugs," *Mater. Lett.*, vol. 132, pp. 193–195, Oct. 2014.

[95]   A. Ciesielski and P. Samorì, "Graphene via sonication assisted liquid-phase exfoliation.," *Chem. Soc. Rev.*, vol. 43, no. 1, pp. 381–98, Jan. 2014.

[96]   R. J. Anderson, D. J. Bendell, and P. W. Groundwater, *Organic Spectroscopic Analysis*. Italy: The Royal Society of Chemistry, 2004.

[97]   G. Wang, B. Wang, J. Park, J. Yang, X. Shen, and J. Yao, "Synthesis of enhanced hydrophilic and hydrophobic graphene oxide nanosheets by a solvothermal method," *Carbon N. Y.*, vol. 47, no. 1, pp. 68–72, Jan. 2009.

[98]   *Spectrometric Identification of Organic Compunds*, 7th ed. New York: John Wiley & Sons, Inc.

[99]   K. A. Wepasnick, B. A. Smith, J. L. Bitter, and D. Howard Fairbrother, "Chemical and structural characterization of carbon nanotube surfaces.," *Anal. Bioanal. Chem.*, vol. 396, no. 3, pp. 1003–14, Feb. 2010.

[100]   S. J. Pennycook, A. R. Lupini, M. Varela, A. Y. Borisevich, Y. Peng, M. P. Oxley, K. van Benthem, and M. F. Chisholm, "Scanning Transmission Electron Microscopy for Nanostructure Characterization," in *Scanning Microscopy for Nanotechnology*, 1st ed., New York: Springer, 2007, pp. 152–191.

[101]   J. H. Warner, F. Schaffel, M. Rummeli, and A. Bachmatiuk, *Graphene: Fundamentals and emergent applications*, 1st ed. United States of America: Elsevier, 2013.

[102]   S. N. Magonov, M. Whangbo, and T. Aspects, *Surface Analysis with STM and AFM*. Weinheim, Germany: Wiley-VCH Verlag GmbH, 1995.

[103]   Y. Song and B. Bhushan, "Atomic force microscopy dynamic modes: modeling and applications," *J. Phys. Condens. Matter*, vol. 20, no. 22, p. 225012, Jun. 2008.

[104]   D. Nečas and P. Klapetek, *Gwyddion: an open-source software for SPM data analysis*, vol. 10, no. 1. 2011, pp. 181–188.

[105] P. Hawkes and J. C. H. Spence, "Science of Microscopy, Volume 1," in *Science of Microscopy, Volume 1*, 1st ed., vol. 982, Springer, 2007, pp. 969–1024.

[106] P. Atkins and J. de Paula, *Atkins' Physical Chemistry*, 8th ed. Italy: Oxford University Press, 2006.

[107] F. Davis and S. P. J. Higson, "Structured thin films as functional components within biosensors.," *Biosens. Bioelectron.*, vol. 21, no. 1, pp. 1–20, Jul. 2005.

[108] K. A. Marx, "Quartz crystal microbalance: a useful tool for studying thin polymer films and complex biomolecular systems at the solution-surface interface.," *Biomacromolecules*, vol. 4, no. 5, pp. 1099–120, 2003.

[109] A. I. Neto, A. C. Cibrão, C. R. Correia, R. R. Carvalho, G. M. Luz, G. G. Ferrer, G. Botelho, C. Picart, N. M. Alves, and J. F. Mano, "Nanostructured Polymeric Coatings Based on Chitosan and Dopamine-Modifi ed Hyaluronic Acid for Biomedical Applications," pp. 2459–2469, 2014.

[110] U. Khan, A. O'Neill, M. Lotya, S. De, and J. N. Coleman, "High-concentration solvent exfoliation of graphene.," *Small*, vol. 6, no. 7, pp. 864–71, Apr. 2010.

[111] Y. Hernandez, V. Nicolosi, M. Lotya, F. M. Blighe, Z. Sun, S. De, I. T. McGovern, B. Holland, M. Byrne, Y. K. Gun'Ko, J. J. Boland, P. Niraj, G. Duesberg, S. Krishnamurthy, R. Goodhue, J. Hutchison, V. Scardaci, A. C. Ferrari, and J. N. Coleman, "High-yield production of graphene by liquid-phase exfoliation of graphite.," *Nat. Nanotechnol.*, vol. 3, no. 9, pp. 563–8, Sep. 2008.

[112] B. Unnikrishnan, V. Mani, and S.-M. Chen, "Highly sensitive amperometric sensor for carbamazepine determination based on electrochemically reduced graphene oxide–single-walled carbon nanotube composite film," *Sensors Actuators B Chem.*, vol. 173, pp. 274–280, Oct. 2012.

[113] P. A. A. P. Marques, G. Gonçalves, S. Cruz, N. Almeida, M. K. Singh, J. Grácio, and A. C. M. Sousa, "Functionalized Graphene Nanocomposites," in *Advances in Nanocomposite Technology*, 1st ed., A. Hashim, Ed. InTech, 2011, pp. 247 – 272.

[114] S. Cheemalapati, S. Palanisamy, V. Mani, and S. Chen, "Simultaneous electrochemical determination of dopamine and paracetamol on multiwalled carbon nanotubes / graphene oxide nanocomposite-modi fi ed glassy carbon electrode," *Talanta*, vol. 117, pp. 297–304, 2013.

[115] S. Chaiyakun, N. Witit-anun, N. Nuntawong, P. Chindaudom, S. Oaew, C. Kedkeaw, and P. Limsuwan, "Preparation and characterization of graphene oxide nanosheets," *Procedia Eng.*, vol. 32, pp. 759–764, Jan. 2012.

[116] B. H. Stuart, *Infrared Spectroscopy: Fundamentals and Applications*, 1st ed., vol. 8. England: Wiley, 2004.

[117] S. Bykkam, K. V. Rao, S. C. Ch, and T. Thunugunta, "Synthesis and Characterization of graphene oxide and its antimicrobial activity against Klebseilla and Staphylococus," vol. 4, no. 1, pp. 142–146, 2013.

[118] K. Satheesh and R. Jayavel, "Synthesis and electrochemical properties of reduced graphene oxide via chemical reduction using thiourea as a reducing agent," *Mater. Lett.*, vol. 113, pp. 5–8, Dec. 2013.

[119] B. Unnikrishnan, S. Palanisamy, and S. Chen, "A simple electrochemical approach to fabricate a glucose biosensor based on graphene – glucose oxidase biocomposite," *Biosens. Bioelectron.*, vol. 39, pp. 70–75, 2013.

[120] W. Chen and L. Yan, "Preparation of graphene by a low-temperature thermal reduction at atmosphere pressure.," *Nanoscale*, vol. 2, no. 4, pp. 559–63, Apr. 2010.

[121] E. Cisternas and J. D. Correa, "Theoretical reproduction of superstructures revealed by STM on bilayer graphene," *Chem. Phys.*, vol. 409, pp. 74–78, Dec. 2012.

[122] H. Ö. Doğan, D. Ekinci, and Ü. Demir, "Atomic scale imaging and spectroscopic characterization of electrochemically reduced graphene oxide," *Surf. Sci.*, vol. 611, pp. 54–59, May 2013.

[123] R. R. Costa, C. A. Custódio, A. M. Testera, F. J. Arias, J. C. Rodríguez-Cabello, N. M. Alves, and J. F. Mano, "Stimuli-Responsive Thin Coatings Using Elastin-Like Polymers for Biomedical Applications," *Adv. Funct. Mater.*, vol. 19, no. 20, pp. 3210–3218, Oct. 2009.

[124] S. R. MacEwan and A. Chilkoti, "Applications of elastin-like polypeptides in drug delivery.," *J. Control. Release*, vol. 190, pp. 314–30, Sep. 2014.

[125] G. V Martins, E. G. Merino, J. F. Mano, and N. M. Alves, "Crosslink effect and albumin adsorption onto chitosan/alginate multilayered systems: an in situ QCM-D study.," *Macromol. Biosci.*, vol. 10, no. 12, pp. 1444–55, Dec. 2010.

[126] M. G. Carneiro-da-Cunha, M. A. Cerqueira, B. W. S. Souza, J. A. Teixeira, and A. A. Vicente, "Influence of concentration, ionic strength and pH on zeta potential and mean hydrodynamic diameter of edible polysaccharide solutions envisaged for multinanolayered films production," *Carbohydr. Polym.*, vol. 85, no. 3, pp. 522–528, Jun. 2011.
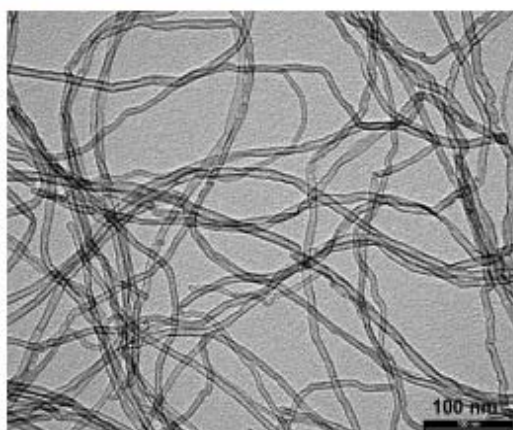
Attachments

Attachment 1

NANO-ENGINEER YOUR FUTURE

nanocyl

THE CARBON NANOTUBE SPECIALIST

Ref: NANOCYL™ NC7000 – 10 March 2009 - V05

NANOCYL™ NC7000 series - Product Datasheet – Thin Multi-Wall Carbon Nanotubes

General information

NANOCYL™ NC7000 series, thin multi-wall carbon nanotubes, are produced via the catalytic carbon vapor deposition (CCVD) process.

A primary interest is in applications requiring low electrical percolation threshold such as high-performance electrostatic dissipative plastics or coatings.

NC7000 is available in powder form in quantities starting at 2 kg to multi-tons.

Pre-dispersed forms are also available (PLASTICYL™, EPOCYL™, AQUACYL™).

Characterization NC7000

PROPERTY	UNIT	VALUE	METHOD OF MEASUREMENT
Average Diameter	nanometers	9.5	TEM
Average Length	microns	1.5	TEM
Carbon Purity	%	90	TGA
Metal Oxide	%	10	TGA
Amorphous Carbon	-	*	HRTEM
Surface Area	m^2/g	250-300	BET

* Pyrolytically deposited carbon on the surface of the NC7000

+ Further information is available upon request

The information contained on this datasheet is believed to be reliable— yet Nanocyl makes no warranties and assumes no liability in connection with any use of this information. Nothing herein is to be taken as a license to operate under or infringe any patent. While this information is accurate at the time of publication, please contact Nanocyl or check http://www.nanocyl.com for the most up-to-date information.

Nanocyl S.A.
Rue de l'Essor 4
B-5060 Sambreville
BELGIUM
Tel +32 71 750 380
Fax +32 71 750 390
sales@nanocyl.com

US contact
info-us@nanocyl.com

www.nanocyl.com

Attachment 2

Nacional de Grafite Ltda.

Micrograf® HC11
Natural Crystalline Graphite

	Unid.		**Valores Garantidos** *Guaranteed Values*		
				Min.	Max.
Carbono - Perda ao Fogo	(%)	*Carbon - Loss on Ignition*		99,5	
Cinzas	(%)	*Ash content*			0,5
Umidade	(%)	*Moisture content*			0,5

Granulometria - laser		*Sizing - laser*	
d_{50}	(µm)		11,0

Embalagens		*Packing*	
Bags	:	4 kg	
Pallets	:	160 kg	
Big Bags	:	--	

Rev.: 00   Pag.: 1/1   Data: 01/09/11

É recomendado testar as amostras, uma vez que os resultados podem divergir devido a diferentes metodologias.
Documento controlado quando disponível no site **www.grafite.com** ou na intranet da Nacional de Grafite
We strongly recommend, sample trial since results may diverge due to different methodologies
The document is controlled when available at www.grafite.com or Nacional de Grafite's Intranet

Pesquisa e Desenvolvimento de Processo		**Gestão da Qualidade**	
Nome: Helvécio Alves Vespúcio		**Nome:** Antônio Sérgio de Souza	
Função: Gerente P&DP	**Assinatura:**	**Função:** C. Cont. Qualidade	**Assinatura:**
Alteração: Mudança de lay-out.			

Nacional de Grafite Ltda. Av. Paulista, 460 - 11° andar - Cep: 01310-904 - São Paulo/SP - Brasil - tel.: +55 11 3289-1322 - fax +55 11 3289-7835 - www.grafite.com